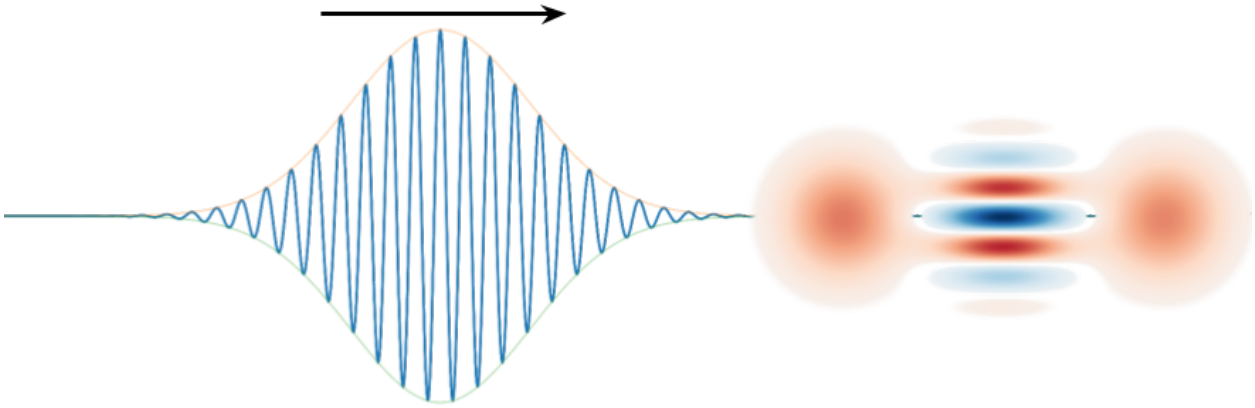

Optimal Encoding of Quantum Information into a Propagating Mode

Master's thesis in Physics

CECILIA ERNEMAN

DEPARTMENT OF MICROTECHNOLOGY AND NANOSCIENCE

CHALMERS UNIVERSITY OF TECHNOLOGY
Gothenburg, Sweden 2026
www.chalmers.se

Master's thesis 2026

Optimal Encoding of Quantum Information into a Propagating Mode

CECILIA ERNEMAN

CHALMERS
UNIVERSITY OF TECHNOLOGY

Department of Microtechnology and Nanoscience
Division of Applied Quantum Physics
Chalmers University of Technology
Gothenburg, Sweden 2026

Optimal Encoding of Quantum Information into a Propagating Mode
CECILIA ERNEMAN

Supervisor: Maryam Khanahmadi, Department of Microtechnology and Nanoscience
Examiner: Göran Johansson, Department of Microtechnology and Nanoscience

Master's Thesis 2026
Department of Microtechnology and Nanoscience
Division of Applied Quantum Physics
Chalmers University of Technology
SE-412 96 Gothenburg
Telephone +46 31 772 1000

Cover: Shaped wavepacket in a transmission line and the Wigner function of the captured single-mode state obtained by virtual-cavity mode extraction.

Typeset in LaTeX
Printed by Chalmers Reproservice
Gothenburg, Sweden 2026

Optimal Encoding of Quantum Information into a Propagating Mode
CECILIA ERNEMAN
Department of Microtechnology and Nanoscience
Chalmers University of Technology

Abstract

This thesis studies how quantum information can be encoded into a propagating microwave mode in a superconducting-circuit setting, with particular emphasis on traveling two-component cat states and cat qubits. The work focuses on how such states can be prepared, released into a transmission line, and characterized after emission. To do this, numerical protocols were developed for state preparation and release, identification of the dominant temporal output mode, and reconstruction of the captured propagating state using a cascaded virtual-cavity approach.
Two different confinement mechanisms were examined: a Kerr-nonlinear parametric oscillator (KPO) and an alternative model based on engineered two-photon dissipation. The captured traveling mode was evaluated using fidelity to ideal cat-qubit target states, state purity, and the efficiency of the dominant temporal mode; in particular, fidelities above 0.96 was obtained for cat states with photon numbers up to 5. For the Kerr model, the results show that high-fidelity propagating cat-qubit states can be generated while still remaining strongly concentrated in a single temporal mode. Across the target photon numbers considered here, the low-pass-filter order pair $(n_p, n_\varepsilon) = (3, 2)$ gave the best overall performance, and shortcut-to-adiabaticity was found to noticeably improve the preparation-and-release protocol. The dominant extracted mode also showed good agreement with the intended reference mode shape.
The two-photon dissipative model was also able to generate traveling cat-like states, although its performance depended strongly on the strength of the two-photon loss. Increasing the dissipative confinement improved fidelity, purity, and mode selectivity. This indicates that the dissipative-confinement model provides a comparatively robust state-generation process relative to the Kerr-confinement model, possibly due to quantum-Zeno-like suppression of unwanted dynamics.
In addition, noise analyses including pure dephasing and one-photon loss showed a systematic decrease in performance in both models, while also indicating that the protocols remain qualitatively functional in the weak-noise regime. Overall, the results show that high-quality propagating cat-qubit encodings can be generated numerically in superconducting-circuit-inspired models, and that both pulse design and the choice of confinement mechanism play an important role in the quality of the transferred state.

Keywords: Quantum communication, circuit quantum electrodynamics, bosonic encoding, cat qubits, Kerr-nonlinear parametric oscillator, two-photon dissipation, propagating microwave modes, virtual cavity.

Acknowledgements

First and foremost, I would like to thank my supervisor, Maryam Khanahmadi, for her invaluable guidance, insightful discussions, and continuous support throughout this thesis project. I would also like to extend my sincere thanks to Zeidan Zeidan for his valuable feedback, engagement, and support, all of which have been greatly appreciated.
I am also grateful to my examiner, Göran Johansson, and to the Department of Microtechnology and Nanoscience for providing me with the opportunity to carry out this thesis in such an inspiring research environment. I would further like to thank my opponent, Oscar Muhr, for his time and engagement.
Finally, I would like to thank my family and friends for their encouragement and support throughout my studies.

Cecilia Erneman, Gothenburg, March 2026

List of Acronyms

Below is the list of acronyms that have been used throughout this thesis listed in alphabetical order:

cQED	Circuit quantum electrodynamics
KPO	Kerr-nonlinear parametric oscillator
LPF	Low-pass filter
RMSE	Root-mean-square error
RWA	Rotating-wave approximation
STA	Shortcut to adiabaticity

Nomenclature

Below is a list of the most frequently used symbols in this thesis.

Operators and states

$\hat{a}$	Annihilation operator for the resonator mode
$\hat{a}^\dagger$	Creation operator for the resonator mode
$\|\alpha\rangle$	Coherent state with complex amplitude α
$\|C_\pm(\alpha)\rangle$	Even/odd cat state with amplitude α
ρ	Density matrix
ρ_v	Density matrix of the captured virtual mode

Control and model parameters

α	Complex coherent-state amplitude
A	Two-photon pump amplitude
ε_x	Normalized one-photon-drive amplitude
K	Kerr nonlinearity
K_{ham}	Hamiltonian Kerr strength
K_{th}	Threshold Kerr scale used for normalization
λ_p	Two-photon pump-time scaling factor
λ_ε	One-photon-drive time scaling factor
κ_{ex}	External coupling rate to the transmission line
κ_1	One-photon loss rate
κ_2	Two-photon loss rate
κ_ϕ	Dephasing rate

Performance metrics and derived quantities

N_{out}	Target output photon number
N_{feed}	Two-photon pump feed quantity
p_+	Fitted even-cat weight
p_-	Fitted odd-cat weight
η_{top}	Efficiency of the dominant temporal mode
$\mathcal{F}_{\mathrm{eo}}$	Fidelity with the ideal even/odd cat-qubit target state
$\mathcal{F}_{\mathrm{eo}}^{\mathrm{min}}$	Minimum even/odd cat-qubit fidelity over a specified interval

Contents

List of Figures

List of Tables

1
Introduction

This chapter introduces the motivation for the thesis, describes the aim and delimitations, and outlines the structure of the report.

1.1 Background and motivation

The state space of a quantum system grows exponentially with system size, making it difficult to simulate the dynamics of such a system on a classical computer [1], [2]. A quantum computer naturally represents and processes quantum states, and it can (in principle) simulate certain quantum states more efficiently than classical computers, with major relevance for chemistry and materials design [3]. Furthermore, quantum algorithms can offer speedups for specific computational problems; such an example is Shor's algorithm used for integer factoring, with importance in cryptography [4]. Today's quantum computers have limited numbers of qubits and the stored quantum information is easily disturbed by noise [5]. To perform long and reliable computations, future quantum computers will need quantum error correction [6], [7]. The basic idea is to encode one logical qubit into many physical qubits so that errors can be detected and corrected repeatedly while the computation runs [6]. Building an error-corrected processor with many qubits then becomes not only a question of improving individual qubits, but also of solving major architecture challenges related to scaling up the hardware [7].

Building one very large quantum processor introduces engineering problems such as increased complexity in design and control, and the need to accurately characterize and tune many interacting components. Unwanted interactions (cross-talk) between different parts of the circuit can also become significant, and fast control and readout must be integrated without destroying the fragile quantum states, which places strong demands on isolation and shielding [7]. One promising way to overcome these issues when scaling is to build smaller quantum processors and connect them, known as distributed quantum computing, instead of putting everything on a single device [8]. In this kind of architecture, the connection must be able to carry quantum information without destroying it, which turns reliable quantum state transfer between nodes into a central requirement [8].

In superconducting circuit platforms quantum information can be stored in microwave resonators and processed with superconducting qubits. Furthermore, microwave pulses in transmission lines can act as carriers between different parts of the system [7], [9]. This means that a practical building block for a distributed superconducting system is to prepare a desired quantum state in a device, release it

into a traveling pulse, and capture it elsewhere [9].
Instead of encoding information only in two-level systems, one can encode a so called logical qubit in an oscillator mode, known as bosonic encoding, which can offer advantages for noise protection and hardware efficiency [9], [10]. In particular, specific superpositions of coherent states, so called cat states, provide a natural bosonic basis and have been demonstrated in superconducting systems [10], [11]. For modular superconducting architectures, it is therefore interesting to generate traveling cat-qubit states that can carry logical information between nodes [9].
In general, the emitted radiation can occupy several independent temporal wavepackets (temporal modes). Since any receiver effectively couples to a specific mode, it is essential to characterize how close the emitted pulse is to a single mode and to quantify the fraction of the radiation that can be collected in a chosen target wavepacket [12].

1.2 Aim

The aim of this master's thesis project is to investigate how quantum information can be encoded into a propagating microwave mode in a superconducting circuit setting. Prior work establishes generation and mode-selective readout of nonclassical pulses. This thesis will extend this to logical qubits in traveling modes. More specifically, the aim of this project is to develop and evaluate protocols to generate, shape, and read out propagating bosonic code states, specifically two-component cat states, and quantify their suitability for quantum communication between superconducting nodes.
More concretely, the objectives are to simulate the preparation and release of nonclassical states into a transmission line for both a Kerr-nonlinear parametric oscillator (KPO) and an alternative model based on engineered two-photon dissipation. The study then quantifies how strongly the emission is concentrated into the dominant temporal output mode, models mode-matched capture of the selected propagating mode using a cascaded (virtual-cavity) approach and extracts its density matrix, and benchmarks the captured mode against ideal cat(-qubit) target states using state fidelity.

1.3 Delimitations

This thesis is a theoretical and numerical study of quantum-state emission and mode-selective capture in superconducting circuit-inspired models. The work does not include an experimental implementation, and practical aspects such as device fabrication, calibration procedures, and experimental data analysis are therefore outside the scope of the project. The dynamics are modeled using open-quantum-system methods together with input-output and cascaded-systems formalisms.
The analysis focuses on extracting and characterizing the most populated propagating temporal mode. Populations emitted into other temporal modes are treated as multimode leakage rather than being actively captured and used. The target states considered are bosonic encodings based on cat(-qubit) states, and other bosonic

codes are not being studied. Finally, results are primarily evaluated using mode selectivity and the state fidelity of the captured mode with respect to optimized target cat(-qubit) states, additional hardware-specific imperfections beyond the chosen model are not exhaustively included.

1.4 Thesis outline

The remainder of this thesis is organized as follows. Chapter 2 presents the theoretical background relevant to the study, including bosonic encodings in harmonic oscillators, two-component cat states and cat-qubit encoding, effective models for driven resonators, and the open-system description of emission into a transmission line. It also introduces temporal-mode decomposition and the virtual-cavity approach used to characterize propagating states.
Chapter 3 describes the methods used in the numerical study. This includes the full system model for both Kerr-based and dissipative confinement, the parametrization of the control pulses, the numerical implementation, calibration procedures, and the metrics used to evaluate the captured traveling mode.
Chapter 4 presents the results. First, results are shown for the Kerr (Hamiltonian-confinement) model, including intracavity cat formation, LPF-order optimization, captured-state Wigner functions, mode-shape comparisons, pulse-time optimization, Kerr-scaling effects, and initialization in a logical superposition state. The chapter then compares these results with the two-photon dissipative-confinement model and finally investigates robustness against dephasing and one-photon loss.
Chapter 5 summarizes the main conclusions of the thesis and discusses the overall implications of the results for encoding quantum information into propagating bosonic modes in superconducting platforms.

2

Theory

This chapter introduces the theoretical framework underlying the thesis. It begins with a brief review of quantum states, qubits, and bosonic encodings in harmonic oscillators, with particular focus on two-component cat states and cat-qubit encoding. The chapter then presents the effective description of driven nonlinear resonators, including the Kerr-nonlinear parametric oscillator, shortcut-to-adiabaticity, and logical rotations induced by a one-photon drive. Furthermore, an alternative model to the Kerr-nonlinear parametric oscillator, based on two-photon dissipation is described. Finally, the open-system description of emission into a transmission line is introduced together with the temporal-mode and virtual-cavity formalisms used later to analyze and characterize the propagating quantum state.

2.1 Quantum states, qubits, and logical qubits

A qubit is a two-dimensional quantum system with computational basis $\{|0\rangle, |1\rangle\}$. Any pure qubit state can be written as $|\psi\rangle = c_0 |0\rangle + c_1 |1\rangle$ with $c_0, c_1 \in \mathbb{C}$ and $|c_0|^2 + |c_1|^2 = 1$. In practice, physical qubits are imperfect, the stored quantum information is disturbed by interactions with the environment and control errors. In the near term, this limits the complexity of quantum computations that can be performed reliably and motivates strategies for protecting quantum information [5]. A central protection strategy is called quantum error correction, where logical qubits, which encodes quantum information into a larger Hilbert space, are introduced [6]. The main idea is to distribute the information across many physical degrees of freedom such that errors can be detected and corrected repeatedly while preserving the encoded state [6]. The computational basis of the logical qubit is then represented by two orthonormal states $\{|0_L\rangle, |1_L\rangle\}$.
Apart from two-level systems, logical qubits can also be encoded in the Hilbert space of a harmonic oscillator mode, such as a microwave resonator, these types of encodings are referred to as Bosonic codes [9]. This approach is particularly natural in circuit quantum electrodynamics (cQED), where long-lived cavity modes can store quantum states, while superconducting qubits provide a convenient interface for control and measurement of the oscillator state [9].

2.2 Qubit encoding in a Quantum harmonic oscillator

A single bosonic mode is described by the annihilation and creation operators $\hat{a}$, $\hat{a}^\dagger$, which satisfy the commutation relation $[\hat{a}, \hat{a}^\dagger] = 1$.
The Hamiltonian of an ideal harmonic oscillator can be expressed as Equation (2.1)

$$\hat{H}_{osc} = \hbar\omega \left(\hat{a}^\dagger \hat{a} + \frac{1}{2}\right) \tag{2.1}$$

where ω is the angular frequency of the oscillator. The eigenstates of $\hat{H}_{osc}$ is the Fock states $|n\rangle$, with $n = 0, 1, 2, ...$, which obeys Equation (2.2)

$$\begin{aligned} \hat{a}^\dagger |n\rangle &= \sqrt{n+1}\, |n+1\rangle \\ \hat{a} |n\rangle &= \sqrt{n}\, |n-1\rangle \\ \hat{a}^\dagger \hat{a} |n\rangle &= n |n\rangle . \end{aligned} \tag{2.2}$$

In cQED, these states correspond to having n microwave photons stored in the resonator [9].
Many bosonic encodings are expressed using coherent states, $|\alpha\rangle$, defined in Equation (2.3)

$$|\alpha\rangle = e^{-\frac{|\alpha|^2}{2}} \sum_{n=0}^{\infty} \frac{\alpha^n}{\sqrt{n!}} |n\rangle , \; \alpha \in \mathbb{C}. \tag{2.3}$$

Furthermore, the coherent states are defined as an eigenstate of the annihilation operator, i.e. $\hat{a} |\alpha\rangle = \alpha |\alpha\rangle$.
The complex coherent state amplitude, α, can be parametrized in polar form as Equation (2.4)

$$\alpha = r_\alpha e^{i\theta_\alpha}, \tag{2.4}$$

where $r_\alpha = |\alpha| \geq 0$ is the magnitude and $\theta_\alpha = \arg(\alpha) \in [0, 2\pi)$ is the phase of the coherent-state displacement. Equivalently, in Cartesian coordinates, the coherent state amplitude can be parametrized as Equation (2.5)

$$\alpha = \mathrm{Re}(\alpha) + i\, \mathrm{Im}(\alpha), \tag{2.5}$$

where $\mathrm{Re}(\alpha) = r_\alpha \cos\theta_\alpha$ and $\mathrm{Im}(\alpha) = r_\alpha \sin\theta_\alpha$. A graphical illustration of this parametrization in the complex α-plane is shown in Figure 2.1.

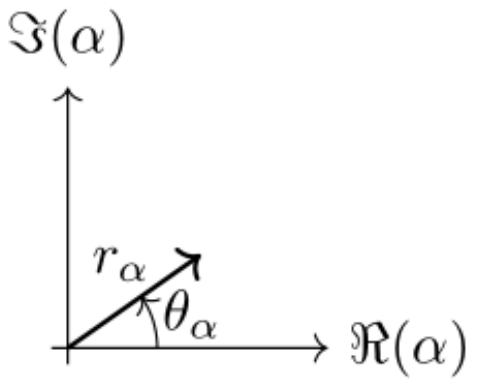

Figure 2.1: Parametrization of the coherent-state amplitude α in the complex plane. The displacement α is written in polar form $\alpha = r_\alpha e^{i\theta_\alpha}$, where $r_\alpha = |\alpha|$ and $\theta_\alpha = \arg(\alpha)$, with axes $\mathrm{Re}(\alpha)$ and $\mathrm{Im}(\alpha)$.

2.3 Two-component cat states and the 2-cat qubit

This section introduces the two-component cat states and the associated two-component cat-qubit encoding, which form the conceptual basis for the numerical and theoretical analysis in the remainder of this thesis. First, the even and odd cat states are defined as superpositions of coherent states and their overlap properties are discussed. Next, the Wigner function is introduced as a phase-space representation used to visualize cat states and to identify nonclassical interference features. Finally, the logical cat-qubit basis and Bloch-sphere parameterization are defined, and the role of photon-number parity in error detection under single-photon loss is briefly reviewed.

2.3.1 Two-component cat states

One type of bosonic encoding, which is the main focus of this thesis, is the two-component cat states. These states are superpositions of coherent states $|\alpha\rangle$ and $|-\alpha\rangle$, where $\alpha \in \mathbb{C}$ denotes the coherent state amplitude. In Equation (2.6) the even ($|C_+\rangle$) respectively odd ($|C_-\rangle$) two-component cat states are defined

$$\begin{aligned} |C_+(\alpha)\rangle &= \frac{1}{\sqrt{2(1+e^{-2|\alpha|^2})}}(|\alpha\rangle + |-\alpha\rangle) \\ |C_-(\alpha)\rangle &= \frac{1}{\sqrt{2(1-e^{-2|\alpha|^2})}}(|\alpha\rangle - |-\alpha\rangle). \end{aligned} \tag{2.6}$$

The overlap between the coherent states, $\langle\alpha|-\alpha\rangle = e^{-2|\alpha|^2}$, decays exponentially with $|\alpha|^2$, so for sufficiently large $|\alpha|$ the states $|\alpha\rangle$ and $|-\alpha\rangle$ become nearly orthogonal, enabling a well-separated logical subspace. However, this improved distinguishability comes at the cost of increased sensitivity to photon loss for larger cat amplitudes [9], [10].

2.3.2 Wigner function and phase-space representation

A common phase-space representation of a single bosonic mode is given by the Wigner function, a real-valued quasi-probability distribution over the complex phase-space coordinate $\beta \in \mathbb{C}$. For a state described by the density operator ρ, the Wigner function can be expressed in the displaced-parity form presented in Equation (2.7),

$$W(\beta) = \frac{2}{\pi}\mathrm{Tr}\{\hat{D}(-\beta)\rho\hat{D}(\beta)\hat{\Pi}\}, \tag{2.7}$$

where $\hat{D}(\beta) = \exp\left\{\beta\hat{a}^\dagger - \beta^*\hat{a}\right\}$ is the displacement operator and $\hat{\Pi} = \exp\left\{i\pi\hat{a}^\dagger\hat{a}\right\}$ is the photon number parity operator [13]. Equation 2.7 makes explicit that $W(\beta)$ is proportional to the expectation value of parity after displacing the state by β.
The Wigner function is particularly useful for cat states, where the two coherent components appear as separated phase-space peaks, while coherent superpositions exhibit oscillatory interference fringes with regions of negative $W(\beta)$ between the peaks [10]. Such interference features are used throughout this thesis as a visual signature of nonclassical superposition in the two-component cat-qubit manifold.

2.3.3 Two-component cat-qubit encoding

By restricting the logical qubit to the two-dimensional subspace spanned by the even and odd cat states $\{|C_+(\alpha)\rangle, |C_-(\alpha)\rangle\}$, the standard two-component cat-qubit encoding presented in Equation (2.8) can be adopted

$$\begin{aligned} |0_L\rangle &\equiv |C_+(\alpha)\rangle \\ |1_L\rangle &\equiv |C_-(\alpha)\rangle . \end{aligned} \tag{2.8}$$

With this choice of logical basis, an arbitrary encoded state can be parameterized on the Bloch sphere as Equation (2.9)

$$|\psi_L(\alpha,\theta,\varphi)\rangle = \cos\frac{\theta}{2}|C_+(\alpha)\rangle + \sin\frac{\theta}{2}e^{i\varphi}|C_-(\alpha)\rangle, \text{ with } \theta \in [0,\pi],\ \varphi \in [0,2\pi]. \tag{2.9}$$

Any pure logical state $|\psi_L(\alpha,\theta,\varphi)\rangle$ in Equation (2.9) corresponds to a point on the unit sphere with spherical coordinates (θ,φ), where θ is the angle measured from the $+Z_L$ axis and φ is the angle measured in the X_L-Y_L plane. With the convention presented in Equation (2.8), the north and south poles of the sphere correspond to $|C_+(\alpha)\rangle$ and $|C_-(\alpha)\rangle$, respectively, defining the logical Z_L axis.
The remaining logical axes are defined by the eigenstates of the logical Pauli operators. In particular, the logical X_L and Y_L states are presented in Equation (2.10)

$$\begin{aligned} |\pm_L\rangle &= \frac{|0_L\rangle \pm |1_L\rangle}{\sqrt{2}} \\ |\pm i_L\rangle &= \frac{|0_L\rangle \pm i\,|1_L\rangle}{\sqrt{2}}, \end{aligned} \tag{2.10}$$

which, in the cat basis, correspond to $|\pm\rangle_L \approx |\pm\alpha\rangle$ and $|\pm i\rangle_L \approx |\alpha\rangle \pm i\,|-\alpha\rangle =: |C_{\pm i}(\alpha)\rangle$ (up to normalization and an α-dependent overlap). A visualization of this logical Bloch sphere, together with Wigner functions for the six cardinal logical states, is shown in Figure 2.2.

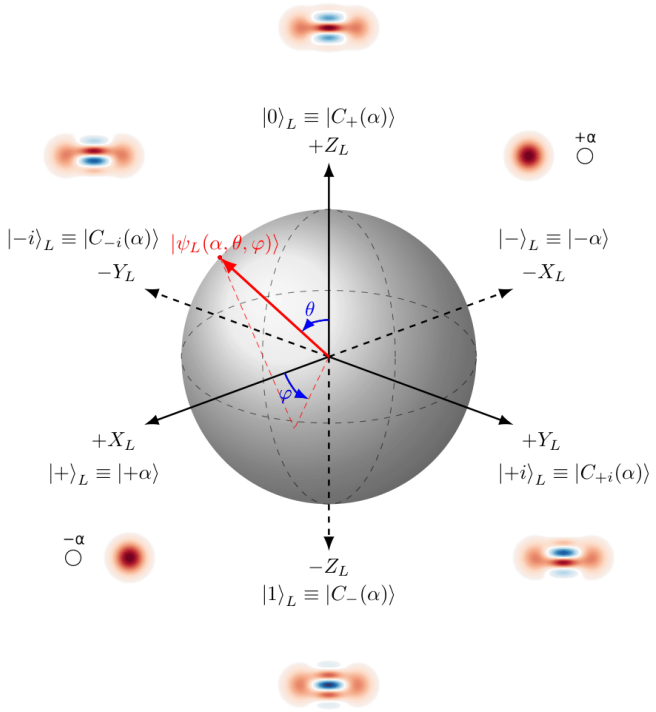

Figure 2.2: Bloch-sphere representation of the two-component cat logical qubit. The logical computational basis is chosen as $|0_L\rangle \equiv |C_+(\alpha)\rangle$ and $|1_L\rangle \equiv |C_-(\alpha)\rangle$, defining the $\pm Z_L$ axis. The remaining cardinal states correspond to eigenstates of the logical Pauli operators: $|\pm\rangle_L \equiv |\pm\alpha\rangle$ (along $\pm X_L$) and $|\pm i\rangle_L \equiv |C_{\pm i}(\alpha)\rangle \propto |\alpha\rangle \pm i\,|-\alpha\rangle$ (along $\pm Y_L$). The red arrow shows a general logical state $|\psi_L(\alpha,\theta,\varphi)\rangle = \cos(\theta/2)\,|C_+(\alpha)\rangle + \sin(\theta/2)e^{i\varphi}\,|C_-(\alpha)\rangle$ with spherical angles θ and φ measured with respect to the logical axes. The figure also shows the Wigner functions corresponding to each eigenstate (red/blue indicate positive/negative values and interference fringes). For $|\pm\alpha\rangle$ an open circle marks the phase-space location of the opposite coherent amplitude $\mp\alpha$.

The even and odd two-component cat states contain only even and only odd photon-number (Fock) components, respectively. They are therefore eigenstates of the photon-number parity operator $\hat{\Pi} = e^{i\pi\hat{a}^\dagger\hat{a}}$ with eigenvalues $+1$ and -1, respectively [9], [10].
One of the main reasons for the two-component cat qubit being of interest to study in superconducting circuit platforms is that they have properties useful for quantum error detection and correction. A single-photon loss event corresponds to applying the annihilation operator $\hat{a}$ to the state, and because $\hat{a}$ removes exactly one exci-

tation, the photon-number parity switches from even to odd (or vice versa). For a two-component cat encoding, this means that a single-photon loss typically moves the state from the even-cat subspace to the odd-cat subspace, or the other way around. This means that by monitoring the photon-number parity one gains information whether a photon-loss event has occurred, which is a key ingredient in cat-code error detection and correction schemes [9], [10].

2.4 Effective models for driven resonators

Parametrically driven microwave resonators exhibit dynamics on multiple time scales. They display fast oscillations at microwave frequencies set by the bare resonator and pump, but also slower evolution associated with effective detunings, nonlinearities, dissipation, and shaped control envelopes. A standard strategy in circuit QED is therefore to reformulate the problem in a rotating frame and subsequently apply the rotating-wave approximation (RWA), which yields an effective Hamiltonian in terms of slowly varying operators and drive envelopes [13], [14], [15]. These tools will be used throughout this work to motivate effective models for the Kerr-nonlinear parametric oscillator (KPO) (see Section 2.5.1 for details) and its control drives.

2.4.1 Rotating frame

Formally, the rotating frame is introduced as a time-dependent change of picture implemented by a unitary operator. Consider a quantum system with Hamiltonian $\hat{H}(t)$ and a state $|\psi(t)\rangle$ obeying the Schrödinger equation, presented in Equation (2.11)

$$i\hbar\frac{\partial}{\partial t}|\psi(t)\rangle = \hat{H}(t)|\psi(t)\rangle\,. \tag{2.11}$$

The state in the rotating frame can then be defined as Equation (2.12)

$$|\psi'(t)\rangle = \hat{U}^\dagger(t)|\psi(t)\rangle \tag{2.12}$$

where $\hat{U}(t)$ is unitary, i.e. $\hat{U}^\dagger(t)\hat{U}(t) = \mathbb{I}$. Using the product rule and unitary, one finds that $|\psi'(t)\rangle$ satisfies a Schrödinger equation of the same form, presented in Equation (2.13)

$$i\hbar\frac{\partial}{\partial t}|\psi'(t)\rangle = \hat{H}'(t)|\psi'(t)\rangle\,, \tag{2.13}$$

with the transformed Hamiltonian presented in Equation (2.14)

$$\hat{H}'(t) = \hat{U}^\dagger(t)\hat{H}(t)\hat{U}(t) - i\hbar\hat{U}^\dagger(t)\frac{\partial\hat{U}(t)}{\partial t} \tag{2.14}$$

which is the standard rotating-frame transformation [15].
In many driven-resonator problems it is convenient to separate the Hamiltonian as Equation (2.15)

$$\hat{H}(t) = \hat{H}_0 + \hat{V}(t), \tag{2.15}$$

where $\hat{H}_0$ is the bare resonator Hamiltonian that makes the field rotate rapidly in phase at the reference frequency even when no drive is applied. $\hat{V}(t)$, on the other hand, contains the slower dynamics of interest. For a microwave resonator one typically has $\hat{H}_0$ on the form defined in Equation (2.16)

$$\hat{H}_0 = \hbar\omega_{\mathrm{r}}\hat{a}^\dagger\hat{a}, \tag{2.16}$$

where ω_r denotes the (bare) angular resonance frequency of the resonator mode in the laboratory frame. The rotating-frame frequency ω_{rf} is a freely chosen reference frequency; often one sets $\omega_{\mathrm{rf}} = \omega_r$. Plugging in the corresponding unitary $\hat{U}(t) = \exp\Big(-i\hat{H}_0 t/\hbar\Big)$ in Equation (2.16), the transformed Hamiltonian becomes Equation (2.17)

$$\hat{H}'(t) = \hat{U}^\dagger(t)\hat{V}(t)\hat{U}(t). \tag{2.17}$$

In this frame the explicit free rotation is removed and the remaining terms appear as effective detunings and slowly varying drive envelopes.
Furthermore, for the choice $\hat{U}(t) = \exp\Big(-i\omega_{\mathrm{rf}} t\hat{a}^\dagger\hat{a}\Big)$, the ladder operators pick up phase factors, as shown in Equation (2.18) and (2.19),

$$\begin{aligned}\hat{a}'(t) &= \hat{U}^\dagger(t)\hat{a}\hat{U}(t)\\ &= \hat{a}e^{-i\omega_{\mathrm{rf}}t},\end{aligned} \tag{2.18}$$

$$\begin{aligned}\hat{a}'^\dagger(t) &= \hat{U}^\dagger(t)\hat{a}^\dagger\hat{U}(t)\\ &= \hat{a}^\dagger e^{+i\omega_{\mathrm{rf}}t}.\end{aligned} \tag{2.19}$$

As a result, terms in the lab-frame Hamiltonian that oscillate rapidly at frequencies near ω_{rf} can become slowly varying (or time-independent) in the rotating frame, which is the main practical advantage of this change of picture.

2.4.1.1 Choice of rotating frame for a parametric pump.

For a Kerr-nonlinear parametric oscillator (KPO) with a two-photon (parametric) drive at angular frequency ω_p, a common choice is to rotate at half the pump frequency, $\omega_{\mathrm{rf}} = \omega_p/2$ [13], [14]. In this frame the resonant part of the two-photon drive becomes slowly varying, while terms oscillating at frequencies near $\pm\omega_p$ are rapidly rotating and can be neglected under the Rotating-wave approximation discussed next (see Section 2.4.2) .

2.4.2 Rotating-wave approximation (RWA)

After transforming to a frame rotating at a chosen reference frequency ω_{rf}, the Hamiltonian still generally contains terms oscillating at $\pm 2\omega_{\mathrm{rf}}$ (and higher harmonics, i.e. oscillations at integer multiples of the rotating-frame frequency). The rotating-wave approximation (RWA) consists of neglecting these rapidly rotating contributions, keeping only the near-resonant terms that vary slowly on the timescales set by the effective dynamics. Physically, the discarded terms average to (almost) zero over

many cycles of the fast rotation and therefore have a weak net effect on the evolution [16].
As an example, consider a parametrically pumped Kerr resonator in the lab frame, where the two-photon drive contains terms of the form $\propto p(t)(\hat{a}^{\dagger 2}e^{-i\omega_p t} + \hat{a}^2 e^{+i\omega_p t})$. In the frame rotating at $\omega_{\mathrm{rf}} = \omega_p/2$, the resonant components become slowly varying, while counter-rotating contributions oscillate at $\pm 2\omega_{\mathrm{rf}} = \pm\omega_p$ and are dropped under the RWA. The resulting effective KPO Hamiltonian then takes the form presented later in Equation (2.21), with detuning $\Delta = \omega_{\mathrm{KPO}} - \omega_p/2$, where ω_{KPO} denotes the relevant bare resonance frequency of the nonlinear oscillator mode [13].
The validity of the RWA requires a separation of time scales, more specifically, the remaining dynamics must be slow compared to ω_{rf}. For the KPO this means that the Kerr nonlinearity K, the pump amplitude $|p(t)|$, and relevant dissipation rates should satisfy Equation (2.20) (see Section 2.5.1 for details regarding the parameters)

$$K,\ |p(t)|,\ \kappa_{\mathrm{ex}} \ll \omega_{\mathrm{rf}}, \tag{2.20}$$

and that the pump envelope $p(t)$ varies slowly on the scale $1/\omega_{\mathrm{rf}}$ [13], [16]. When these conditions hold, the RWA yields an accurate effective description in which the parametric drive appears as a stationary two-photon term in the rotating frame [13].

2.5 Two-component cat-qubit Hamiltonian and logical gates

This section introduces the Hamiltonian description and control primitives for a two-component cat qubit realized in a two-photon-driven Kerr-nonlinear parametric oscillator (KPO). Cat-state preparation via adiabatic pumping and acceleration using shortcut-to-adiabaticity (STA) are then reviewed. Finally, logical control within the manifold is discussed.

2.5.1 Effective KPO Hamiltonian

A two-photon-driven Kerr-nonlinear parametric oscillator (KPO) is a nonlinear resonator driven by a two-photon parametric pump. As the pump amplitude increases, the system undergoes a bifurcation that gives rise to two stable, classically distinct oscillation states that differ in phase by π. In the quantum regime, an adiabatic increase of the pump amplitude can prepare the oscillator in a coherent superposition of these two states, corresponding to a cat-like state of the resonator field [13], [14], [17].
A standard approach for generating a propagating microwave quantum state in superconducting circuits is to first prepare the desired state in a harmonic-oscillator cavity and subsequently release it into a transmission line through a nonlinear superconducting element, typically a transmon-based interface. In such architectures, the release process can be controlled and temporally shaped, allowing the outgoing wave packet to acquire a desired envelope. This capability is useful both for high-efficiency quantum state transfer to a remote cavity and for generating entanglement between stationary and propagating modes [18], [19].

In the present context, however, a different architecture is of interest. Although tunable couplers enable controlled release, the Josephson nonlinearity responsible for tunability generally also induces effective nonlinear terms. As a result, the photon-number content of the state may become coupled to its spatiotemporal structure, such that the emitted radiation is no longer well described by a single propagating mode. Instead, multiphoton states may acquire an inherently multimode character, which is undesirable when the objective is to generate a well-defined traveling quantum state [20].
To avoid this complication, the tunable coupler is omitted and the Kerr-nonlinear parametric oscillator (KPO) is coupled directly to the waveguide. In this setting, the cat-like quantum state is not first prepared as a stationary cavity state and subsequently released. Rather, the state is generated directly in the propagating mode of the waveguide during the emission process itself. The KPO thereby constitutes the nonlinear element that both supports cat-state physics and enables the formation of the outgoing field [13].
Working in a frame rotating at half the pump frequency ($\omega_{\mathrm{rf}} = \omega_p/2$) and applying the rotating-wave approximation an effective Hamiltonian for a two-photon-driven KPO can be written as Equation (2.21) [13]

$$\hat{H}_{\mathrm{KPO}}(t) = \frac{p(t)}{2}(\hat{a}^{\dagger 2} + \hat{a}^2) - \frac{K}{2}\hat{a}^{\dagger 2}\hat{a}^2 + \Delta\hat{a}^\dagger\hat{a}. \tag{2.21}$$

Here $\hat{a}$ and $\hat{a}^\dagger$ are the annihilation and creation operators of the oscillator mode, K is the Kerr nonlinearity, Δ is the detuning and $p(t)$ is the two-photon pump amplitude [13]. Physically, the Kerr term is responsible for the anharmonicity that allows the oscillator to explore nonclassical states. The two-photon drive, in turn, creates a double-well structure in phase space that supports cat-like superpositions [13].
A key property of the Hamiltonian in Equation (2.21) is its symmetry under the transformation $\hat{a} \to -\hat{a}$ when $\Delta = 0$. Equivalently, the Hamiltonian commutes with the photon-number parity operator, since $\hat{\Pi}\hat{a}\hat{\Pi}^\dagger = -\hat{a}$ and therefore $\hat{\Pi}\hat{a}^2\hat{\Pi}^\dagger = \hat{a}^2$ (and similarly for $\hat{a}^{\dagger 2}$). Because the Kerr term and the two-photon term contain only even powers of $\hat{a}$ and $\hat{a}^\dagger$, they preserve photon-number parity. Thus, on resonance ($\Delta = 0$) one has Equation (2.22)

$$[\hat{H}_{\mathrm{KPO}}(t), \hat{\Pi}] = 0, \qquad (\Delta = 0), \tag{2.22}$$

and the dynamics do not mix even and odd Fock sectors.
The Hamiltonian in Equation (2.21) supports a low-energy manifold spanned (approximately) by two coherent states with opposite phase. This can be seen most transparently in the resonant case $\Delta = 0$, where (up to an additive constant) the KPO Hamiltonian can be rewritten in the factorized form presented in Equation (2.23) [13]

$$\hat{H}_{\mathrm{KPO}}(t) = -\frac{K}{2}(\hat{a}^{\dagger 2} - \frac{p(t)}{K})(\hat{a}^2 - \frac{p(t)}{K}). \tag{2.23}$$

This form makes it clear that states satisfying $\hat{a}^2 |\psi\rangle \approx \frac{p(t)}{K} |\psi\rangle$ have low energy. Coherent states $|\alpha\rangle$ are eigenstates of $\hat{a}$, and therefore also satisfy $\hat{a}^2 |\alpha\rangle = \alpha^2 |\alpha\rangle$.

Consequently, the coherent amplitudes $\alpha(t)$ that minimize the effective energy obey Equation (2.24)

$$\alpha(t)^2 \approx \frac{p(t)}{K}, \qquad \Rightarrow \qquad \alpha(t) \approx \pm\sqrt{\frac{p(t)}{K}}. \tag{2.24}$$

This relation is also useful for understanding how the energy-level spacings depend on K and α. Writing the Hamiltonian in terms of $\alpha^2 \approx p/K$ shows that K sets the overall energy scale of the spectrum, while α controls its dimensionless structure and, in particular, the separation between the parity branches. As a result, increasing K rescales all eigenenergies and hence all level spacings by the same factor, whereas increasing $|\alpha|$ changes the relative spacing between the low-energy cat manifold and the higher excited states. In the large-$|\alpha|$ regime, the gap from the cat manifold to the first excited states grows approximately as $4K|\alpha|^2$, while the splittings between the even- and odd-parity excited-state doublets become progressively smaller as $|\alpha|^2$ increases, with higher doublets requiring larger values of $|\alpha|$ before becoming nearly degenerate [21]. This low-lying structure is illustrated schematically in Figure 2.3, where δ_1 denotes the splitting within the first excited doublet and ΔE_{10} denotes the gap from the cat manifold to the first excited manifold.

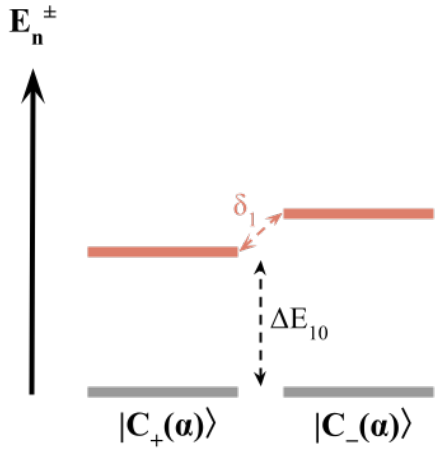

Figure 2.3: Schematic illustration of the low-lying energy-level structure of the resonant KPO. The two lower gray levels represent the even- and odd-parity states forming the cat manifold, while the two upper red levels represent the first excited even/odd doublet. The quantity δ_1 denotes the splitting within the first excited doublet, $\delta_1 = |E_1^- - E_1^+|$, where $E_1^\pm$ are the first excited odd- and even-parity eigenenergies. The quantity ΔE_{10} denotes the gap between the cat manifold and the first excited manifold. In the large-$|\alpha|$ regime, ΔE_{10} grows approximately as $4K|\alpha|^2$, while δ_1 decreases as $|\alpha|^2 = p/K$ increases [21].

Because $\hat{H}_{\mathrm{KPO}}(t)$ preserves photon-number parity on resonance, the eigenstates in the low-energy sector can be chosen to have definite parity. The corresponding even- and odd-parity superpositions of the two coherent components are the two-component cat states introduced in Equation (2.6), with parity eigenvalues $\hat{\Pi}\,|C_\pm(\alpha)\rangle = \pm\,|C_\pm(\alpha)\rangle$. For sufficiently large $|\alpha|$ the overlap $\langle\alpha|-\alpha\rangle = e^{-2|\alpha|^2}$ is exponentially small, and $|C_+(\alpha)\rangle$ and $|C_-(\alpha)\rangle$ form an approximately orthonor-

mal basis for a two-dimensional manifold [13]. Throughout this thesis, this manifold will be referred to as the *cat manifold*.

2.5.2 Adiabatic preparation of cat states

A common approach to generate two-component cat states in a KPO is to initialize the resonator near the vacuum and adiabatically ramp the two-photon pump amplitude $p(t)$ from 0 to a final value p_0 [13], [14]. If the ramp is slow compared to the inverse energy gap separating the low-energy manifold from higher-lying excitations, the dynamics are well described by the adiabatic approximation, meaning that the state remains close to an instantaneous low-energy eigenstate of the time-dependent Hamiltonian $\hat{H}_{\mathrm{KPO}}(t)$ throughout the ramp.
Because the resonant KPO Hamiltonian preserves photon-number parity, the even and odd sectors evolve independently. Starting from the vacuum state, which has even parity, an adiabatic ramp of the pump therefore prepares an even cat state at the final pump strength, p_0, as presented in Equation (2.25) [13]

$$\begin{aligned} &|0\rangle \xrightarrow[\text{adiabatic ramp}]{p:0\to p_0} |C_+(\alpha_0)\rangle\,, \\ &\alpha_0 = \sqrt{p_0/K}, \\ &p_0 = p(t_0). \end{aligned} \tag{2.25}$$

Similarly, if the system is initialized in the odd-parity sector (e.g. $|1\rangle$), the adiabatic ramp connects to the odd cat state $|C_-(\alpha_0)\rangle$ [13]. In this way, adiabatic pumping provides a direct route to preparing parity-defined cat states that form the logical basis, presented in Equation (2.8), of the two-component cat qubit.
According to Goto *et al.* leakage during the cat-state preparation can degrade the state fidelity for the traveling cat and it is therefore of interest to speed up the preparation [13]. On the other hand, if the two-photon pump is ramped up too quickly, the evolution is no longer adiabatic and the state can suffer from non-adiabatic excitations. Goto *et al.* demonstrated this effect explicitly by increasing the bandwidth of the pump-shaping filter which yielded oscillations in the intracavity observables and reduced the fidelity of the generated cat state [13]. This motivates the use of acceleration techniques, such as shortcut-to-adiabaticity (STA), discussed in the next subsection (see Section 2.5.3).

2.5.3 Shortcut-to-adiabaticity (STA) for accelerated preparation

Goto *et al.* introduces the Shortcut-to-adiabaticity (STA) technique to reproduce the outcome of adiabatic evolution without requiring an extremely slow ramp of the pump [13]. The general idea of STA is to add a counterdiabatic term $\hat{H}_{\mathrm{counter}}(t)$ to the Hamiltonian, designed to suppress the unwanted transitions that would otherwise occur for a finite-speed ramp. In Equation (2.26) the general definition of such

a counterdiabatic Hamiltonian is presented

$$\hat{H}_{\text{counter}}(t) = \frac{i}{2}\sum_n (\left|\dot{\phi}_n\right\rangle \langle\phi_n| - |\phi_n\rangle \left\langle\dot{\phi}_n\right|), \tag{2.26}$$

where $|\phi_n\rangle$ is the nth instantaneous eigenstate of the reference Hamiltonian. This Hamiltonian is essentially compensating for the eigenbasis change in time and suppresses unwanted transitions between eigenstates [22].
In the two-photon-driven KPO model used by Goto *et al.* an approximate counterdiabatic Hamiltonian of the form presented in Equation (2.27) is used

$$\begin{aligned} \hat{H}_{\text{counter}}(t) &= i\frac{p'(t)}{2}(\hat{a}^{\dagger 2} - \hat{a}^2) \\ p'(t) &= \frac{\dot{p}(t)}{p(t)} \tanh\frac{p(t)}{K}, \end{aligned} \tag{2.27}$$

where $p'(t)$ acts as an imaginary pump amplitude added to the usual real pump $p(t)$ [13]. Numerically, Goto *et al.* shows that including this STA term suppresses the non-adiabatic oscillations and improves the final cat-state fidelity, especially for faster pump ramps [13].

2.5.4 Logical X_L and equatorial rotations from a one-photon drive

Because $\hat{H}_{\text{KPO}}(t)$ conserves photon-number parity, it cannot on its own drive transitions between $|C_+\rangle$ and $|C_-\rangle$. A logical X_L rotation therefore requires an additional control term that breaks parity, such as a one-photon drive [17], [23]. A one-photon drive on the oscillator mode can be modeled as Equation (2.28)

$$\hat{H}_\varepsilon(t) = \varepsilon(t)(\hat{a} + \hat{a}^\dagger), \tag{2.28}$$

where $\varepsilon(t)$ is a real-valued envelope [10]. Since $\hat{a}$ changes the photon number by one, $\hat{H}_\varepsilon(t)$ does not conserve parity, instead mixing even and odd Fock sectors and thus couples the logical basis states $|0_L\rangle \equiv |C_+(\alpha)\rangle$ and $|1_L\rangle \equiv |C_-(\alpha)\rangle$.
To understand the logical action of $\hat{H}_\varepsilon(t)$, one can project Equation (2.28) onto the cat manifold. Using $\hat{a}\,|\alpha\rangle = \alpha\,|\alpha\rangle$ and the definitions of $|C_\pm(\alpha)\rangle$, the annihilation operator approximately maps even and odd cats into each other for sufficiently large $|\alpha|$, as presented in Equation (2.29)

$$\hat{a}\,|C_\pm(\alpha)\rangle \approx \alpha\,|C_\mp(\alpha)\rangle \tag{2.29}$$

(and similarly for $\hat{a}^\dagger$). Neglecting small corrections due to the finite overlap $\langle\alpha|{-\alpha}\rangle$ and leakage outside the manifold, Equation (2.29) implies that the one-photon drive acts approximately as a Pauli X-operator in the logical basis.
The approximation in Equation (2.29) is valid when the one-photon drive is sufficiently weak so that it does not significantly populate states outside the cat manifold. This requires the one-photon drive to be weak compared to the mechanism that confines the dynamics to the cat manifold (e.g. the two-photon stabilization rate), so that leakage outside the manifold remains negligible [10].

2.5.5 Two-photon dissipative confinement

Subsections 2.5.1-2.5.4 described *Kerr Hamiltonian confinement* of a cat manifold using the Kerr-nonlinear parametric-oscillator (KPO) Hamiltonian in Equation (2.21), where the interplay of a two-photon drive and a Kerr nonlinearity generates an effective double-well structure in phase space and yields cat-like eigenmanifolds. The present subsection introduces the complementary concept of *two-photon dissipative confinement*, where appropriately engineered dissipation together with a two-photon pump can stabilize a cat-qubit manifold as an attractor (steady-state manifold) of the open-system dynamics, rather than relying exclusively on Hamiltonian spectral structure [10], [21].

The dynamics are generated by the same time-dependent Hamiltonian as in Equation (2.21), but with the Kerr term neglected (i.e. $K = 0$), while a two-photon loss channel is added to the Lindblad master equation, as presented in Equation (2.30),

$$\dot{\rho}(t) = -i[\hat{H}(t), \rho(t)] + \kappa_{\text{ex}}\mathcal{D}[\hat{a}]\rho(t) + \Gamma_2\mathcal{D}[\hat{a}^2]\rho(t). \tag{2.30}$$

Here Γ_2 denotes the effective two-photon loss rate (its relation to the collapse-operator normalization used in simulations is specified in Subsection 3.1.2). See Section 2.6 for definition of κ_{ex}.

The two-photon loss term models irreversible processes in which photons are removed pairwise from the oscillator. Since $\hat{a}^2$ changes the photon number by 2, it preserves photon-number parity. Parity preservation is naturally compatible with cat encodings, where logical states are supported predominantly on (approximately) even/odd superpositions [10].

In the two-photon dissipative-confinement case, the STA correction can be understood as acting in a phase-rotated two-photon quadrature relative to the Kerr-confined case. While the Kerr STA term is proportional to $i(a^{\dagger 2} - a^2)$, the dissipative expression is proportional to $(a^{\dagger 2} + a^2)$, and the counterterm changes to Equation (2.31) [24],

$$\hat{H}^{\text{diss}}_{\text{counter}}(t) = \frac{p'(t)}{4}(\hat{a}^{\dagger 2} + \hat{a}^2). \tag{2.31}$$

In the two-photon dissipative-confinement picture, the cat-qubit manifold is not protected by an energy gap, but is instead stabilized as the steady-state manifold of an engineered two-photon loss process. In this setting, weak one-photon driving can still induce logical rotations, but the underlying mechanism differs from the Kerr case: the dynamics can be understood in terms of quantum Zeno dynamics, where the continuous two-photon dissipation acts as a measurement-like process that continuously drives the state back toward the cat-qubit subspace while the weak drive generates an effective evolution within that subspace [10]. This picture requires the applied drive to remain small compared to the two-photon dissipation rate in order for the logical dynamics to remain approximately unitary within the protected manifold [10].

This distinction is important when comparing dissipative and Hamiltonian confinement for driven logical operations. In a purely dissipative gate, the Zeno mechanism keeps the state close to the cat manifold, but higher-order corrections can lead to

effective phase decoherence and associated nonadiabatic phase errors [21]. By contrast, in a Hamiltonian-confinement scheme such as the Kerr model, the cat-qubit manifold is a gapped eigenspace, so sufficiently smooth driving can suppress transitions outside the logical subspace exponentially in the gate time [21]. Purely dissipative confinement is therefore highly effective as a stabilization mechanism, but it generally imposes stronger constraints on coherent gate performance than a gapped Hamiltonian confinement scheme [21].

2.6 Emission into a transmission line: open-system description

A key ingredient in this work is that the KPO is not perfectly isolated, but is intentionally coupled to a one-dimensional output channel. This coupling allows photons to leak out at an external coupling rate κ_{ex}, thereby converting an intracavity quantum state into a propagating microwave field. Goto *et al.* uses a standard system-bath model and writes the total Hamiltonian as Equation (2.32) [13]

$$\hat{H}(t) = \hat{H}_{\mathrm{KPO}}(t) + \hat{H}_{\mathrm{out}} + \hat{H}_{\mathrm{c}}. \tag{2.32}$$

Here, $\hat{H}_{\mathrm{out}}$ is the Hamiltonian of the continuum of transmission-line modes, presented in Equation (2.33), where $\hat{b}$ and $\hat{b}^\dagger$ are the annihilation and creation operators for photons of frequency $\omega_p/2 + \omega$ in the output mode. Furthermore, $\hat{H}_{\mathrm{c}}$ is the the coupling between the KPO mode $\hat{a}$ and the output field modes, presented in Equation (2.34) [13]

$$\hat{H}_{\mathrm{out}} = \int_{-\infty}^{\infty} \omega \hat{b}^\dagger(\omega)\hat{b}(\omega)d\omega \tag{2.33}$$

$$\hat{H}_{\mathrm{c}} = i\sqrt{\frac{\kappa_{\mathrm{ex}}}{2\pi}} \int_{-\infty}^{\infty} [\hat{b}^\dagger(\omega)\hat{a} - \hat{a}^\dagger\hat{b}(\omega)]d\omega. \tag{2.34}$$

In this description, κ_{ex} sets the energy decay rate of the intracavity mode due to emission into the transmission line [13]. Throughout, Goto *et al.* uses units where $\hbar = \upsilon_p = 1$, with υ_p the phase velocity of the propagating output field [13].
If one is primarily interested in the intracavity state, the output channel can be traced out, where the reduced density matrix of the KPO mode obeys a Lindblad master equation of the form presented in Equation (2.35)

$$\begin{aligned} \dot{\rho}_s(t) &= -i[\hat{H}_{\mathrm{KPO}}(t), \rho_s(t)] + \kappa_{\mathrm{ex}}\mathcal{D}(\hat{a})\rho_s(t) \\ \mathcal{D}(\hat{a})\rho_s(t) &= \hat{a}\rho_s(t)\hat{a}^\dagger - \frac{1}{2}(\{\hat{a}^\dagger\hat{a}, \rho_s(t)\}). \end{aligned} \tag{2.35}$$

Here, the emission channel is described by the Lindblad jump operator $\hat{L} = \sqrt{\kappa_{\mathrm{ex}}}\hat{a}$ [13]. Physically, the dissipator $\mathcal{D}[\hat{L}]$ describes irreversible energy flow from the intracavity mode into traveling modes of the line. In the absence of coherent driving and other dissipation channels, Equation (2.35) implies that the mean intracavity photon number decays as Equation (2.36)

$$\frac{d}{dt}\langle \hat{a}^\dagger \hat{a}\rangle(t) = -\kappa_{\mathrm{ex}}\langle \hat{a}^\dagger \hat{a}\rangle(t), \tag{2.36}$$

i.e. $\langle \hat{a}^\dagger \hat{a}\rangle(t) \propto e^{-\kappa_{\mathrm{ex}} t}$, which corresponds to emission into the line.
To connect this intracavity loss channel to the propagating output field, one uses input-output theory. In the Markov approximation, the coupling of a localized quantum system to a one-dimensional continuum yields the boundary condition in Equation (2.37) [25]

$$\hat{b}_{\mathrm{out}}(t) = \hat{b}_{\mathrm{in}}(t) + \hat{L}(t), \tag{2.37}$$

where $\hat{b}_{\mathrm{in}}(t)$ and $\hat{b}_{\mathrm{out}}(t)$ are the incoming and outgoing traveling-field operators and $\hat{L}(t) = \sqrt{\kappa_{\mathrm{ex}}}\,\hat{a}(t)$ is the jump operator associated with emission into that port.
Goto *et al.* emphasize that any quantum state inside a linear cavity is released into a traveling pulse in the same quantum state, with an exponentially decaying temporal envelope set by the cavity decay [13]. This motivates the picture that the outgoing radiation from a linear cavity can be well described by a single dominant temporal mode.
For a KPO, the above linear-cavity intuition does not automatically apply. During emission, the intracavity state continues to evolve under the nonlinear Kerr Hamiltonian, which can imprint photon-number-dependent phases and thereby distort the state of the emitted traveling pulse [13]. Goto *et al.* propose to avoid this distortion by shaping the two-photon pump amplitude $p(t)$ during the release such that the KPO behaves effectively as a linear cavity [13].
Goto *et al.* show that once the intracavity cat state has formed, its coherent components $|\pm\alpha\rangle$ approximately satisfy $\alpha^2 \approx p/K$ [13]. Under external damping, $\alpha(t)$ decays as $\alpha(t) = \alpha_0 e^{-\kappa_{\mathrm{ex}}(t-t_0)/2}$. If one simultaneously chooses the pump to decay as Equation (2.38)

$$p(t) = p(t_0)e^{-\kappa_{\mathrm{ex}}(t-t_0)}, \tag{2.38}$$

then the relation $\alpha(t)^2 = p(t)/K$ is maintained during the release and the factorized structure in Equation (2.23) implies that the photon-number-dependent phase evolution generated by the Kerr nonlinearity is strongly suppressed while photons leak out. As a result, the prepared intracavity cat state can be emitted into the line with high fidelity [13].
A related physical picture is given by Khanahmadi and Mølmer, who show that in direct generation of traveling non-Gaussian states, the temporal profile of the drive can determine the shape of the propagating wave packet. While their setup differs from the KPO considered here, this supports the expectation that the dominant emitted mode should be closely connected to the pump-defined intracavity amplitude rather than being selected arbitrarily by the capture procedure [24]. In the present setting, this suggests using the profile associated with $\alpha(t)^2 = p(t)/K$ as a physically motivated reference for the emitted wave packet.

2.7 Temporal-mode decomposition and virtual-cavity capture

This section introduces the temporal-mode framework used to characterize the radiation emitted from the KPO and to extract the quantum state of a selected outgoing wavepacket.

2.7.1 Temporal-mode decomposition and single-modality

To characterize the temporal structure of the emitted radiation from the KPO, one can introduce the first-order correlation function of the output field, presented in Equation (2.39)

$$g^{(1)}(t,t') = \langle \hat{b}^\dagger_{\text{out}}(t)\hat{b}_{\text{out}}(t')\rangle. \tag{2.39}$$

In the common case where the input is vacuum in the relevant output channel, the output correlations reduce to Equation (2.40)

$$g^{(1)}(t,t') = \langle \hat{L}^\dagger(t)\hat{L}(t')\rangle. \tag{2.40}$$

which can be evaluated from the system dynamics, by the quantum regression theorem [12].
A traveling quantum field generally occupies a continuum of temporal degrees of freedom. A convenient discrete description is obtained by introducing normalized temporal mode functions $v(t)$ on a time interval $[0,T]$ (chosen long enough that the emission is essentially complete) and defining the associated wavepacket annihilation operator as Equation (2.41) [12]

$$\begin{aligned} \hat{a}_v &= \int_0^T v^*(t)\hat{b}_{\text{out}}(t)dt \\ \int_0^T |v(t)|^2 dt &= 1. \end{aligned} \tag{2.41}$$

If the set, $\{v_i(t)\}$, are orthonormal, $\int_0^T v_i^*(t)v_j(t)dt = \delta_{ij}$, then the corresponding $\hat{a}_{v_i}$ satisfy bosonic commutation relations, as presented in Equation (2.42), and represent independent temporal modes

$$\begin{aligned} [\hat{a}_{v_i}, \hat{a}^\dagger_{v_j}] &= \delta_{ij} \\ [\hat{a}^{(\dagger)}_{v_i}, \hat{a}^{(\dagger)}_{v_j}] &= 0. \end{aligned} \tag{2.42}$$

The mean photon number in the mode v is given by Equation (2.43)

$$\begin{aligned} n_v &= \langle \hat{a}^\dagger_v \hat{a}_v \rangle \\ &= \langle \int_0^T dt \int_0^T dt' v(t)\hat{b}^\dagger_{\text{out}}(t)v^*(t')\hat{b}_{\text{out}}(t')\rangle \\ &= \int_0^T dt \int_0^T dt' v(t)g^{(1)}(t,t')v^*(t') \end{aligned} \tag{2.43}$$

Kiilerich and Mølmer shows that the autocorrelation function can be rewritten in eigenmode decomposition, presented in Equation (2.44)

$$g^{(1)}(t,t') = \sum_i n_i v_i^*(t) v_i(t'), \tag{2.44}$$

where $n_i \geq 0$ is the mean population (photon number) in the temporal mode $v_i(t)$ [12]. From now on, the mode with the largest eigenvalue, (n_1, v_1), will be referred to as the *dominant temporal mode*.
A compact measure of how close the emission is to single-mode is the modal purity, defined in Equation (2.45),

$$\eta_{\text{mode}} \equiv \frac{n_1}{\sum_i n_i}, \tag{2.45}$$

which approaches unity when nearly all emitted photons populate a single temporal mode and decreases as the field becomes multimode [12].

2.7.2 Virtual-cavity capture and state diagnostics

The autocorrelation function $g^{(1)}(t,t')$ reveals the temporal mode structure and populations of the emitted field, but obtaining the density matrix of a specific mode requires an extended description. Kiilerich and Mølmer introduce a powerful construction for this purpose, a virtual cavity placed downstream of the source and coupled in a time-dependent way such that it absorbs a chosen outgoing temporal mode [12].
Let's consider $v_i(t)$ to be the target mode and $\hat{a}_{v_i}$ to denote the annihilation operator of the virtual cavity mode that will store the captured state. In the ideal unidirectional setting, the virtual cavity is driven by the output of the source, but it does not feed back into the source. The required time-dependent coupling rate is presented in Equation (2.46)

$$g_{v_i}(t) = -\frac{v_i^*(t)}{\sqrt{\int_0^t dt' |v_i(t')|^2}}, \tag{2.46}$$

which ensures that the incoming wave packet is absorbed without reflection in the ideal limit [12].
The virtual cavity construction can be implemented by using the theory of cascaded quantum systems [12]. For a source system with coupling operator $\hat{L}_s$ and a downstream virtual cavity mode $\hat{a}_{v_i}$, the combined (source $\otimes$ virtual-cavity) state, ρ_{sv}, obeys a Lindblad master equation where the cascade produces an interference between emission from the source and absorption by the virtual cavity [12]. The joint jump operator and Hamiltonian for the casacaded systems are presented in Equation (2.47)

$$\begin{aligned}
\hat{L}_{\text{sv}}(t) &= \hat{L}_s + \hat{L}_v(t) \\
&= \sqrt{\kappa_{ex}}\hat{a} + g_{v_i}^*(t)\hat{a}_{v_i}, \\
\hat{H}_{\text{sv}}(t) &= \hat{H}_{\text{s}}(t) + \hat{H}_{\text{cross}}(t) \\
&= \hat{H}_{\text{s}}(t) + \frac{i\sqrt{\kappa_{\text{ex}}}}{2}(g_{v_i}^*(t)\hat{a}^\dagger\hat{a}_{v_i} - g_{v_i}(t)\hat{a}_{v_i}\hat{a}),
\end{aligned} \tag{2.47}$$

where the cascaded Hamiltonian cross term, $\hat{H}_{\text{cross}}(t)$, enforces unidirectional coupling [12].
Solving the cascaded master equation, presented in Equation (2.48), yields the joint density matrix $\rho_{sv}(t)$

$$\dot{\rho}_{\text{sv}}(t) = -i[\hat{H}_{\text{sv}}(t), \rho_{\text{sv}}(t)] + \mathcal{D}(\hat{L}_{\text{sv}}(t))\rho_{\text{sv}}(t). \tag{2.48}$$

The quantum state stored in the virtual cavity at the end of the emission (at time T) is then obtained by tracing out the source degrees of freedom, as Equation (2.49) shows

$$\rho_{\text{v}}(T) = \text{Tr}_{\text{s}}\{\rho_{\text{sv}}(T)\}. \tag{2.49}$$

By construction, $\rho_{\text{v}}(T)$ is (ideally) the quantum state of the outgoing temporal mode $v(t)$, represented in a discrete Fock basis of the virtual cavity [12].
A useful scalar measure of the mixedness of a quantum state is the purity. For a density operator ρ on a finite-dimensional Hilbert space, the purity is defined as, $\text{Tr}\{\rho^2\}$, and satisfies $0 < \text{Tr}\{\rho^2\} \leq 1$ [26]. The upper bound $\text{Tr}\{\rho^2\} = 1$ holds if and only if ρ is a pure state ($\rho = |\psi\rangle \langle\psi|$), whereas $\text{Tr}\{\rho^2\} < 1$ indicates a mixed state ($\rho = \sum_i p_i |\psi_i\rangle \langle\psi_i|$) [26].
The purity is particularly informative when the overall state is (approximately) pure, in that case, a reduction in $\text{Tr}\{\rho^2_{\text{KPO}}\}$ (equivalently $\text{Tr}\{\rho^2_v\}$) directly reflects entanglement between the KPO and the virtual mode.

3
Methods

This chapter describes the models, numerical methods, and evaluation procedures used in the thesis. First, the full open-system model is introduced for both the Kerr-confinement and two-photon dissipative-confinement cases, including the description of the emitted field and its capture into a virtual cavity. Next, the parametrization of the control pulses is presented, including the low-pass-filter based pulse shapes for the pump and and one-photon drive as well as the STA contribution. The chapter then summarizes the numerical implementation, truncation choices, calibration of pulse amplitudes to target output photon numbers, and the metrics used to quantify fidelity, mode selectivity, and state quality of the captured propagating mode.

3.1 Full system model

This section specifies the open-system model corresponding to the full setup shown schematically in Figure 3.1.
The system consisted of a KPO coupled to a one-dimensional output channel (transmission line) which in turn was coupled to a virtual cavity. The transmission line was treated as a Markovian bath and was traced out, resulting in a Lindblad master equation for the reduced state of the KPO, as given in Equation (2.35). To obtain a density-matrix description of a selected propagating temporal mode of the emitted field, the model was extended by introducing a downstream virtual cavity that absorbed the chosen mode. The virtual cavity was included explicitly as an additional bosonic degree of freedom and was coupled to the KPO in a cascaded (unidirectional) manner as described in Section 2.7.

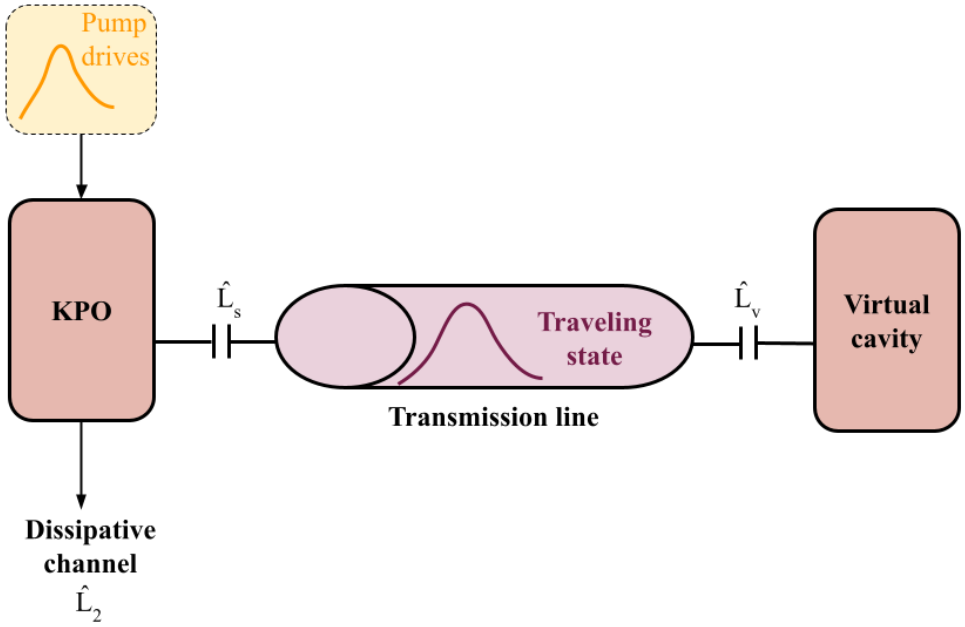

Figure 3.1: Schematic of the effective model used in the simulations. A Kerr-nonlinear parametric oscillator (KPO) is driven by shaped pump pulses and emits into a one-dimensional output channel, producing a propagating quantum state. Dissipation is represented by Lindblad channels, where $\hat{L}_s$ denotes coupling of the KPO to the monitored output port (source emission into the transmission line). In the alternative dissipative-confinement model (where Kerr nonlinearity is set to zero), two-photon loss is included via the channel $\hat{L}_2$. To obtain a density-matrix description of a selected traveling temporal mode, a downstream virtual cavity is introduced and coupled in a cascaded (unidirectional) manner; $\hat{L}_v$ denotes the time-dependent absorption channel that maps the chosen output wave packet onto the virtual-cavity state $\rho_v(T)$.

3.1.1 KPO Hamiltonian and dissipative coupling

The coherent KPO dynamics were governed by the effective Hamiltonian $\hat{H}_{\mathrm{KPO}}(t)$ introduced in Equation (2.21). In addition, the model optionally included a one-photon rotation drive $\hat{H}_{\varepsilon}(t)$ (Equation (2.28)) and a shortcut-to-adiabaticity (STA) correction $\hat{H}_{\mathrm{counter}}(t)$ (Equation (2.27)). The explicit construction of the time-dependent envelopes that entered these Hamiltonian terms is given in Section 3.2. Coupling to the monitored output channel was treated within the Born-Markov approximation and is described by the Lindblad master equation in Equation (2.35). The emission into the output channel was modeled by the collapse operator in Equation (3.1)

$$\hat{L}_s = \sqrt{\kappa_{\mathrm{ex}}}\hat{a}, \tag{3.1}$$

where κ_{ex} is the external coupling rate and $\hat{a}$ is the KPO annihilation operator. When included, pure dephasing and one-photon loss was modeled by two additional collapse operators $\hat{L}_\phi$ respectively $\hat{L}_1$, defined in Equation (3.2) respectively (3.3),

$$\hat{L}_\phi = \sqrt{\kappa_\phi}\hat{a}^\dagger\hat{a}, \tag{3.2}$$

corresponding to a dephasing dissipator $\kappa_\phi \mathcal{D}[\hat{a}^\dagger \hat{a}]$ in the master equation, and

$$\hat{L}_1 = \sqrt{\kappa_1}\hat{a}, \tag{3.3}$$

corresponding to a one-photon loss dissipator $\kappa_1 \mathcal{D}[\hat{a}]$ in the master equation.

3.1.2 Two-photon-loss (dissipative-confinement) model

In addition to the Kerr-based reference model, a two-photon dissipative-confinement model was studied in which the Hamiltonian confinement mechanism was replaced by engineered two-photon loss. More specifically, the coherent dynamics were described by the same time-dependent Hamiltonian contributions as in the Kerr model, the detuning, the two-photon pump $p(t)$, and, when enabled, the one-photon rotation drive $\varepsilon(t)$, while the Kerr nonlinearity was omitted from $\hat{H}_{\mathrm{KPO}}(t)$ and the STA contribution was instead taken to be the counterterm in Equation (2.31).
The open-system evolution was then extended with a two-photon loss collapse operator, presented in Equation (3.4),

$$\hat{L}_2 = \sqrt{2\kappa_2}\hat{a}^2, \tag{3.4}$$

which corresponded to an additional dissipator $2\kappa_2 \mathcal{D}[\hat{a}^2]$ in the master equation.

3.1.3 Temporal-mode description of the emitted field

The emitted traveling field was characterized in terms of temporal modes using the first-order correlation function defined in Equation (2.39), which, for vacuum input in the monitored line, can be expressed in terms of the system coupling operator $\hat{L}_s$ via the input-output relation (Equation (2.37)). In the numerical implementation, $g^{(1)}(t, t')$ was evaluated as a two-time system correlation $\langle \hat{L}_s^\dagger(t) \hat{L}_s(t') \rangle$ on a discrete time grid.
The temporal modes $\{v_i(t)\}$ and their mean photon numbers $\{n_i\}$ were obtained by diagonalizing the correlation kernel as introduced in Equation (2.44), with $n_i \geq 0$ and $v_i(t)$ following the normalization condition in Equation (2.41). Unless otherwise stated, the subsequent capture procedure targeted the most populated mode $v_1(t)$ corresponding to the largest eigenvalue n_1.

3.1.4 Virtual-cavity capture model

To obtain a density matrix for a selected propagating temporal mode, the source system (KPO) was coupled to a downstream virtual cavity mode. The virtual cavity was designed to absorb a chosen temporal mode $v(t)$ of the outgoing field and thereby map the traveling-mode state onto an intracavity state at a final time T (see Section 2.7).
Given a normalized target mode $v(t)$, the mode-matched capture coupling $g_v(t)$ is defined in Equation (2.46). The total Hilbert space was extended to a tensor product of the KPO (dimension d_1) and the virtual cavity (dimension d_2), with virtual-mode annihilation operator $\hat{a}_v$.

The cascaded (unidirectional) coupling between the KPO and the virtual cavity was implemented using the cascaded master-equation structure given in Equation (2.47) and (2.48).
After time evolution to $t = T$, the density matrix of the captured mode was obtained by tracing out the KPO subsystem (Equation 2.49). The captured photon number was computed as presented in Equation (3.5)

$$N_{\text{cap}} = \langle \hat{a}_v^\dagger \hat{a}_v \rangle_{t=T}. \tag{3.5}$$

3.1.5 Hilbert-space truncation and initial states

The KPO mode was simulated in a truncated Fock basis of dimension d_1. The initial KPO state was selected either as a Fock state $|n_{\text{init}}\rangle$ or as a superposition in the $\{|0\rangle, |1\rangle\}$ subspace, presented in Equation (3.6),

$$\begin{aligned} |\psi(0)\rangle &= \sqrt{p_0}\,|0\rangle + e^{i\phi_{\text{init}}}\sqrt{p_1}\,|1\rangle\,, \\ p_0 + p_1 &= 1. \end{aligned} \tag{3.6}$$

When the virtual cavity was included, the initial state of the virtual mode was vacuum $|0\rangle_v$, and the joint initial state was $|\psi(0)\rangle \otimes |0\rangle_v$.

3.2 Control pulses and parametrization

This section describes how the time-dependent control pulses entering the Hamiltonian were constructed and how the main simulation parameters were defined. The time dependence was introduced through the two-photon pump envelope $p(t)$ in $\hat{H}_{\text{KPO}}(t)$ and, when enabled, the one-photon rotation envelope $\varepsilon(t)$ in $\hat{H}_\varepsilon(t)$. When STA was enabled, an auxiliary envelope $p'(t)$ appeared in $\hat{H}_{\text{counter}}(t)$.

3.2.1 Time discretization and spline representation

All time-dependent quantities were evaluated on a uniform grid $t_i \in [0, T]$ with N_T points, as presented in Equation (3.7)

$$\begin{aligned} t_i &= i\Delta t \\ i &= 0, 1, \ldots, N_T - 1 \\ \Delta t &= \frac{T}{N_T - 1}. \end{aligned} \tag{3.7}$$

Discrete pulse samples were represented by spline interpolants to provide smooth time dependence in the QuTiP solver. When time-rescaling was applied (see Equation (3.11) and (3.14)), spline evaluation was clamped to $[0, T]$ to avoid extrapolation.

3.2.2 Two-photon pump pulse $p(t)$ of order n_p

The pump envelope was generated by an n_pth-order low-pass filter (LPF) cascade driven by the input in Equation (3.8),

$$p_{\text{in}}(t) = K_{\text{th}} A e^{-\kappa_{\text{ex}} t}, \tag{3.8}$$

where A is a dimensionless pump amplitude parameter, and K_{th} a Kerr threshold scale, defined in Subsection 3.3.1. By letting $p_0(t) \equiv p_{\text{in}}(t)$, one can define, for $m = 1, 2, \ldots, n_p$, Equation (3.9),

$$p_m(t) = \int_0^t B e^{-B(t-\tau)} p_{m-1}(\tau) d\tau, \tag{3.9}$$

where B is the filter bandwidth. The resulting pump envelope of order n_p is then $p(t; n_p) \equiv p_{n_p}(t)$.
To compare pulse shapes independently of the overall amplitude, a peak-normalized pulse was introduced as presented in Equation (3.10),

$$\begin{aligned} \tilde{p}(t) &\equiv \frac{p(t)}{p_{\max}}, \\ p_{\max} &\equiv \max_{t \in [0,T]} |p(t)|. \end{aligned} \tag{3.10}$$

For example, if a pulse had $p_{\max} = 2.2$ (in the chosen units), the normalization corresponded to the rescaling $p(t) \to p(t)/2.2$, yielding $\max_t |\tilde{p}(t)| = 1$. Unless explicitly stated otherwise, the simulations used the unnormalized pump $p(t)$, while normalized pulses $\tilde{p}(t)$ are only used here for visualization. In Figure 3.2 two-photon pump pulses of different orders n_p are visualized.
An optional pump time scaling was introduced by Equation (3.11)

$$p_{\lambda_p}(t) = p(\lambda_p t), \tag{3.11}$$

where $\lambda_p > 0$ and with endpoint clamping of the spline evaluation as described above.

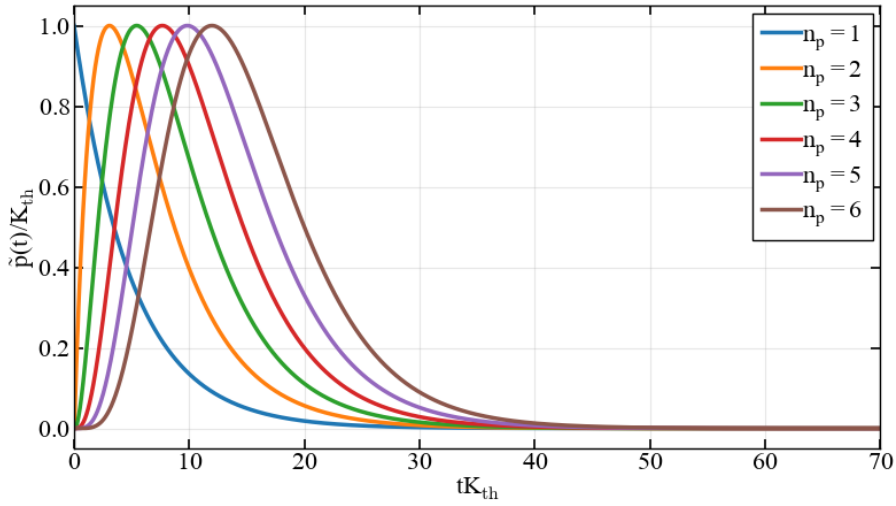

Figure 3.2: Two-photon pump pulse shapes generated by the n_pth-order LPF model. To emphasize differences in temporal shape rather than overall scale, each curve shows the peak-normalized pulse $\tilde{p}(t) = p(t)/p_{\max}$ defined in Equation (3.10), such that $\max_t |\tilde{p}(t)| = 1$. Colored curves correspond to LPF orders $n_p \in \{1, 2, 3, 4, 5, 6\}$. Unless stated otherwise, parameters are fixed to $K_{\text{th}} = 1$, $\kappa_{\text{ex}} = 0.2K_{\text{th}}$, $B = 2.5\,\kappa_{\text{ex}}$, $A = 4.45$, and total duration $T = 70/K_{\text{th}}$. The horizontal axis is shown in dimensionless units tK_{th} and the vertical axis as $\tilde{p}(t)/K_{\text{th}}$

3.2.3 STA auxiliary envelope $p'(t)$

When the STA correction term $\hat{H}_{\text{counter}}(t)$ was enabled, an auxiliary envelope $p'(t)$ was constructed from the pump shape $p(t)$. On the discrete grid, $\dot{p}(t)$ was approximated using a finite-difference gradient. Equation (2.27) was applied pointwise to compute $p'(t)$ while avoiding division by values near zero. Additionally, negative values of $\dot{p}(t)$ were suppressed by setting $p'(t) = 0$ whenever $\dot{p}(t) < 0$, such that the STA correction primarily acted during the pump turn-on and did not introduce an additional quadrature during the release stage.

3.2.4 One-photon rotation pulse $\varepsilon(t)$ of order n_ε

The one-photon rotation pulse $\varepsilon(t)$ entered the Hamiltonian via $\hat{H}_\varepsilon(t)$ (Equation (2.28)). The rotation pulse $\varepsilon(t)$ was generated using an independent LPF order n_ε and a dimensionless input parameter ε_x, which defined the rotation-drive strength via an L^2-normalization relative to the pump pulse. First, a raw envelope $\varepsilon_{\text{raw}}(t) = p(t; n_\varepsilon)$ was constructed using the same LPF procedure as for the two-photon pump (Equation (3.9)), but with order n_ε. The raw envelope was then rescaled such that the integrated pulse energy satisfied Equation (3.12),

$$\int_0^T |\varepsilon(t)|^2 dt = \varepsilon_x^2 \int_0^T |p(t; n_p)|^2 dt, \tag{3.12}$$

yielding Equation (3.13),

$$\varepsilon(t) = \varepsilon_x \sqrt{\frac{\int_0^T |p(t; n_p)|^2 dt}{\int_0^T |\varepsilon_{\mathrm{raw}}(t)|^2 dt}} \varepsilon_{\mathrm{raw}}(t). \tag{3.13}$$

With this convention, $\varepsilon_x = 0.1$ corresponded to a one-photon drive pulse whose integrated intensity was 1% of the two-photon pump intensity over the interval $[0, T]$. For the special case $n_\varepsilon = n_p$, this construction reduced to the proportional relation $\varepsilon(t) = \varepsilon_x p(t; n_p)$.
A separate time scaling for the rotation pulse was introduced by Equation (3.14)

$$\varepsilon_{\lambda_\varepsilon}(t) = \varepsilon(\lambda_\varepsilon t), \tag{3.14}$$

where $\lambda_\varepsilon > 0$ and with spline clamping to $[0, T]$ under rescaling.

3.3 Numerical implementation and evaluation

This section summarizes the numerical configuration used for time evolution and correlation calculations. Furthermore, it outlines validation checks, and defines the metrics used to evaluate emission, mode selectivity, capture and state quality.

3.3.1 Units and normalization

All simulations were performed in dimensionless units by introducing a fixed reference Kerr scale K_{th} as the frequency unit, which will be referred to as the threshold Kerr scale. Times were therefore reported in units of K_{th}^{-1}, i.e. the dimensionless time variable was $K_{\mathrm{th}} t$. Unless explicitly stated otherwise, all rates and drive amplitudes were expressed as fractions of K_{th}, for example Δ/K_{th}, $\kappa_{\mathrm{ex}}/K_{\mathrm{th}}$, and κ_2/K_{th}.
To distinguish between the reference scale used for normalization and the Kerr coefficient appearing in the Hamiltonian, the Kerr coefficient in the Hamiltonian was denoted by K_{ham}.

3.3.2 Default simulation parameters

The simulation time window was chosen as $T = 70/K_{\mathrm{th}}$. The external coupling rate was set proportional to the reference scale, $\kappa_{\mathrm{ex}} = 0.2K_{\mathrm{th}}$ and the LPF bandwidth was chosen as a fixed multiple of κ_{ex}, $B = 2.5\kappa_{\mathrm{ex}}$. Unless otherwise stated, the KPO was initialized in vacuum in the simulations, i.e. $|n_{\mathrm{init}}\rangle = 0$.
The KPO and virtual cavity Hilbert spaces were truncated to $d_1 = d_2 = 20$ in the Kerr confinement simulations and $d_1 = d_2 = 14$ in the two-photon dissipative confinement simulations. The time evolution was discretized into $N_T = 1000$ time steps. The detuning was parametrized as a fraction of the reference scale, $\Delta = \Delta_{\mathrm{frac}} K_{\mathrm{th}}$, with default $\Delta_{\mathrm{frac}} = 0$. By default, no additional dissipative channels were enabled, i.e. $\kappa_1 = 0$, $\kappa_2 = 0$, $\kappa_\phi = 0$. In the Kerr (Hamiltonian) confinement model K_{ham} was set to the threshold value by default, i.e. $K_{\mathrm{ham}} = K_{\mathrm{th}}$. In the two-photon dissipative-confinement model, the Hamiltonian Kerr term was omitted by setting $K_{\mathrm{ham}} = 0$, and confinement was instead introduced via a nonzero two-photon loss

rate $\kappa_2 > 0$. Furthermore, κ_2 was specified as a fraction of K_{th} (i.e. $\kappa_2 = \kappa_{2,\text{frac}} K_{\text{th}}$). In all simulations the Kerr threshold scale was set to $K_{\text{th}} = 1$.
The time-scaling parameters for the two-photon and one-photon drives defaulted to unity, i.e. $\lambda_p = 1$, $\lambda_\varepsilon = 1$. The shortcut-to-adiabaticity (STA) correction was disabled by default. When enabled, an additional imaginary quadrature drive term proportional to $p'(t)$ was included in the Hamiltonian.

3.3.3 Time evolution and correlation calculations

Time evolution of the reduced density matrix was performed using the QuTiP master equation solver `mesolve` on the time grid in Equation (3.7). The final joint state $\rho_{sv}(T)$ was stored for post-processing, whereas storing the full trajectory of density matrices was disabled to reduce memory usage.
Two-time correlations, $g^{(1)}(t, t')$, required for the temporal-mode analysis were computed using QuTiP's two-time correlation functionality. In the implementation, the solver returned the correlation on a triangular (t, τ) domain with $\tau = t' - t$; the Hermitian was constructed by enforcing $g^{(1)}(t, t') = [g^{(1)}(t', t)]^*$.

3.3.4 Convergence and numerical sanity checks

The truncation dimension (d_1, d_2) and the time resolution N_T were chosen such that reported observables were insensitive to further increases. Convergence was assessed by verifying negligible changes in key quantities such as $\langle \hat{a}^\dagger \hat{a} \rangle(t)$, $\langle \hat{a}_v^\dagger \hat{a}_v \rangle(t)$, mode populations $\{n_i\}$, the captured photon number N_{cap}, and state fidelities.
Trace preservation of the Lindblad evolution and positivity of the density matrices were provided by the master-equation solver up to numerical tolerance. Hermiticity of the reconstructed correlation matrix was enforced explicitly by symmetrization.

3.3.5 Amplitude calibration for a target captured photon number

In scans where a fixed captured photon number, N_{cap}, was desired, the pump amplitude A was determined by solving for the value that achieved $N_{\text{cap}} \approx N_{\text{out}}$. This was formulated as the root-finding problem in Equation (3.15),

$$f(A) = N_{\text{cap}}(A) - N_{\text{out}}, \tag{3.15}$$

where each evaluation of $N_{\text{cap}}(A)$ consisted of a full temporal-mode extraction followed by the cascaded capture simulation. A bracketing stage was used to obtain an interval $[A_{\text{lo}}, A_{\text{hi}}]$ satisfying $f(A_{\text{lo}}) f(A_{\text{hi}}) < 0$, which guaranteed (for continuous f) that at least one root lied within the interval.
The root was then computed using Brent's method, which combines the guaranteed convergence of bisection with the faster convergence of interpolation-based updates. Specifically, Brent's method maintained a bracketing interval containing the root and adaptively chose between a bisection step and an interpolation step. When the interpolation step was expected to be reliable it was used to accelerate convergence; otherwise the method fell back to bisection to preserve robustness. The procedure

terminated when the interval width and/or the function value satisfied specified absolute and relative tolerances, and the final bracket together with the achieved value of N_{cap} was stored. In the implementation, the Brent solver ran with absolute and relative tolerances $\texttt{xtol} = 10^{-6}$ and $\texttt{rtol} = 10^{-6}$ and a maximum of $\texttt{maxiter} = 100$ iterations.

3.3.6 Evaluation metrics and state-quality benchmarks

Photon-number and efficiencies were defined from the pump and mode decomposition. The pump feed was defined as Equation (3.16)

$$N_{\mathrm{feed}} = \int_0^T |p(t)|^2 dt, \tag{3.16}$$

the total emitted photon number was $N_{\mathrm{get}} = \sum_i n_i$, the selected-mode population was $N_{\mathrm{top}} = n_1$, and the captured photon number was N_{cap} (defined in Equation (3.5)). From these quantities, emission, mode selectivity and capture efficiencies were computed according to Equation (3.17),

$$\begin{aligned} \eta_{\mathrm{emit}} &= \frac{N_{\mathrm{get}}}{N_{\mathrm{feed}}}, \\ \eta_{\mathrm{top}} &= \frac{N_{\mathrm{top}}}{N_{\mathrm{get}}}, \\ \eta_{\mathrm{cap,total}} &= \frac{N_{\mathrm{cap}}}{N_{\mathrm{get}}}, \\ \eta_{\mathrm{cap,top}} &= \frac{N_{\mathrm{cap}}}{N_{\mathrm{top}}}, \end{aligned} \tag{3.17}$$

with appropriate safeguards against division by zero.
To quantify the quality of the captured-mode state $\rho_v(T)$, fidelities with respect to cat-qubit target families were evaluated by maximizing Equation (3.18),

$$\mathcal{F}(\boldsymbol{\theta}) = \langle \psi(\boldsymbol{\theta}) | \, \rho_v(T) \, | \psi(\boldsymbol{\theta}) \rangle \,, \tag{3.18}$$

over the parameters $\boldsymbol{\theta}$ specifying a chosen target-state ansatz. Two target families were considered.
First, an even/odd cat-qubit target family was considered. The ansatz state was defined as Equation (2.9), with the coherent amplitude expressed in polar form as in Equation (2.4). The fidelity maximization over this family was carried out with respect to the amplitude parameters (r, ϕ_α) and the Bloch-sphere angles (θ, φ) specifying the superposition within the $\{|C_+\rangle \,, |C_-\rangle\}$ basis. The resulting maximized fidelity was denoted by $\mathcal{F}_{\mathrm{eo}}$.
Second, an extended four-component cat ansatz was considered. The target state was defined as Equation (3.19),

$$
\begin{aligned}
|\psi_{\text{extended}}(\alpha, u_1, u_2, u_3, \vartheta, \vartheta')\rangle = \mathcal{N}\Big[& x(|\alpha\rangle + |-\alpha\rangle) \\
& + y e^{i\vartheta}(|\alpha\rangle - |-\alpha\rangle) \\
& + x'(|\alpha\rangle + i\,|-\alpha\rangle) \\
& + y' e^{i\vartheta'}(|\alpha\rangle - i\,|-\alpha\rangle)\Big],
\end{aligned}
\tag{3.19}
$$

where α was defined according to Equation (2.4) and $\mathcal{N}$ was a normalization constant. The nonnegative weights (x, y, x', y') satisfied $x^2 + y^2 + x'^2 + y'^2 = 1$ and were parametrized by angles $u_1, u_2, u_3 \in [0, \pi/2]$ according to Equation (3.20),

$$
\begin{aligned}
x &= \cos u_1, \\
y &= \sin u_1 \cos u_2, \\
x' &= \sin u_1 \sin u_2 \cos u_3, \\
y' &= \sin u_1 \sin u_2 \sin u_3.
\end{aligned}
\tag{3.20}
$$

For this extended ansatz, the fidelity maximization was performed over the parameter set $(r, \phi_\alpha, u_1, u_2, u_3, \vartheta, \vartheta')$, and the resulting maximized fidelity was denoted by $\mathcal{F}_{\text{extended}}$.

The maximization of Equation (3.18) was recast as a minimization problem by optimizing the negative fidelity. In both cases, this optimization was carried out numerically using a two-stage strategy. First, a global search was performed with SciPy's `differential_evolution` algorithm in order to reduce sensitivity to initial conditions and lower the risk of convergence to suboptimal local minima in the high-dimensional parameter space of the cat-state ansatz. Second, the best parameter vector returned by the global stage was used to initialize a local constrained refinement with SciPy's `minimize` under bound constraints.

This combination provided a practical balance between robustness and efficiency: the differential-evolution stage enabled reliable exploration of the parameter space, while the subsequent local refinement improved convergence in the vicinity of the optimum and typically produced a more accurate estimate of the maximum fidelity together with more precise best-fit parameters.

4

Results

This chapter presents the main results of the thesis. It begins with the Kerr-confinement model, where the formation of intracavity cat states, optimization of pulse-shape parameters, properties of the captured traveling mode, and the effects of pulse-time and Kerr-strength scaling are investigated. The analysis then extends to the two-photon dissipative-confinement model in order to compare Hamiltonian and dissipative mechanisms for generating propagating cat-qubit states. Finally, the robustness of both approaches is examined in the presence of dephasing and one-photon loss, with emphasis of how these noise mechanisms affect fidelity, mode selectivity, and purity of the captured mode.

4.1 Kerr (Hamiltonian) Confinement

This section reports results for the Kerr-nonlinear parametric oscillator, where confinement in phase space arises from the Kerr term in the Hamiltonian combined with a two-photon pump.

4.1.1 Intracavity cat formation

The intracavity dynamics of the KPO were examined in simulations where the virtual cavity and the mode-extraction procedure were omitted. In this setting, the master equation was solved for the reduced intracavity state $\rho_{\mathrm{KPO}}(t)$ under the same pump pulse $p(t)$ and STA protocol as in the full simulation pipeline, but without performing temporal-mode decomposition or virtual-mode capture. This isolated the intrinsic intracavity dynamics and provided a direct phase-space picture of how the intracavity state evolved during the protocol. The purpose of this analysis was to assess how closely the KPO follows the intended even-cat reference during the evolution, independently of the later emission and capture stages.
The instantaneous adiabatic reference amplitude was defined as, $\alpha_{\mathrm{ad}}(t) = \sqrt{p(t)/K}$, and the state $\rho(t)$ was compared to the corresponding ideal even cat state $|C_+(\alpha_{\mathrm{ad}}(t))\rangle$ via the fidelity presented in Equation (4.1),

$$\mathcal{F}_{\mathrm{cat},\alpha_{\mathrm{ad}}}(t) = \langle C_+(\alpha_{\mathrm{ad}}(t))|\, \rho(t)\, |C_+(\alpha_{\mathrm{ad}}(t))\rangle\,. \tag{4.1}$$

For the three representative pump amplitudes $A = \{2.5058, 3.4699, 4.4798\}$, corresponding to $N_{\mathrm{out}} = 2, 3, 4$ (STA enabled, $\varepsilon_x = 0$), the intracavity cat fidelity exhibited a characteristic transient reduction during the early stage of the protocol, followed by a recovery to near unity at later times. As summarized in Table 4.1,

the depth of the transient fidelity reduction increased systematically with pump amplitude. The minimum fidelity decreased from $\mathcal{F}^{\min}_{\mathrm{cat},\alpha_{\mathrm{ad}}} = 0.66797$ for $N_{\mathrm{out}} = 2$ to $\mathcal{F}^{\min}_{\mathrm{cat},\alpha_{\mathrm{ad}}} = 0.53404$ for $N_{\mathrm{out}} = 4$, while the corresponding recovery time shifted slightly later. In all three cases, however, the fidelity recovered and remained close to unity at late times, with recovery times $t_{\mathrm{rec}}K_{\mathrm{th}} \in [43.37, 46.74]$ and final values $\mathcal{F}_{\mathrm{cat},\alpha_{\mathrm{ad}}}(T) \geq 0.999992$.

A, (N_{out})	$\mathcal{F}^{\min}_{\mathrm{cat},\alpha_{\mathrm{ad}}}$	$t_{\min}K_{\mathrm{th}}$	$t_{\mathrm{rec}}K_{\mathrm{th}}$	$\mathcal{F}_{\mathrm{cat},\alpha_{\mathrm{ad}}}(T)$
2.5058, (2)	0.66797	8.55	43.37	0.999996
3.4699, (3)	0.57743	8.27	45.34	0.999994
4.4798 (4)	0.53404	7.43	46.74	0.999992

Table 4.1: Intracavity cat-formation fidelity metrics extracted from KPO-only simulations (STA enabled) for three operating points corresponding to target captured photon numbers $N_{\mathrm{out}} \in \{2, 3, 4\}$. For each pump amplitude A, the minimum fidelity $\mathcal{F}^{\min}_{\mathrm{cat},\alpha_{\mathrm{ad}}} = \min_t \mathcal{F}_{\mathrm{cat},\alpha_{\mathrm{ad}}}(t)$ is reported together with the time $t_{\min}K_{\mathrm{th}}$ at which it occurs, and the recovery time $t_{\mathrm{rec}}K_{\mathrm{th}}$ defined as the first time after the minimum where $\mathcal{F}_{\mathrm{cat},\alpha_{\mathrm{ad}}}(t) \geq 0.999$. The final-time fidelity $\mathcal{F}_{\mathrm{cat},\alpha_{\mathrm{ad}}}(T)$ quantifies how closely the intracavity state matches the instantaneous adiabatic cat reference at the end of the protocol.

Photon-number diagnostics are summarized in Table 4.2. The maximum intracavity population increased monotonically with the two-photon pump amplitude A, while the final residual population remained on the order of 10^{-5} in all investigated cases. The integrated occupation I_t likewise increased with A, reflecting the larger transient intracavity population associated with stronger pumping. At the same time, the root-mean-square deviation (RMSE) with respect to the instantaneous adiabatic prediction $|\alpha_{\mathrm{ad}}(t)|^2$ decreased modestly over the investigated range, indicating that the photon-number evolution remained in good overall agreement with the adiabatic expectation.

A, (N_{out})	$\max_t\langle a^\dagger a\rangle(t)$	$\langle a^\dagger a\rangle(T)$	$I_t = \int_0^T \langle a^\dagger a\rangle(t)\,dt$	$\mathrm{RMSE}\big(\langle a^\dagger a\rangle, \lvert\alpha_{\mathrm{ad}}\rvert^2\big)$
2.5058, (2)	0.99724	5×10^{-6}	10.119	0.05968
3.4699, (3)	1.43072	7×10^{-6}	15.120	0.05177
4.4798, (4)	1.91428	9×10^{-6}	20.116	0.04678

Table 4.2: Intracavity photon-number and adiabatic-tracking diagnostics from KPO-only simulations (STA enabled) for the same operating points as in Table 4.1. The maximum intracavity population over time is denoted as $\max_t\langle a^\dagger a\rangle(t)$ and the final residual population is denoted as $\langle a^\dagger a\rangle(T)$. The integrated population I_t summarizes the total intracavity occupation over the protocol. The RMSE quantifies the deviation between the simulated photon number $\langle a^\dagger a\rangle(t)$ and the instantaneous adiabatic reference $|\alpha_{\mathrm{ad}}(t)|^2$.

Figure 4.1 shows the time-resolved intracavity cat fidelity and representative Wigner snapshots for the case $\varepsilon_x = 0$ (no one-photon drive), with STA enabled and the two-photon pump amplitude fixed to $A = 2.505759$, corresponding to the operating point

optimized to yield $N_{\text{out}} = 2$. The fidelity trace illustrates the same characteristic behavior seen in Table 4.1, an initial decrease relative to the instantaneous even-cat reference followed by a later recovery to near-unity values. The corresponding Wigner snapshots show that the intracavity state evolves from a distribution localized near the origin toward a more clearly two-lobed phase-space structure as the protocol progresses. In the intermediate snapshots, for example around $tK_{\text{th}} = 6$ and 12, two lobes begin to emerge, indicating the development of cat-like structure in the intracavity field. However, the displayed Wigner plots do not show strongly pronounced interference fringes of the type typically associated with an ideal, fully developed Schrödinger cat state. Instead, the intracavity field appears as a coherent-state-like or two-lobed distribution at the sampled times. The transient reduction in intracavity fidelity therefore suggests that, during the intermediate stage of the protocol, the KPO field is not yet well described as an independent stationary cat state. As discussed further in connection with Figure 4.2, this behavior is naturally interpreted by considering the simultaneous build-up of correlations between the intracavity field and the emitted output field during the release process.

To further illustrate the time-domain dynamics of the protocol, Figure 4.2 shows representative trajectories for the case $N_{\text{out}} = 2$. The pump envelope $p(t)$ and the STA auxiliary term $p'(t)$ are shown together with the instantaneous photon numbers in the KPO and virtual mode, as well as the corresponding reduced-state purities. The KPO population, n_{KPO}, rises as the pump is increased and then decays as the excitation is emitted into the output channel, while the virtual-mode population, n_v, builds up correspondingly. This provides a natural interpretation of the reduced intracavity fidelity seen in Figure 4.1, particularly around $tK_{\text{th}} \approx 8$, at that point, the intracavity field is not fully independent, but is expected to be entangled with the emitted output field. The reduced intracavity state therefore need not to be an ideal pure cat state, because part of the coherence is shared with the emitted field during the release process. However, the fact that the reduced-state purities remain close to unity throughout most of the protocol indicates that the dynamics are still predominantly coherent, and that the observed deviations are not due to strong mixed-state degradation.

Taken together, these results show that the transient reduction in $\mathcal{F}_{\text{cat},\alpha_{\text{ad}}}(t)$ does not correspond to a complete failure of intracavity state preparation, but rather to a temporary deviation from the instantaneous even-cat reference during the build-up and release of the state. The recovery to near-unity fidelity in all investigated cases indicates that, according to this quantitative metric, the STA-assisted pump protocol keeps the KPO dynamics close to the desired even-cat manifold by late times. At the same time, the representative Wigner snapshots for $N_{\text{out}} = 2$ do not display the strongly pronounced interference fringes expected for an ideal stationary cat state, and therefore do not by themselves provide direct visual evidence of a fully developed intracavity textbook cat at the sampled times.

A natural interpretation of this apparent mismatch is that, in the present protocol, the most relevant cat-state structure is not most clearly expressed as a stationary intracavity state at each intermediate time, but rather as a propagating temporal-mode state that is formed during the combined generation-and-release process. Since the KPO is continuously coupled to the transmission line, the protocol does not first

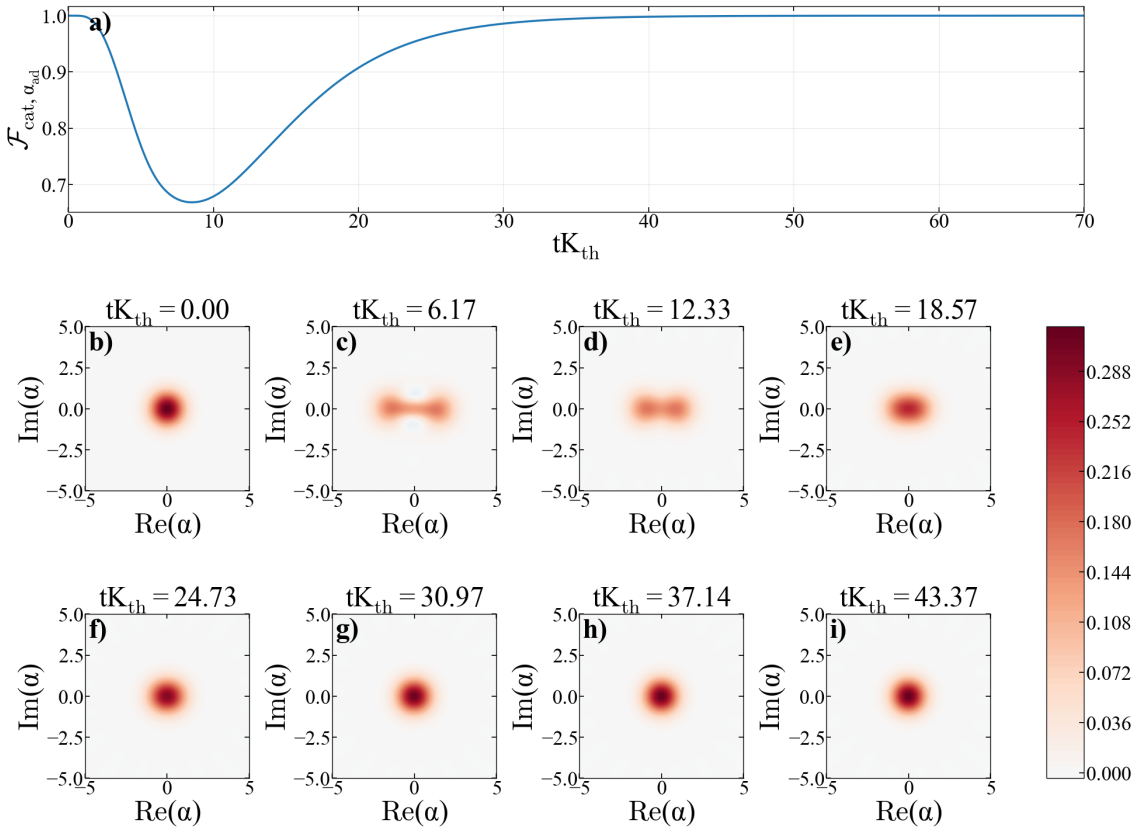

Figure 4.1: Intracavity cat formation for the Kerr (Hamiltonian-confinement) model. Top panel: time-resolved fidelity $\mathcal{F}_{\mathrm{cat},\alpha_{\mathrm{ad}}}(tK_{\mathrm{th}})$, where the instantaneous adiabatic amplitude is defined as $\alpha_{\mathrm{ad}}(t) = \sqrt{p(t)/K}$ (real-valued in the chosen convention). Bottom panel: Wigner-function snapshots $W(\alpha, t)$ of $\rho_{\mathrm{KPO}}(t)$ at selected times (indicated above each snapshot), plotted versus the complex phase-space coordinate $\alpha = \mathrm{Re}(\alpha) + i\,\mathrm{Im}(\alpha)$. The one-photon drive was disabled ($\varepsilon_x = 0$), STA was enabled and the pump amplitude was fixed to $A = 2.505759$, optimized to yield two photons in the output field. The eight Wigner snapshots were chosen automatically by sampling uniformly from $t = 0$ up to the first time at which the fidelity returned to within 10^{-3} of unity after an initial drop.

prepare an ideal intracavity cat state and then release it in a separate step. Instead, state generation and emission occur simultaneously. The intracavity Wigner snapshots therefore represent only the instantaneous residual field remaining in the KPO, which can appear as coherent-state-like lobes or transient blobs without strongly pronounced interference fringes, even while coherent cat-state structure is being formed in the emitted wave packet.

A further indication of this is that the transient dip in $\mathcal{F}_{\mathrm{cat},\alpha_{\mathrm{ad}}}(t)$ follows the minima of the reduced-state purities $\mathrm{Tr}\{\rho_{\mathrm{KPO}}(t)^2\}$ and $\mathrm{Tr}\{\rho_v(t)^2\}$, and occurs near the maximum of the two-photon pump pulse. This suggests that the largest deviation from the ideal intracavity cat reference arises precisely when the protocol is most strongly driving the combined generation-and-release dynamics, so that the intracavity state is least well described as an isolated pure cat state.

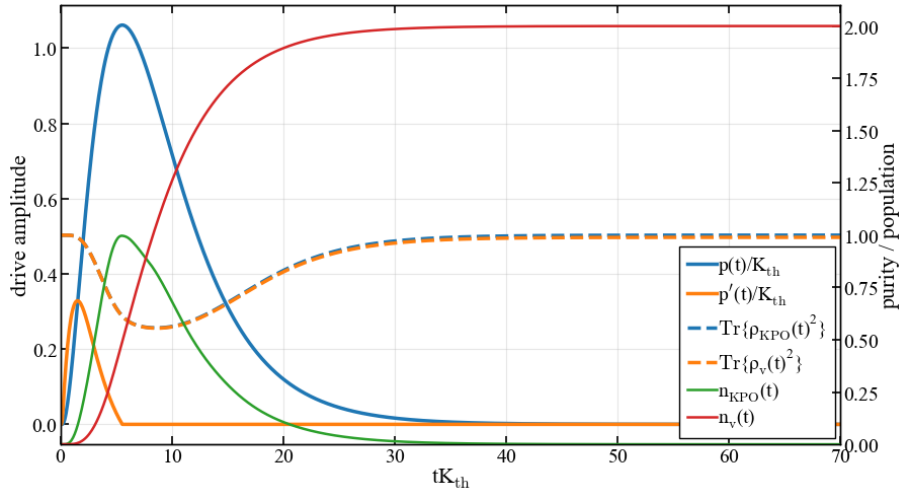

Figure 4.2: Full time-domain dynamics for a representative Kerr Hamiltonian-confinement run with $N_{\text{out}} = 2$, STA enabled, LPF orders $(n_p, n_\varepsilon) = (3, 2)$, and $\varepsilon_x = 0$. Left axis: pump envelope $p(t)/K_{\text{th}}$ and the STA auxiliary term $p'(t)/K_{\text{th}}$. Right axis: instantaneous purities of the reduced states, $\text{Tr}\{\rho_{\text{KPO}}(t)^2\}$ and $\text{Tr}\{\rho_v(t)^2\}$, together with the mean photon numbers $n_{\text{KPO}}(t) = \langle a^\dagger a\rangle(t)$ and $n_v(t) = \langle a_v^\dagger a_v\rangle(t)$.

4.1.2 LPF Order optimization

The two-photon pump $p(t)$ and one-photon rotation pulse $\varepsilon(t)$ were parameterized using low-pass-filter (LPF) pulse families of orders (n_p, n_ε). These orders controlled the smoothness and effective bandwidth of the applied envelopes and therefore influenced both the temporal-mode selectivity of the emission and the achievable state fidelity after capture. The purpose of this analysis was to identify LPF order pairs that yielded a high and stable performance across the full logical-rotation interval, rather than only at isolated operating points.

A discrete search over LPF order pairs (n_p, n_ε) was performed for each target photon number $N_{\text{out}} \in \{2, 3, 4, 5\}$. A full logical rotation from the even-cat branch toward the odd-cat branch was realized within the interval $\varepsilon_x \in [0, 0.1]$, therfore each candidate pair was evaluated over this full window. For each (n_p, n_ε) and N_{out}, the even/odd cat-qubit fidelity $\mathcal{F}_{\text{eo}}(\varepsilon_x)$ was summarized by its mean value $\overline{\mathcal{F}}_{\text{eo}}$ over $\varepsilon_x \in [0, 0.1]$. To assess robustness over the full rotation path, the minimum fidelity $\mathcal{F}_{\text{eo}}^{\text{min}} = \min_{\varepsilon_x \in [0,0.1]} \mathcal{F}_{\text{eo}}$ and the standard deviation $\sigma(\mathcal{F}_{\text{eo}})$ were used as secondary criteria.

The investigated LPF order pairs were $(n_p, n_\varepsilon) \in \{(3, 2), (3, 3), (4, 2), (4, 3), (4, 4), (4, 5)\}$, and each case was simulated both with and without STA enabled. Figure 4.3 summarizes the performance trends for the Kerr (Hamiltonian-confinement) model at $N_{\text{out}} \in \{2, 3, 4, 5\}$ with STA enabled. For a fuller comparison of the LPF-order scans, including the cases with and without STA across all investigated target photon numbers, see Appendix A.1.

Across all investigated targets $N_{\text{out}} \in \{2, 3, 4, 5\}$ with STA enabled, the pair $(n_p, n_\varepsilon) = (3, 2)$ provided the best overall performance. In each case, this order pair yielded the highest mean fidelity over the full rotation window while also maintaining a high

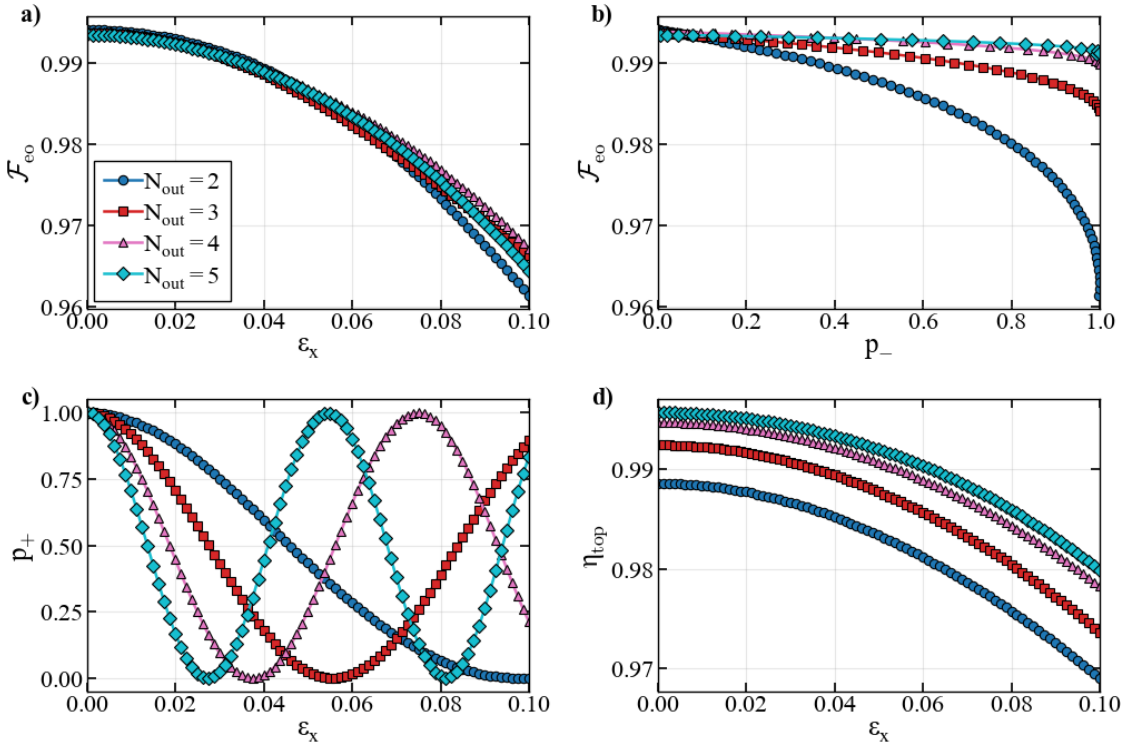

Figure 4.3: LPF-order optimization and performance trends for the Kerr (Hamiltonian-confinement) model. For each target output photon number $N_{\text{out}} \in \{2, 3, 4, 5\}$, the pair of LPF orders (n_p, n_ε) is selected by maximizing the mean even/odd cat-qubit fidelity $\overline{\mathcal{F}}_{\text{eo}}$ over the scanned parameter set. In all cases STA is enabled. The selected LPF orders are $(n_p, n_\varepsilon) = (3, 2)$ for $N_{\text{out}} = 2, 3, 4, 5$. The figure includes (a) even/odd cat-qubit fidelity $\mathcal{F}_{\text{eo}}$ versus one-photon drive strength ε_x, (b) $\mathcal{F}_{\text{eo}}$ versus fitted odd weight p_-, (c) fitted even weight p_+ versus ε_x, and (d) top-mode efficiency η_{top} versus ε_x.

worst-case fidelity and a low standard deviation. The corresponding mean fidelities are presented in Equation (4.2)

$$\overline{\mathcal{F}}_{\text{eo}} = \begin{cases} 0.983143, & N_{\text{out}} = 2, \\ 0.983578, & N_{\text{out}} = 3, \\ 0.984620, & N_{\text{out}} = 4, \\ 0.983752, & N_{\text{out}} = 5, \end{cases} \tag{4.2}$$

with corresponding worst-case values presented in Equation (4.3)

$$\mathcal{F}_{\text{eo}}^{\min} = \begin{cases} 0.961363, & N_{\text{out}} = 2, \\ 0.966250, & N_{\text{out}} = 3, \\ 0.967130, & N_{\text{out}} = 4, \\ 0.964387, & N_{\text{out}} = 5. \end{cases} \tag{4.3}$$

The associated standard deviations remained below 1.1×10^{-2} in all cases. These

results show that the performance is not only high on average, but also comparatively uniform across the scanned logical-rotation interval.
In addition to state fidelity, the dominant temporal-mode fraction remained high throughout the sweep. Its mean values are presented in Equation (4.4)

$$\overline{\eta}_{\mathrm{top}} = \begin{cases} 0.9817, & N_{\mathrm{out}} = 2, \\ 0.9860, & N_{\mathrm{out}} = 3, \\ 0.9891, & N_{\mathrm{out}} = 4, \\ 0.9904, & N_{\mathrm{out}} = 5, \end{cases} \tag{4.4}$$

showing a slight increase with target photon number over the investigated range. The capture efficiency of the dominant temporal mode, $\eta_{\mathrm{cap,top}}$, remained essentially unity across the sweeps, with mean values presented in Equation (4.5)

$$\overline{\eta}_{\mathrm{cap,top}} = \begin{cases} 0.99969, & N_{\mathrm{out}} = 2, \\ 0.99965, & N_{\mathrm{out}} = 3, \\ 0.99963, & N_{\mathrm{out}} = 4, \\ 0.99961, & N_{\mathrm{out}} = 5. \end{cases} \tag{4.5}$$

This indicates that, once the dominant mode is identified, the virtual-cavity capture itself remains essentially lossless over the full parameter sweep.
Taken together, these results indicate that relatively low-order LPF pulse families are sufficient to achieve high-fidelity cat-qubit control in the present protocol. In particular, the fact that $(n_p, n_\varepsilon) = (3, 2)$ is optimal for all investigated values of N_{out} suggests that increasing the LPF order does not automatically improve performance. Rather, the results suggest that lower-order LPF pulse families may be advantageous, possibly because higher LPF orders produce more temporally extended pulses, which can make the state-generation and emission process less compact and allow small deviations from the intended evolution to build up over time. The combination of high fidelity, low variation, high top-mode selectivity, and near-unity dominant-mode capture further suggests that the main limitation is not the capture stage itself, but the quality of the emitted state and its control during the rotation process. Since the same LPF order pair performed well across all considered target photon numbers, $(n_p, n_\varepsilon) = (3, 2)$ is adopted as the baseline choice in the remainder of this chapter unless stated otherwise.
Figure 4.4 compares the baseline Kerr-model protocol without STA to the corresponding protocol with the STA correction included (see Equation (2.27)). The inclusion of STA led to a clear improvement in performance for all investigated values of N_{out}. In particular, both the branch-averaged fidelity and the top-mode efficiency increased substantially relative to the no-STA case, and the improvement became more pronounced as N_{out} increased. The virtual-mode purity also remained higher with STA enabled over the relevant branch of the sweep. This shows that non-adiabatic effects remain an important source of error in the baseline protocol, especially at larger target photon numbers, and that the STA correction plays a central role in maintaining both state quality and mode purity during the emission-and-capture process. A quantitative summary of the comparison between protocols with and without STA is given in Appendix A.2.

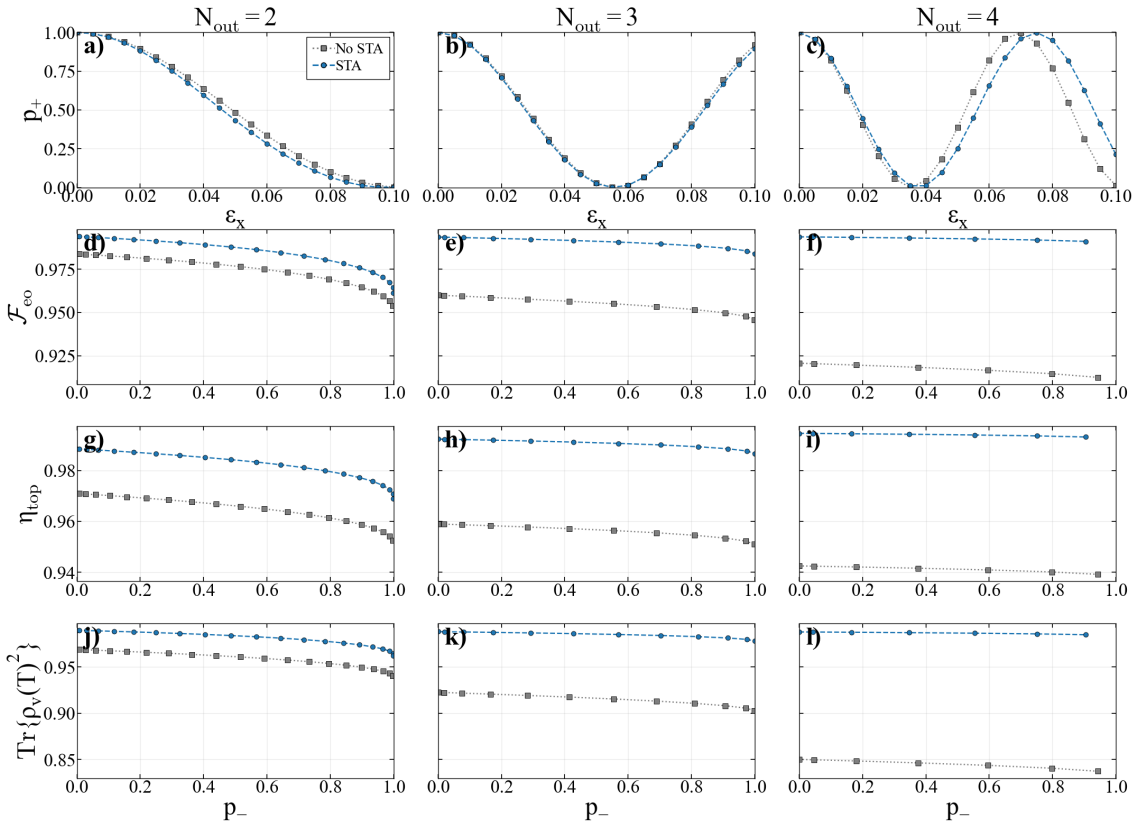

Figure 4.4: Comparison of STA disabled and enabled for the Kerr (Hamiltonian-confinement) model using the baseline LPF orders $(n_p, n_\varepsilon) = (3, 2)$. Columns correspond to target output photon numbers $N_{\text{out}} = 2, 3, 4$, and rows show (top to bottom): fitted even weight p_+ versus normalized one-photon-drive amplitude ε_x, even/odd cat-qubit fidelity $\mathcal{F}_{\text{eo}}$ versus fitted odd weight p_-, top-mode efficiency η_{top} versus p_-, and virtual-mode purity $\text{Tr}\{\rho_v(T)^2\}$ versus p_-. The two curve sets correspond to no STA and with STA enabled. For the rows plotted against p_-, the curves are truncated at an N_{out}- and variant-dependent cutoff in ε_x, chosen to retain approximately one effective rotation branch.

The final virtual-mode states were also benchmarked against the extended target family introduced in Subsection 3.3.6. However, no noticeable increase in fidelity was obtained compared with the even/odd target family. This indicates that the reported fidelities are not significantly limited by a mismatch between the simulated states and the restricted even/odd target ansatz, and therefore supports the use of the simpler target family as the primary benchmark in the following analysis.

4.1.3 Wigner functions of the captured states

To visualize how the captured virtual-mode state evolves as the effective logical X-rotation is increased, Wigner functions of $\rho_{v_1}(T)$ were plotted for representative points along the ε_x sweep. The purpose of this analysis was to provide a qualitative phase-space picture of how the captured state changes as the one-photon drive moves the system along the logical rotation path. In this subsection, the Wigner representation serves primarily as a visual complement to the quantitative cat-qubit fit parameters and fidelity measures introduced earlier.

For each N_{out}, eight representative points were selected such that the fitted odd weight p_- approximately spans the interval $[0, 1]$ in near-uniform steps. This choice makes the progression from an even-like cat state ($p_- \approx 0$), through intermediate superposition states ($p_- \approx 0.5$), toward an odd-like cat state ($p_- \approx 1$) directly visible in phase space. Figures 4.5, 4.6, 4.7, and 4.8 show the resulting phase-space distributions for $N_{\text{out}} = 2, 3, 4, 5$, with STA enabled and the optimized LPF orders. The Wigner functions are plotted versus the complex phase-space coordinate $\alpha = \mathrm{Re}(\alpha) + i\,\mathrm{Im}(\alpha)$.

To enable consistent visual comparison across the sweep, each state was rotated in phase space according to $\rho \mapsto R(\theta_\alpha)\rho R^\dagger(\theta_\alpha)$ with $R(\theta_\alpha) = e^{-i\theta_\alpha \hat{n}}$, where θ_α is the fitted coherent-state phase from the cat-qubit fit. This rotation aligns the cat axis with the $\mathrm{Re}(\alpha)$ axis and makes the change in phase-space structure across the sweep easier to compare from panel to panel.

The Wigner plots show a systematic evolution of the captured state across the ε_x sweep for all investigated values of N_{out}. At small fitted odd weight $p_- \approx 0$, the phase-space distributions are most similar to even-like cat configurations, while at large fitted odd weight $p_- \approx 1$ they approach odd-like structure. For intermediate values, especially around $p_- \approx 0.5$, the Wigner functions display states that interpolate between these two limiting cases. After phase alignment, the dominant phase-space lobes remain oriented along a common axis for all four values $N_{\text{out}} = 2, 3, 4, 5$, making the progression along the logical-rotation path visually apparent. Across the sweep, the overall cat-like structure remains recognizable.

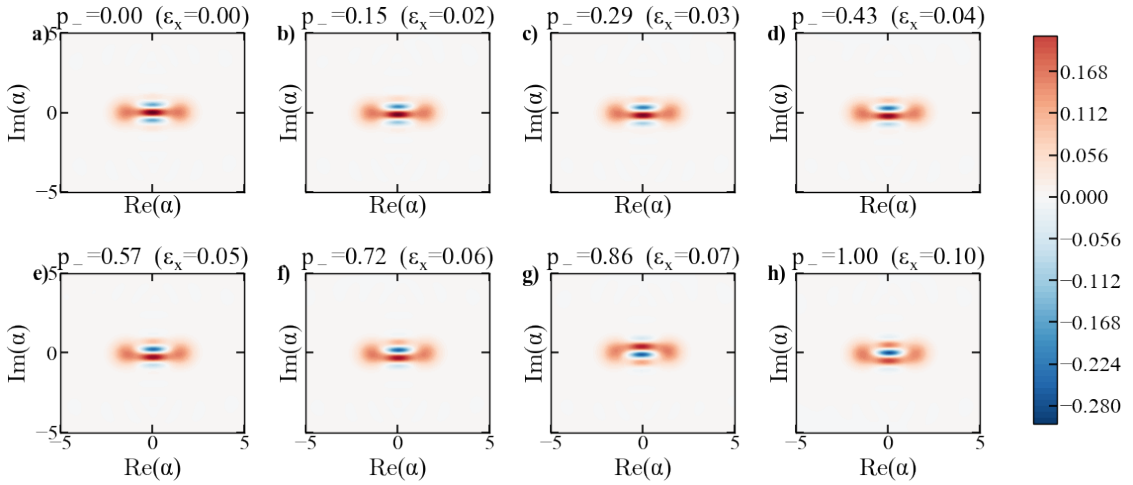

Figure 4.5: Wigner functions of the captured virtual-mode state $\rho_{v_1}(T)$ for $N_{\text{out}} = 2$ using the optimized LPF orders $(n_p, n_\varepsilon) = (3, 2)$ and the Kerr (Hamiltonian-confinement) model with STA enabled. The eight panels are selected along the ε_x sweep by matching approximately uniform values of the fitted odd weight p_-, from $p_- \approx 0.0$ to $p_- \approx 1.0$. The labels above each panel show the fitted p_- and the corresponding ε_x. Each state is phase-rotated before plotting so that the cat axis is aligned with the Re(α)-axis.

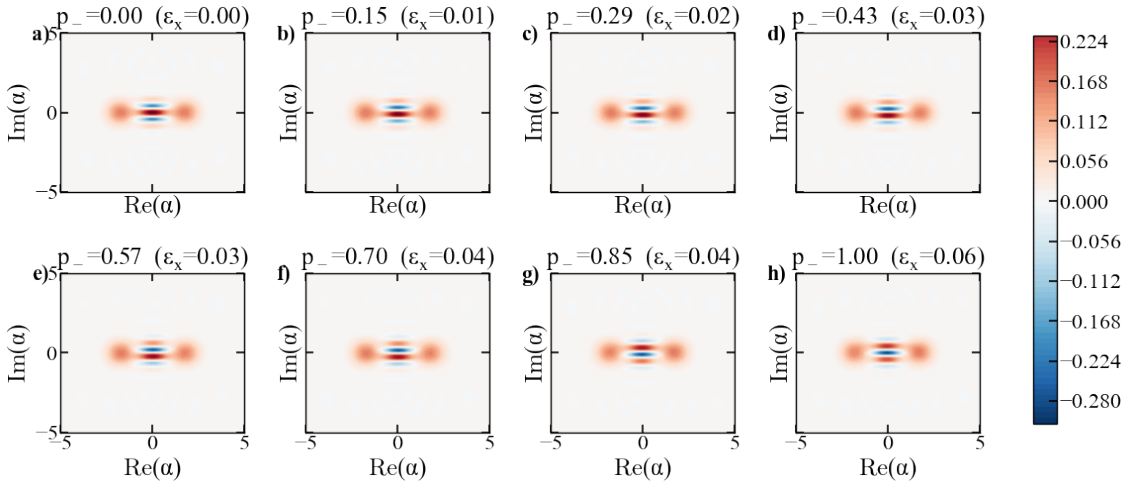

Figure 4.6: Wigner functions of the captured virtual-mode state $\rho_{v_1}(T)$ for $N_{\text{out}} = 3$ using the optimized LPF orders $(n_p, n_\varepsilon) = (3, 2)$ and the Kerr (Hamiltonian-confinement) model with STA enabled. The eight panels are selected along the ε_x sweep by matching approximately uniform values of the fitted odd weight p_-, from $p_- \approx 0.0$ to $p_- \approx 1.0$. The labels above each panel show the fitted p_- and the corresponding ε_x. Each state is phase-rotated before plotting so that the cat axis is aligned with the Re(α)-axis.

These phase-space results support the interpretation that the one-photon drive produces a continuous evolution of the captured state along the intended logical manifold, rather than generating only isolated endpoint states. The smooth visual change

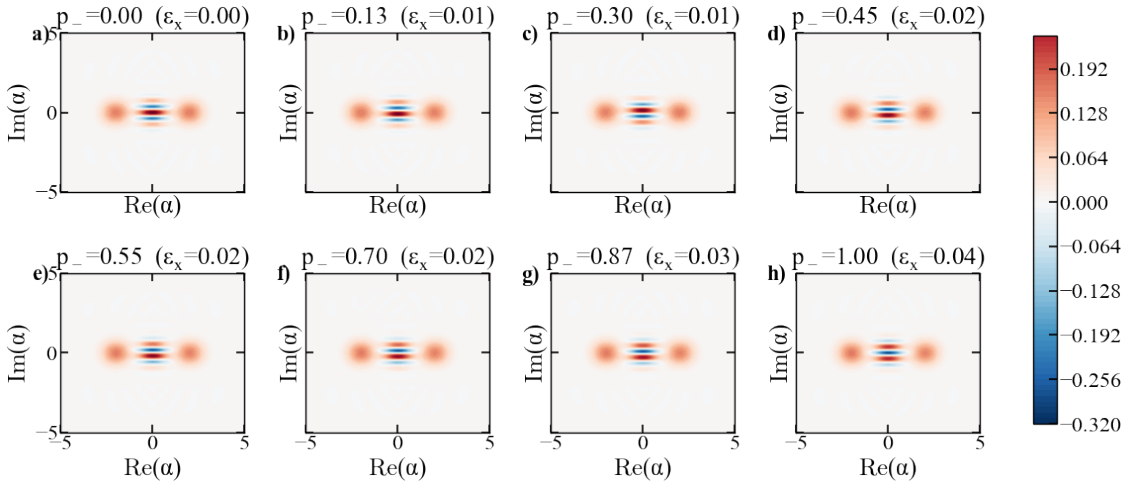

Figure 4.7: Wigner functions of the captured virtual-mode state $\rho_{v_1}(T)$ for $N_{\text{out}} = 4$ using the optimized LPF orders $(n_p, n_\varepsilon) = (3, 2)$ and the Kerr (Hamiltonian-confinement) model with STA enabled. The eight panels are selected along the ε_x sweep by matching approximately uniform values of the fitted odd weight p_-, from $p_- \approx 0.0$ to $p_- \approx 1.0$. The labels above each panel show the fitted p_- and the corresponding ε_x. Each state is phase-rotated before plotting so that the cat axis is aligned with the Re(α)-axis.

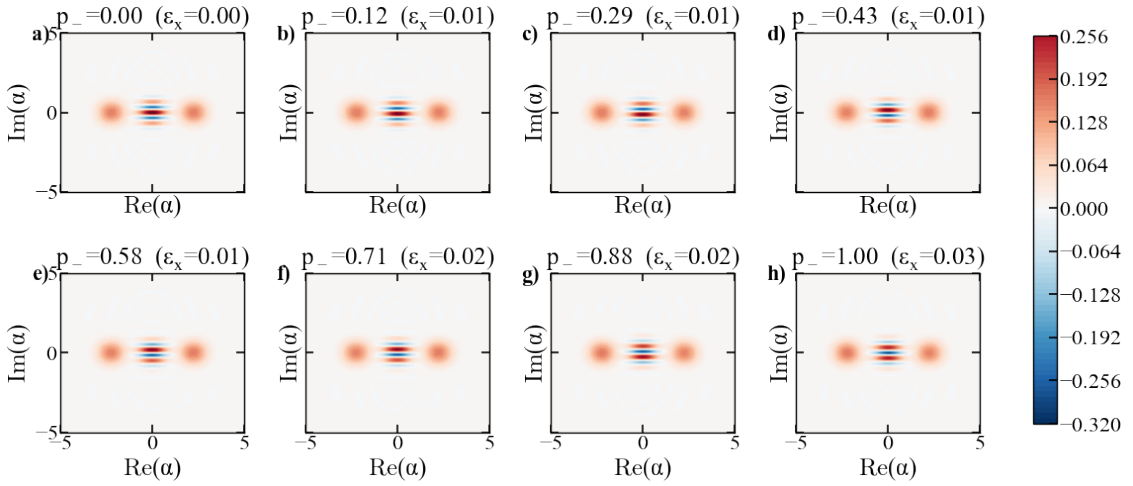

Figure 4.8: Wigner functions of the captured virtual-mode state $\rho_{v_1}(T)$ for $N_{\text{out}} = 5$ using the optimized LPF orders $(n_p, n_\varepsilon) = (3, 2)$ and the Kerr (Hamiltonian-confinement) model with STA enabled. The eight panels are selected along the ε_x sweep by matching approximately uniform values of the fitted odd weight p_-, from $p_- \approx 0.0$ to $p_- \approx 1.0$. The labels above each panel show the fitted p_- and the corresponding ε_x. Each state is phase-rotated before plotting so that the cat axis is aligned with the Re(α)-axis.

in the Wigner functions as p_- increases is consistent with the fitted cat-qubit description and indicates that the protocol accesses a continuous family of logical states between the even-like and odd-like limits. At the same time, the Wigner plots should

be interpreted with appropriate caution. They provide qualitative visual evidence of this evolution, but they do not by themselves determine how close each state is to an ideal cat-qubit target. Taken together, the Wigner functions therefore support the conclusion that the captured states follow the intended logical rotation in a qualitatively consistent way, while the quantitative fidelity and fitted-weight metrics remain the primary measures of performance.

4.1.4 Comparison of extracted and reference mode shapes

The virtual-cavity capture protocol is motivated by the expectation that the dominant emitted temporal mode $v_1(t)$ should be closely related to the reference mode associated with the pump-induced coherent amplitude $\alpha(t) = \sqrt{p(t)/K}$. As discussed in Section 2.6, this expectation is physically motivated by the idea that when state generation and release occur in the same process, the temporal profile of the drive helps determine the shape of the propagating wave packet. The purpose of the present analysis is therefore to test this expectation directly by comparing the dominant mode extracted from the correlation-kernel diagonalization with the reference profile $\alpha(t)$ and by quantifying their normalized overlap.
Figure 4.9 shows $|v_1(t)|$ and $|\alpha(t)|$ for $N_{\text{out}} = 2, 3, 4, 5$ with STA enabled and the optimized LPF orders, evaluated at representative points near $p_- = 0$, $p_- = 0.5$, and $p_- = 1$. In all displayed cases, the extracted dominant mode and the reference profile agree closely. The normalized magnitudes almost completely overlap across the full time window, both near the even-like limit, in the intermediate regime, and near the odd-like limit of the logical-rotation sweep. The minimum overlap achieved over the displayed points was $|\langle v_1|\alpha\rangle| = 0.991$, indicating consistently strong agreement between the extracted dominant temporal mode and the reference profile.
These results support the interpretation that the dominant emitted field is indeed concentrated in a temporal mode set primarily by the pump-shaped state-generation process inside the KPO. In this sense, the good agreement between $v_1(t)$ and $\alpha(t)$ is not merely a numerical convenience of the virtual-cavity method, but is consistent with the broader physical picture that the drive profile governs the shape of the emitted wave packet. The high overlaps therefore strengthen the view that $\alpha(t)$ provides a physically meaningful reference mode for the dominant output field. At the same time, the small residual mismatch between $v_1(t)$ and $\alpha(t)$ indicates that this identification is not exact in a strict sense, but it remains an accurate practical approximation for all cases shown here.

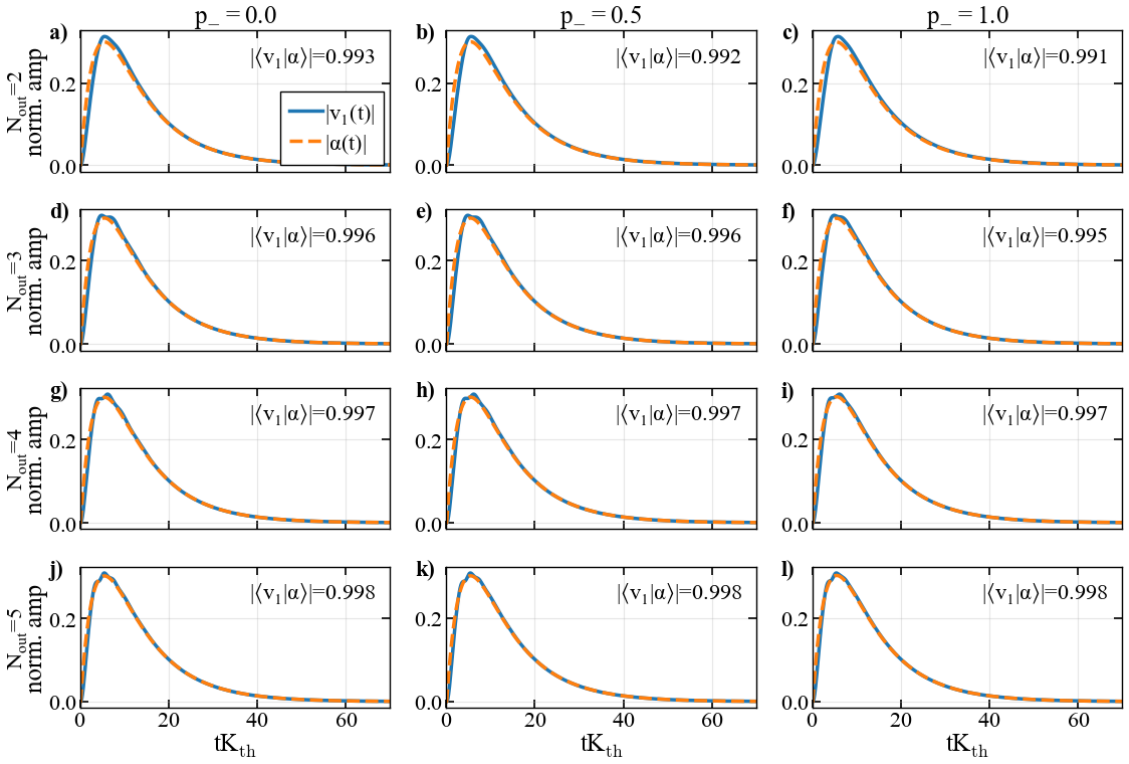

Figure 4.9: Comparison between the extracted dominant output mode $v_1(t)$ and the reference profile $\alpha(t) = \sqrt{p(t)/K}$ for the Kerr model. Both curves are L^2-normalized before plotting, and the reported overlap is $|\langle v_1|\alpha\rangle|$ after phase alignment. Rows correspond to $N_{\text{out}} = 2, 3, 4, 5$, and columns correspond to fitted odd weights $p_- = 0, 0.5, 1$ (selected as nearest available runs in the optimized LPF-order dataset where STA is enabled).

4.1.5 Time-scaling optimization of the one-photon drive pulse

Beyond the discrete LPF-order choice, the relative time scale of the one-photon drive pulse $\varepsilon(t)$ provides an additional continuous control parameter that can influence how efficiently a logical X-rotation is implemented before leakage and non-adiabatic effects degrade the captured state. The purpose of this analysis was to determine whether rescaling the temporal width of the one-photon drive pulse could improve the quality of the logical rotation, and to assess how sensitive the Kerr-model performance was to this additional control parameter.

The optimization results for $N_{\text{out}} \in \{2, 3, 4, 5\}$ with STA enabled and $(n_p, n_\varepsilon) = (3, 2)$ are summarized in Figure 4.10, where the curves are grouped by the one-photon-drive time-scaling factor $\lambda_\varepsilon \in \{0.7, 0.8, 0.9, 1.0, 1.1, 1.2, 1.3, 1.4, 1.5, 1.6, 1.7\}$. Figure 4.10 shows that the time-scaling factor λ_ε provides a meaningful additional degree of freedom beyond the discrete LPF-order choice. When the full scanned interval $\varepsilon_x \in [0, 0.10]$ was used as the comparison window, increasing λ_ε systematically improved the mean fidelity and reduced the variation of $\mathcal{F}_{\text{eo}}$ for $N_{\text{out}} = 2, 3, 4$ within the explored range. The same overall trend was also seen for $N_{\text{out}} = 5$, although the improvement there was somewhat smaller and the best-performing scanned value

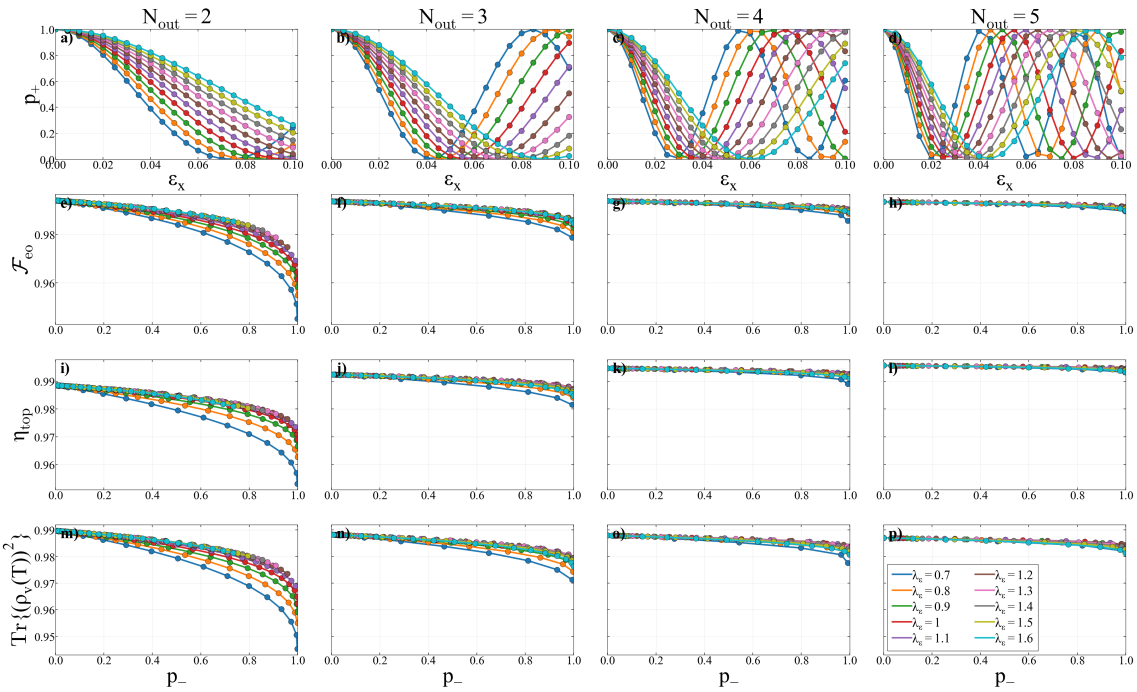

Figure 4.10: Optimization of the ε-pulse time-scaling factor λ_ε in the Kerr (Hamiltonian-confinement) model. STA is enabled, the LPF orders used are $(n_p, n_\varepsilon) = (3, 2)$ and the two-photon pump time-scaling factor λ_p is set to one. Columns show target output photon numbers $N_{\text{out}} = 2, 3, 4, 5$. Rows show (top to bottom): fitted even weight p_+ versus ε_x, even/odd cat-qubit fidelity $\mathcal{F}_{\text{eo}}$ versus odd weight p_-, top-mode efficiency η_{top} versus p_-, and virtual-mode purity $\text{Tr}\{\rho_v(T)^2\}$ versus p_-. Curves are grouped by the ε-pulse time-scaling λ_ε (color). For the rows plotted against p_-, the curves are truncated at a N_{out}- and λ_ε-dependent cutoff in ε_x (approximately corresponding to one effective rotation cycle) to ensure a consistent comparison.

shifted to $\lambda_\varepsilon = 1.4$ rather than 1.6.

Table 4.3 compares the baseline choice $\lambda_\varepsilon = 1.0$ with the value that maximized the mean fidelity over the full scanned ε_x interval. For $N_{\text{out}} = 2, 3, 4$, increasing the time scale to $\lambda_\varepsilon = 1.6$ improved both the mean fidelity and the worst-case fidelity, while for $N_{\text{out}} = 5$ the best scanned value was $\lambda_\varepsilon = 1.4$. The mean fidelity increased from 0.983143 to 0.991204 for $N_{\text{out}} = 2$, from 0.983578 to 0.989953 for $N_{\text{out}} = 3$, from 0.984620 to 0.988994 for $N_{\text{out}} = 4$, and from 0.983752 to 0.986565 for $N_{\text{out}} = 5$. The corresponding worst-case fidelity also improved in all cases. By contrast, the fidelity at the first balanced point $p_- = 0.5$ changed only weakly, remaining close to 0.99 in all cases and showing only marginal improvement or slight decrease depending on N_{out}.

These results indicate that the timing of the one-photon drive is an important additional control parameter for the Kerr-model protocol. In particular, the improvement in mean fidelity and worst-case fidelity with increasing λ_ε suggests that the temporal scaling of the one-photon drive affects how well the logical rotation is matched to the relevant dynamical time scales of the protocol, and thereby how ro-

N_{out}	λ_ε	$\overline{\mathcal{F}}_{\mathrm{eo}}$	$\mathcal{F}_{\mathrm{eo}}^{\mathrm{min}}$	$\mathcal{F}_{\mathrm{eo}}(p_- = 0.5)$	$\epsilon_x(p_- = 0.5)$
2	1.0	0.983143	0.961363	0.987714	0.045870
	1.6	0.991204	0.985398	0.989445	0.074299
3	1.0	0.983578	0.966249	0.991260	0.027544
	1.6	0.989953	0.982375	0.991606	0.044584
4	1.0	0.984620	0.967129	0.992805	0.018708
	1.6	0.988994	0.978550	0.992676	0.030304
5	1.0	0.983752	0.964387	0.992906	0.013659
	1.4	0.986565	0.970972	0.992827	0.019076

Table 4.3: Compact comparison between the baseline time scaling $\lambda_\varepsilon = 1.0$ used in the main Kerr-model studies and the best-performing λ_ε value within the scanned set, evaluated over the full sweep $\varepsilon_x \in [0, 0.10]$. The quantity $\mathcal{F}_{\mathrm{eo}}(p_- = 0.5)$ was evaluated at the first occurrence of $p_- = 0.5$ as ε_x increased, using linear interpolation between neighboring sampled points.

bustly the rotation can be implemented over the full sweep. At the same time, the weak dependence of $\mathcal{F}_{\mathrm{eo}}(p_- = 0.5)$ on λ_ε shows that optimizing the full trajectory is not equivalent to optimizing a single representative operating point. Since increasing λ_ε shortens the effective duration of the one-photon drive, the results further suggest that a faster rotation pulse may better match the relevant emission-and-capture time scale. In that case, the improved fidelity could reflect better timing of the logical rotation relative to the state-generation and release dynamics.
In the remainder of this chapter, $\lambda_\varepsilon = 1.0$ is retained as the baseline choice in order to maintain a consistent parameter set across the main Kerr-model studies. This choice should therefore be understood as a controlled reference setting rather than the globally optimal value according to the full-sweep fidelity criterion.

4.1.6 Effect of Kerr-Term Scaling in the Hamiltonian

To separate the role of the Kerr nonlinearity as a confinement mechanism from parameters defined relative to the fixed Kerr threshold scale, the Kerr term in the Hamiltonian was rescaled by a factor $K_{\mathrm{ham}}/K_{\mathrm{th}} \in \{1, 2, 3, 4, 5, 6, 7\}$, while quantities such as κ_{ex} were kept fixed in units of the reference scale K_{th}. The purpose of this analysis was to determine how the protocol performance changes when the intrinsic Kerr confinement strength is varied independently of the remaining threshold-scaled parameters.
Figure 4.11 shows how p_+, $\mathcal{F}_{\mathrm{eo}}$, η_{top}, and $\mathrm{Tr}\{\rho_v(T)^2\}$ depend on $K_{\mathrm{ham}}/K_{\mathrm{th}}$ for $N_{\mathrm{out}} \in \{2, 3, 4\}$ with STA enabled and $(n_p, n_\varepsilon) = (3, 2)$. For the panels plotted versus p_-, the curves are truncated to retain the first effective rotation branch of the even-to-odd interpolation, thereby enabling a consistent comparison across Kerr scalings.
The results show that increasing the Kerr-term scaling changes not only the fidelity metrics, but also the drive conditions required to reach a comparable logical operating point. In Table 4.4, the dimensionless rotation parameter $\varepsilon_x(p_- = 0.5)$ decreases systematically as $K_{\mathrm{ham}}/K_{\mathrm{th}}$ is increased. For example, for $N_{\mathrm{out}} = 3$, it is reduced from 0.027547 at $K_{\mathrm{ham}}/K_{\mathrm{th}} = 1$ to 0.003956 at $K_{\mathrm{ham}}/K_{\mathrm{th}} = 7$, while for $N_{\mathrm{out}} = 4$

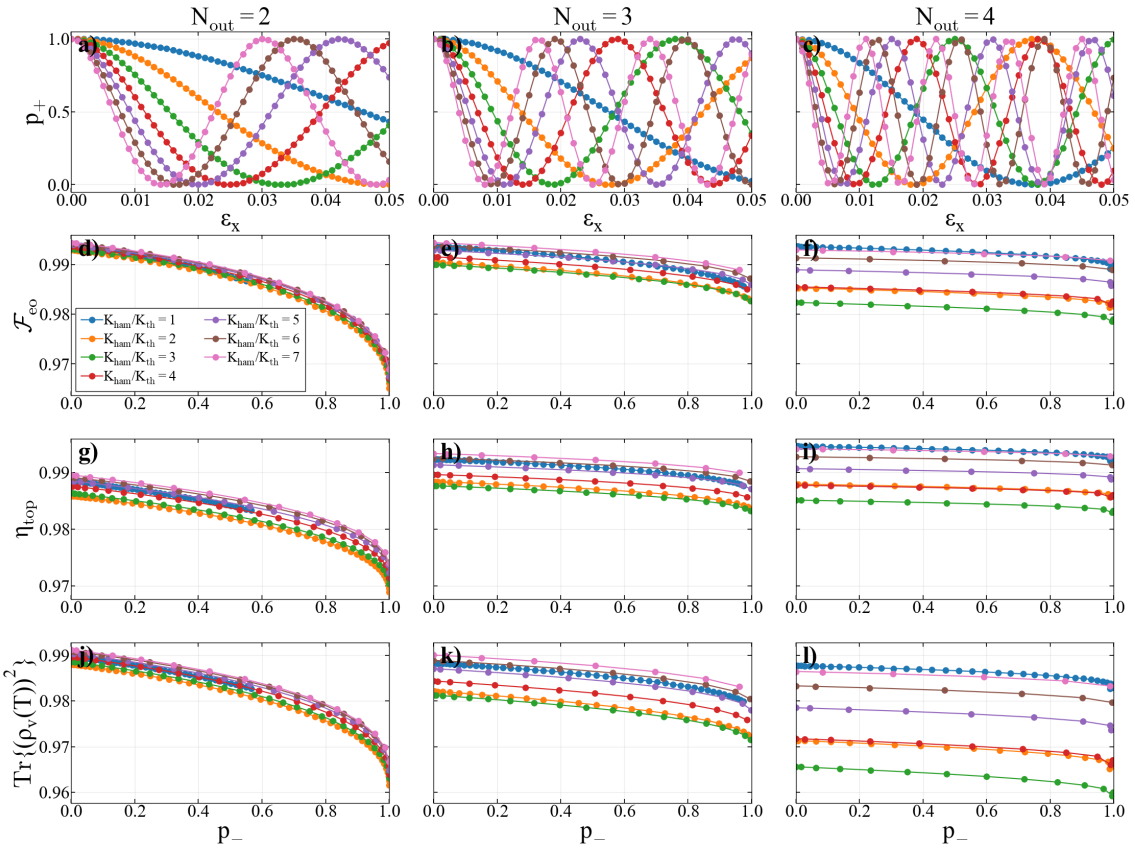

Figure 4.11: Effect of rescaling the Kerr nonlinearity in the Hamiltonian K_{ham} for the Kerr-confinement model, while keeping the Kerr threshold scale K_{th} unchanged. Here the Kerr term in the Hamiltonian is multiplied by $K_{\text{ham}}/K_{\text{th}} \in \{1, \ldots, 7\}$, and results are shown for $N_{\text{out}} = 2, 3, 4$ (columns), using STA and the optimized LPF orders $(n_p, n_\varepsilon) = (3, 2)$. Top row: fitted even weight p_+ versus ε_x. Second row: even/odd cat-qubit fidelity $\mathcal{F}_{\text{eo}}$ versus fitted odd weight p_-. Third row: top-mode efficiency η_{top} versus p_-. Bottom row: purity of the captured virtual-mode state, $\text{Tr}\{\rho_v(T)^2\}$, versus p_-. For the rows plotted against p_-, the curves are truncated at an N_{out}- and K_{ham}-dependent cutoff in ε_x (approximately corresponding to one effective rotation cycle) to ensure a consistent comparison across Kerr scalings.

it drops from 0.018717 to 0.002680. However, since ε_x was defined through the L^2-norm relation in Equation (3.12), this decrease should be interpreted as a reduction in the required one-photon drive strength relative to the pump pulse, rather than necessarily as a reduction in the absolute drive amplitude. Over the same parameter range, the auxiliary quantities A and N_{feed} increase strongly, indicating that the pulse scale associated with the driven dynamics grows with Kerr scaling. Thus, the data show that larger $K_{\text{ham}}/K_{\text{th}}$ requires a smaller relative drive parameter ε_x to reach the first balanced point, even though the overall pulse scale in the protocol increases. The calibrated values of the two-photon pump amplitude A and feed quantity N_{feed} used in the Kerr-scaling study are listed in Appendix A.3.
In terms of fidelity, the influence remains N_{out}-dependent: for $N_{\text{out}} = 3$, increasing the Kerr scaling from 1 to 7 raises the branch-averaged fidelity from 0.991013 to

0.992469 and the worst-case fidelity from 0.985701 to 0.988963, whereas for $N_{\text{out}} = 4$ the corresponding gain in branch-averaged fidelity is very small, from 0.992186 to 0.992212, despite the pronounced shift toward smaller ε_x. For $N_{\text{out}} = 2$, the baseline value $K_{\text{ham}}/K_{\text{th}} = 1$ remains optimal according to the branch-averaged fidelity, while larger Kerr scaling still substantially reduces the relative drive parameter at the balanced point.

N_{out}	$K_{\text{ham}}/K_{\text{th}}$	$\overline{\mathcal{F}}^{(1)}_{\text{eo}}$	$\mathcal{F}^{(1)}_{\text{eo,min}}$	$\mathcal{F}_{\text{eo}}(p_- = 0.5)$	$\epsilon_x(p_- = 0.5)$	$\overline{\eta}^{(1)}_{\text{top}}$
2	1.0	0.991589	0.986455	0.987732	0.045863	0.986776
	6.0	0.986017	0.969728	0.988974	0.007687	0.983732
3	1.0	0.991013	0.985701	0.991278	0.027547	0.990809
	7.0	0.992469	0.988963	0.992650	0.003956	0.992132
4	1.0	0.992186	0.989211	0.992720	0.018717	0.993788
	7.0	0.992212	0.990881	0.992354	0.002680	0.993693

Table 4.4: Comparison between the baseline Kerr-term scaling $K_{\text{ham}}/K_{\text{th}} = 1$ and a high-performing alternative for each N_{out}, evaluated on the truncated first-rotation branch. For $N_{\text{out}} = 2$, the baseline value is also the best-performing one according to the branch-averaged fidelity $\overline{\mathcal{F}}^{(1)}_{\text{eo}}$, so the table instead shows the next-best distinct scaling.

These results support the interpretation that the Kerr nonlinearity acts as a meaningful Hamiltonian confinement resource in the protocol. A natural interpretation is that increasing K_{ham} improves confinement to the cat manifold by enlarging the Kerr-induced energy gap, so that the driven evolution remains closer to the intended logical subspace and requires a smaller one-photon drive relative to the two-photon pump in order to reach the balanced point ($p_- = 0.5$). This provides a physical explanation for why the protocol becomes more drive-efficient in the normalized sense as the Kerr term is increased. At the same time, the modest fidelity improvement in some cases, especially for $N_{\text{out}} = 4$, shows that stronger cat-subspace confinement alone is not sufficient to guarantee uniformly better overall performance, which suggests that other limitations, such as release dynamics or output-mode matching, also become important once leakage out of the cat manifold has been reduced.

4.1.7 Initialization in a logical superposition state

As an additional test of the Kerr-model protocol, initial states prepared directly as logical superpositions in the cat-qubit manifold were also considered, rather than using vacuum initialization followed by generation of the superposition through the applied one-photon drive. The purpose of this test was to examine whether the protocol remained effective when the logical information was already present in the initial state.

The results were found to be qualitatively stable across the scanned superposition weights $p_1 \in [0, 1]$. For $N_{\text{out}} = 2, 3, 4, 5$, the mean even/odd fidelity remained in the range 0.888-0.897, while the mean top-mode efficiency η_{top} remained in the range 0.912-0.955. The dependence on the initial superposition parameter p_1 was relatively

weak, with only a gradual decrease in fidelity and capture efficiency as p_1 was increased. This shows that the protocol does not rely strictly on vacuum initialization, but can also transfer states prepared directly inside the logical cat-qubit manifold, though with a modest performance penalty compared to the vacuum-initialized case. A natural interpretation is that the protocol works best when the logical superposition is created gradually by the one-photon drive during the same evolution that also emits and shapes the output field. When the system is initialized in vacuum, the superposition between the logical cat-qubit components is built up continuously as part of the driven emission process, so that state formation and temporal wave-packet shaping occur in a coordinated way. By contrast, when the system is initialized directly in a logical superposition state, this superposition structure is already present at $t = 0$, and the subsequent pulse no longer creates the state and shapes the outgoing mode in one unified process. A plausible consequence is a slightly less optimal matching between the intracavity dynamics and the target output mode, which can explain the modest decrease in both fidelity and top-mode efficiency as p_1 is increased.
Taken together, these results indicate that direct initialization in the logical cat-qubit manifold is fully compatible with the protocol at a qualitative level, but that the best performance is still obtained when the superposition is generated dynamically during the release process rather than being imposed entirely at the initial time.

4.2 Two-Photon Dissipative Confinement

This section presents results for the two-photon dissipative-confinement model, in which the Kerr nonlinearity is removed from the Hamiltonian ($K_{\mathrm{ham}} = 0$) and confinement of the cat manifold is instead provided by engineered two-photon loss at rate κ_2. The purpose of this analysis was to determine whether dissipative confinement could reproduce the logical-rotation performance obtained in the Kerr-confinement model, and to compare the two approaches in terms of fidelity, mode selectivity, purity, and control requirements.
Unless stated otherwise, the pump and rotation pulses were parameterized using LPF orders $(n_p, n_\varepsilon) = (3, 2)$ and STA was enabled. Figure 4.12 compares the two-photon dissipative-confinement model (colored curves) with $\kappa_2/K_{\mathrm{th}} \in \{1, 2, 3, 4, 5, 6, 7\}$ against the Kerr-confinement reference case, with $K_{\mathrm{ham}}/K_{\mathrm{th}} = 1$, (black markers) for $N_{\mathrm{out}} = 2, 3, 4$ while sweeping ε_x.
Figure 4.12 shows that the two-photon dissipative-confinement model can achieve captured states of comparable quality to those obtained in the Kerr reference model over the first effective rotation branch. For all investigated values $N_{\mathrm{out}} = 2, 3, 4$, increasing the two-photon loss strength improved the performance of the dissipative model, and the best-performing cases occurred at the largest or near-largest investigated values of κ_2/K_{th}. The fitted odd weight varies smoothly along the displayed branch, demonstrating that the dissipative-confinement protocol can interpolate between predominantly even and predominantly odd cat-qubit states in the captured mode. The corresponding fidelities, top-mode efficiencies, and virtual-mode purities remain high throughout the displayed branch, showing that the emitted radiation is still concentrated predominantly into a single capturable temporal mode.

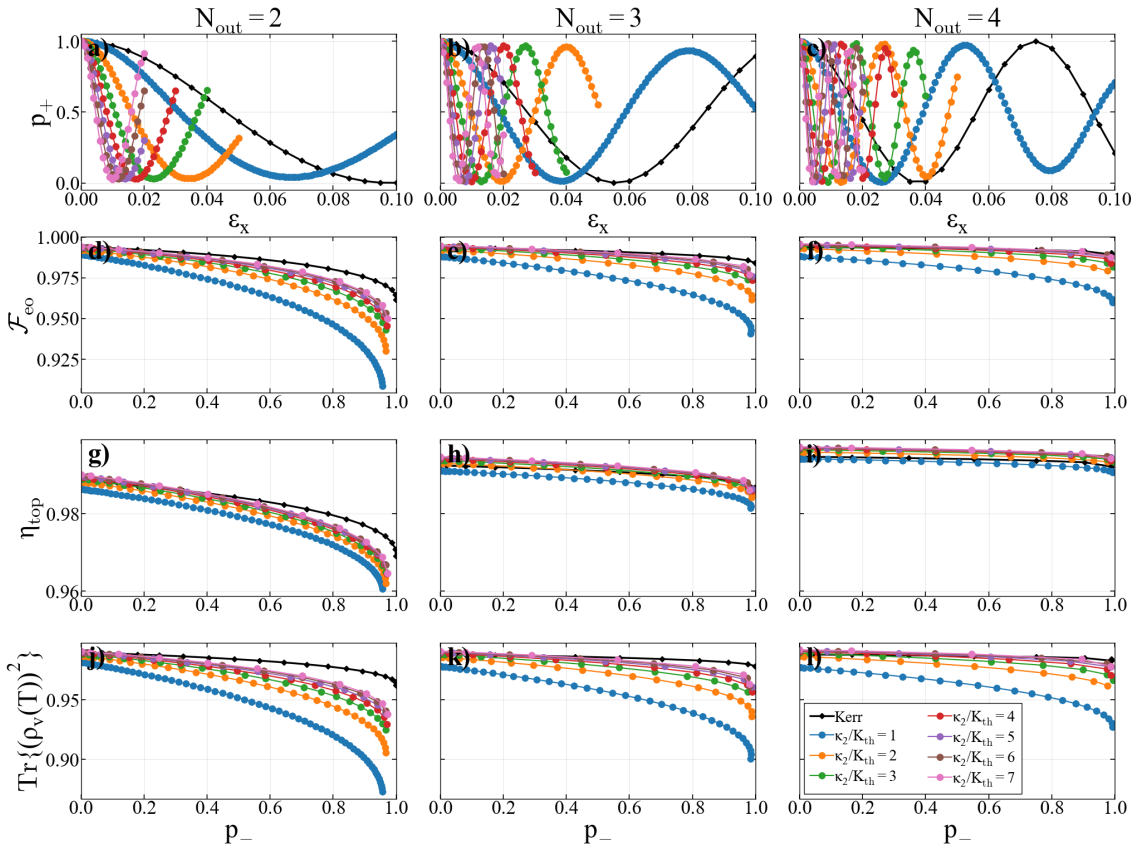

Figure 4.12: Comparison of two-photon dissipative confinement (colored curves) and the Kerr reference model (black diamonds) for $N_{\text{out}} = 2, 3, 4$ (columns), with LPF orders $(n_p, n_\varepsilon) = (3, 2)$ and STA enabled. The dissipative-confinement results are shown for several two-photon loss strengths κ_2/K_{th} (legend). Top row: fitted even weight p_+ versus drive strength ε_x. Second row: even/odd cat-qubit fidelity $\mathcal{F}_{\text{eo}}$ versus fitted odd weight p_-. Third row: top-mode efficiency η_{top} versus p_-. Bottom row: purity of the captured virtual-mode state, $\text{Tr}\{\rho_v(T)^2\}$, versus p_-. For the rows plotted against p_-, the curves are truncated using model- and parameter-dependent cutoffs in ε_x (approximately corresponding to one effective rotation cycle), in order to compare the same branch of the even-to-odd interpolation across different κ_2/K_{th} values and against the Kerr reference.

Table 4.5 compares the Kerr reference model with the best-performing two-photon dissipative-confinement setting for each N_{out}, ranked by the branch-averaged fidelity on the truncated low-ε_x branch used in Figure 4.12. For $N_{\text{out}} = 2$ and 3, the Kerr reference model retains a clear advantage in branch-averaged fidelity, with $\overline{\mathcal{F}}^{(1)}_{\text{eo}} = 0.991589$ and 0.991013, compared with 0.980863 and 0.988249 for the best dissipative-confinement cases. For $N_{\text{out}} = 4$, however, the best two-photon-loss setting slightly outperforms the Kerr reference in both branch-averaged fidelity and balanced-point fidelity, reaching $\overline{\mathcal{F}}^{(1)}_{\text{eo}} = 0.993146$ and $\mathcal{F}_{\text{eo}}(p_- = 0.5) = 0.993535$. Across all three values of N_{out}, the two-photon-loss model reaches the first balanced point at substantially smaller values of ε_x than the Kerr reference model.
A further distinction between the Kerr model and the two-photon-loss model ap-

N_{out}	Model	κ_2/K_{th}	$\overline{\mathcal{F}}_{\text{eo}}^{(1)}$	$\mathcal{F}_{\text{eo,min}}^{(1)}$	$\mathcal{F}_{\text{eo}}(p_- = 0.5)$	$\varepsilon_x(p_- = 0.5)$	$\overline{\eta}_{\text{top}}^{(1)}$
2	Kerr	–	0.991589	0.986455	0.987732	0.045863	0.986776
	2ph loss	7.0	0.980863	0.949958	0.984875	0.004623	0.981746
3	Kerr	–	0.991013	0.985701	0.991278	0.027547	0.990809
	2ph loss	7.0	0.988249	0.976933	0.990768	0.002773	0.991477
4	Kerr	–	0.992186	0.989211	0.992720	0.018717	0.993788
	2ph loss	6.0	0.993146	0.989067	0.993535	0.002209	0.996243

Table 4.5: Comparison between the Kerr-confinement reference model (denoted as *Kerr*) and the best-performing two-photon dissipative-confinement setting (denoted as *2ph loss*) for each N_{out}, where the dissipative case is ranked by the branch-averaged fidelity $\overline{\mathcal{F}}_{\text{eo}}^{(1)}$. All averages and minima are computed on the same truncated low-ε_x branch used in Figure 4.12. The quantity $\mathcal{F}_{\text{eo}}(p_- = 0.5)$ was evaluated at the first occurrence of $p_- = 0.5$ as ε_x increased.

pears in the pump strength required to achieve a given output photon number. While comparable fidelities can be obtained in both models, the optimized two-photon-loss branches require substantially larger values of both the fitted pump amplitude A and the pump quantity N_{feed}. In terms of branch-averaged values, N_{feed} is larger by factors of approximately 193, 194, and 143 for $N_{\text{out}} = 2, 3, 4$, respectively, while the corresponding factors for A are about 13.9, 13.9, and 12.0. More specifically, for $N_{\text{out}} = 2, 3, 4$, the branch-averaged values of N_{feed} are 7.92, 15.88, and 26.67 for the Kerr model, compared with 1530.89, 3076.51, and 3826.18 for the two-photon-loss model. The corresponding mean pump amplitudes are 2.44, 3.45, and 4.48 in the Kerr case, and 33.90, 48.08, and 53.62 in the two-photon-loss case. The corresponding calibration data for the two-photon-loss model are collected in Appendix A.4.

Taken together, these results show that engineered two-photon dissipation can serve as an effective alternative confinement mechanism for cat-qubit generation and rotation. In particular, sufficiently strong two-photon loss rate allows the dissipative-confinement model to approach, and in the $N_{\text{out}} = 4$ case slightly exceed, the Kerr reference on the truncated first-rotation branch.

A plausible interpretation is that the reduced fidelity in the two-photon dissipative-confinement model is connected to the fact that the logical X-rotation is performed in the presence of an active dissipative confinement process. The state is therefore not evolving under a purely coherent Hamiltonian rotation alone, but under a driven open-system dynamics in which the two-photon dissipation continuously stabilizes the cat manifold. This can make the effective logical evolution less ideal and more sensitive to phase errors than in the Kerr-confined case.

The smaller values of $\varepsilon_x(p_- = 0.5)$ in the dissipative model should not be interpreted as showing that the absolute one-photon drive is weaker. Rather, because ε_x was defined through an L^2-normalized intensity relation relative to the two-photon pump pulse, the comparison shows that the dissipative model reaches the balanced point with a smaller normalized one-photon drive fraction, while simultaneously requiring much larger two-photon pump amplitudes and much larger injected two-photon pump strength. The two confinement mechanisms therefore differ not only in how

the cat manifold is stabilized, but also in the control resources required to realize a given logical operation. Overall, the two-photon-loss model demonstrates that high-quality logical rotation and good dominant-mode capture is not unique to Kerr confinement, but the large increase in two-photon pump requirements shows that this alternative operates in a substantially different control regime.

4.3 Noise Robustness: One-Photon Loss and Dephasing

This section evaluates the robustness of the emitted-and-captured cat-qubit states against two common noise channels: pure dephasing and one-photon loss. Both channels were applied to the source oscillator during the protocol, and their impact is quantified on the captured virtual-mode state $\rho_v(T)$ using the same final-state benchmarks as in the noiseless sections. Detailed numerical values are listen in Appendix A.5.

4.3.1 Noise effects in the Kerr (Hamiltonian-confinement) model

The purpose of this analysis was to evaluate how sensitive the Kerr (Hamiltonian-confinement) protocol was to two common noise channels, namely pure dephasing and one-photon loss, and to assess whether simple pulse retuning could partially compensate for the resulting degradation. In particular, the study examined how these noise processes affected the logical rotation trajectory, the cat-qubit fidelity, the dominant-mode selectivity, and the purity of the captured virtual-mode state.
Figure 4.13 summarizes the effect of pure dephasing for $N_{\text{out}} = 2, 3, 4, 5$. For each dephasing strength, $\kappa_\phi \in \{0.0050\kappa_{\text{ex}}, 0.0075\kappa_{\text{ex}}, 0.0100\kappa_{\text{ex}}\}$, the figure reports the resulting fidelity, top-mode efficiency, and purity along the even-to-odd interpolation. In addition, the effect of the two-photon pump time-scaling factor λ_p was investigated as a simple compensation mechanism under dephasing noise. A sweep over $\lambda_p \in \{0.7, 0.9, 1.0, 1.1, 1.3\}$ was performed, and for each $(N_{\text{out}}, \kappa_\phi)$ the best-performing λ_p was selected according to the mean $\mathcal{F}_{\text{eo}}$ over the scanned ε_x values and plotted together with the corresponding baseline curve $\lambda_p = 1.0$. For $N_{\text{out}} = 2, 3, 4$, the largest increase in mean fidelity was obtained for $\lambda_p = 1.1$ for all investigated dephasing strengths, whereas for $N_{\text{out}} = 5$ the corresponding best value was $\lambda_p = 0.9$. The dephasing results show a systematic degradation of performance as κ_ϕ increases. For all investigated values of N_{out}, increasing dephasing lowers the cat-qubit fidelity and the virtual-mode purity along the first rotation branch, while the dominant-mode efficiency remains comparatively less affected. The fitted interpolation from even-like to odd-like states remains visible, but the corresponding states become progressively less pure and less faithful to the ideal cat-qubit targets as the dephasing rate is increased. The additional sweep over λ_p shows that modest retuning of the pump time scale can partially mitigate this degradation, although the improvement is small. For $N_{\text{out}} = 2$ and 3, the selected value $\lambda_p = 1.1$ yields a slight increase in mean fidelity and balanced-point fidelity ($\mathcal{F}_{\text{eo}}(p_- = 0.5)$) relative to the baseline.

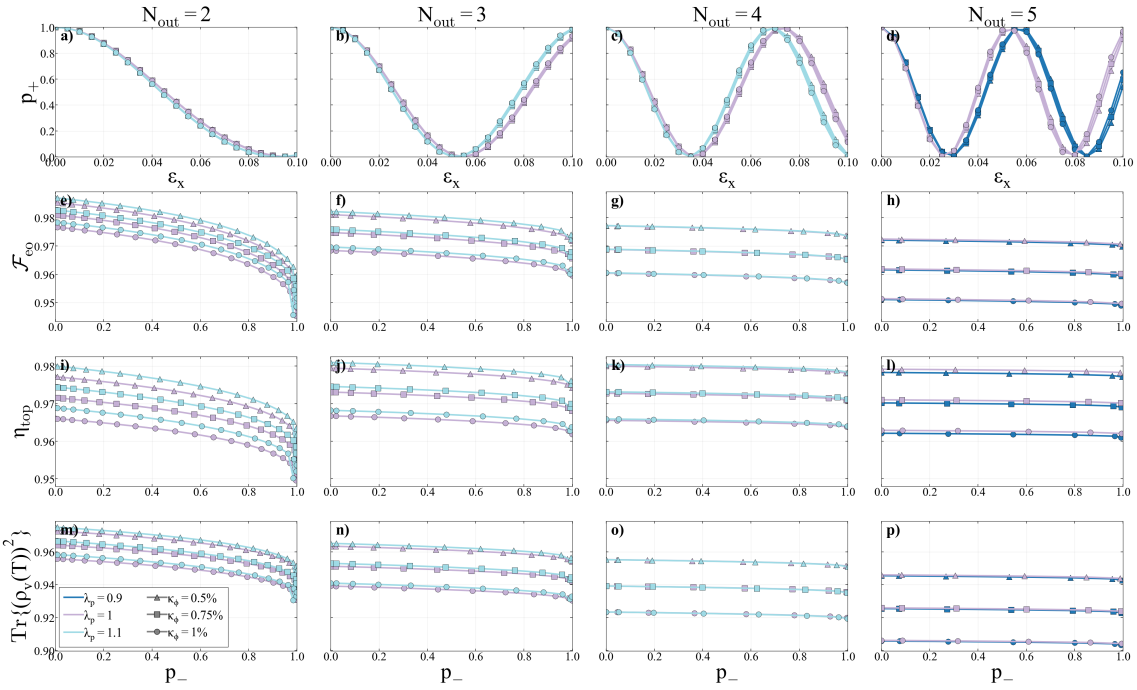

Figure 4.13: Dephasing effects in the Kerr (Hamiltonian-confinement) model for $N_{\text{out}} = 2, 3, 4, 5$ (columns), shown for STA enabled and LPF orders $(n_p, n_\varepsilon) = (3, 2)$, and fixed ε-pulse time scaling $\lambda_\varepsilon = 1.0$. Rows show (top to bottom): fitted even weight p_+ versus drive strength ε_x, even/odd cat-qubit fidelity $\mathcal{F}_{\text{eo}}$ versus fitted odd weight p_-, top-mode efficiency η_{top} versus p_-, and virtual-mode purity $\text{Tr}\{\rho_v(T)^2\}$ versus p_-. Marker shape denotes the dephasing strength κ_ϕ (here $\kappa_\phi = 0.5\%$, 0.75%, 1% of κ_{ex}), while color denotes the pump time-scaling factor λ_p. The plotted dataset combines a baseline set with $\lambda_p = 1.0$ and, for each $(N_{\text{out}}, \kappa_\phi)$, the best-performing λ_p selected from the λ_p sweep according to the mean $\mathcal{F}_{\text{eo}}$ over the ε_x sweep. For the rows plotted against p_-, the curves are truncated using N_{out}- and λ_p-dependent cutoffs in ε_x to retain the first (one-rotation) branch of the even-to-odd interpolation.

For $N_{\text{out}} = 4$, the improvement is negligible, and for $N_{\text{out}} = 5$ the selected value $\lambda_p = 0.9$ slightly changes the performance but does not produce a clear gain on the truncated branch. This indicates that simple pump retuning can provide only limited compensation for dephasing-induced errors.

Figure 4.14 shows the corresponding trends for one-photon loss strengths $\kappa_1 \in \{0.0050\kappa_{\text{ex}}, 0.0075\kappa_{\text{ex}}, 0.0100\kappa_{\text{ex}}\}$. As in the dephasing case, the results are presented along the first rotation branch to enable a consistent comparison across N_{out} and κ_1.

The one-photon-loss results show a similarly systematic degradation with increasing κ_1. For all investigated values of N_{out}, increasing one-photon loss reduces the branch-averaged fidelity, the worst-case fidelity, and the fidelity at the balanced point. The effect is especially clear in the purity and fidelity curves, which shift downward as κ_1 increases. By contrast, the top-mode efficiency remains very high and changes only weakly over the explored loss range. The position of the first balanced point,

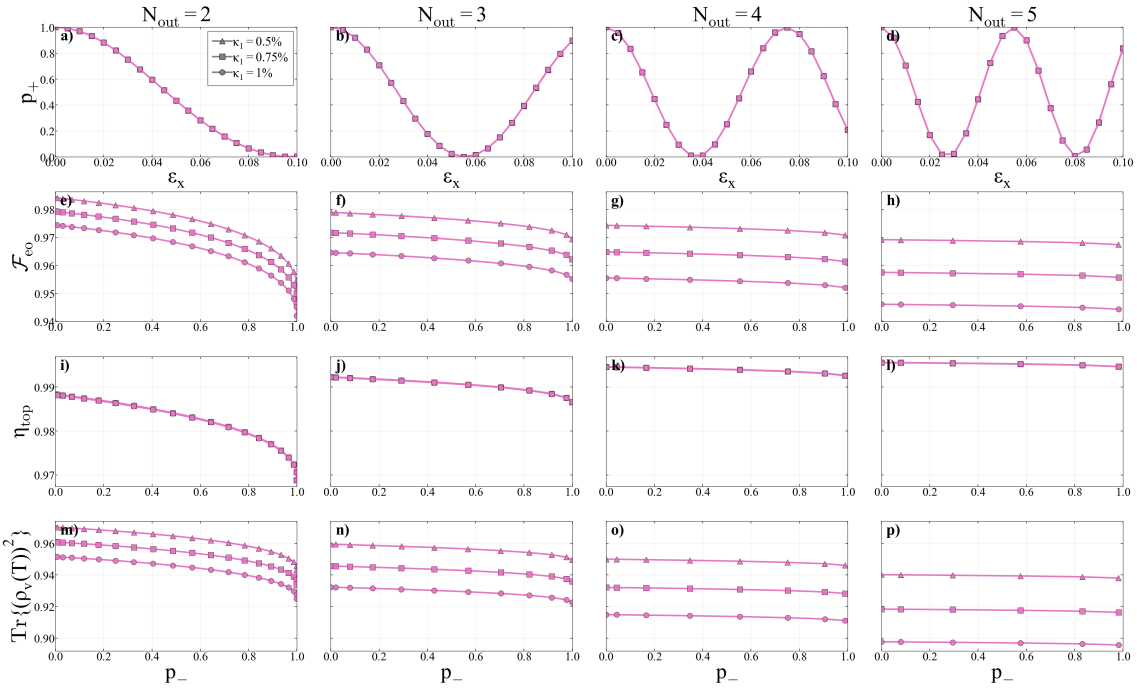

Figure 4.14: One-photon loss effects in the Kerr (Hamiltonian-confinement) model for $N_{\text{out}} = 2, 3, 4, 5$ (columns), shown for STA, LPF orders $(n_p, n_\varepsilon) = (3, 2)$, and fixed pulse time scalings $\lambda_p = \lambda_\varepsilon = 1.0$. Rows show (top to bottom): fitted even weight p_+ versus drive strength ε_x, even/odd cat-qubit fidelity $\mathcal{F}_{\text{eo}}$ versus fitted odd weight p_-, top-mode efficiency η_{top} versus p_-, and virtual-mode purity $\text{Tr}\{\rho_v(T)^2\}$ versus p_-. Marker shape denotes the one-photon loss rate κ_1 (here $\kappa_1 = 0.5\%, 0.75\%, 1\%$ of κ_{ex} in the plotted sweep). For the rows plotted against p_-, the curves are truncated using N_{out}-dependent cutoffs in ε_x to retain the first (one-rotation) branch of the even-to-odd interpolation.

as measured by $\varepsilon_x(p_- = 0.5)$, also remains nearly unchanged, indicating that one-photon loss primarily degrades the quality of the state reached along the logical trajectory rather than strongly altering the location of the trajectory itself in drive space.

Taken together, these results show that the Kerr-confinement protocol is meaningfully affected by both pure dephasing and one-photon loss, although the two noise channels influence the protocol in somewhat different ways. In the dephasing case, increasing κ_ϕ reduces not only the cat-qubit fidelity and the virtual-mode purity, but also the dominant-mode efficiency, indicating that dephasing degrades both the coherence of the captured state and the concentration of the emitted field into a single dominant temporal mode. By contrast, for the investigated range of one-photon loss, the reduction is most clearly seen in the state fidelity and purity, while the top-mode efficiency remains comparatively stable. This suggests that one-photon loss primarily degrades the quality of the encoded state along the logical trajectory, whereas dephasing has a broader impact that also weakens temporal-mode selectivity. The limited improvement obtained by retuning λ_p under dephasing further indicates that these noise effects cannot be fully compensated by simple pulse-scaling adjustments.

Overall, the results show that the Kerr-model protocol remains qualitatively functional under weak noise, but that its achievable performance is ultimately limited by noise-induced degradation of state coherence and, in the case of dephasing, also of mode quality.

4.3.2 Noise effects in the two-photon-loss (dissipative-confinement) model

The purpose of this analysis was to evaluate how sensitive the two-photon-loss (dissipative-confinement) model was to pure dephasing and one-photon loss, and to assess whether the response to these noise channels depended on the strength of the engineered two-photon confinement. In particular, the study compared the noise sensitivity of the dissipative model at fixed $\kappa_2/K_{\mathrm{th}} = 1$ and $\kappa_2/K_{\mathrm{th}} = 3$, and examined how the resulting degradation appeared in the logical rotation trajectory, the cat-qubit fidelity, the dominant-mode efficiency, and the purity of the captured virtual-mode state.

Figures 4.15 and 4.16 show the dephasing results for the two-photon-loss model at fixed $\kappa_2/K_{\mathrm{th}} = 1$ and $\kappa_2/K_{\mathrm{th}} = 3$, respectively, for $N_{\mathrm{out}} = 2, 3, 4$ and dephasing strengths $\kappa_\phi \in \{0.0050\kappa_{\mathrm{ex}}, 0.0075\kappa_{\mathrm{ex}}, 0.0100\kappa_{\mathrm{ex}}, 0.0200\kappa_{\mathrm{ex}}, 0.0300\kappa_{\mathrm{ex}}\}$. As in the Kerr-model dephasing study, a sweep of $\lambda_p \in \{0.7, 0.9, 1.0, 1.1, 1.3\}$ was performed and, for each $(N_{\mathrm{out}}, \kappa_\phi)$, the best-performing value was selected according to the mean $\mathcal{F}_{\mathrm{eo}}$ over the full scanned ε_x interval. For all investigated $N_{\mathrm{out}} = 2, 3, 4$ and all considered dephasing strengths, this full-sweep optimization selected $\lambda_p = 0.7$ in the $\kappa_2/K_{\mathrm{th}} = 1$ case and $\lambda_p = 1.3$ in the $\kappa_2/K_{\mathrm{th}} = 3$ case. In each figure, the selected curve is plotted together with the corresponding baseline curve at $\lambda_p = 1.0$.

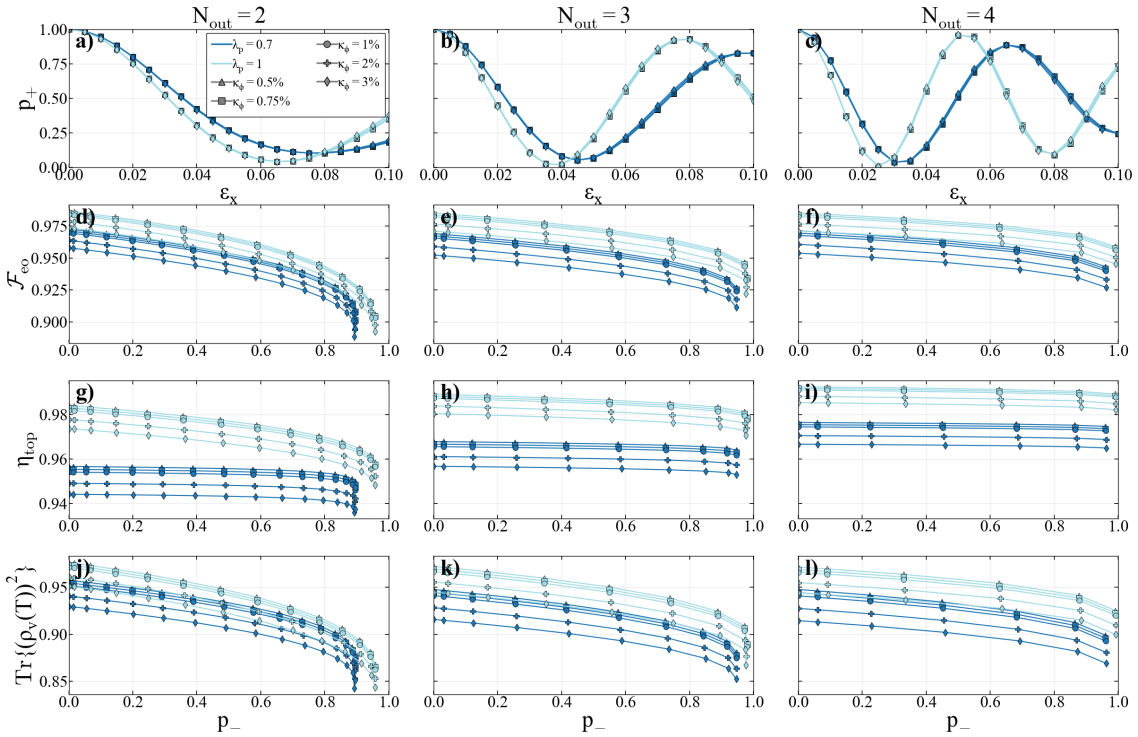

Figure 4.15: Dephasing effects in the two-photon-loss (dissipative-confinement) model for fixed $\kappa_2/K_{\mathrm{th}} = 1$, shown for $N_{\mathrm{out}} = 2, 3, 4$ (columns). All data use STA, LPF orders $(n_p, n_\varepsilon) = (3, 2)$, and fixed ε-pulse time scaling $\lambda_\varepsilon = 1.0$. The dephasing rate is varied over $\kappa_\phi = \{0.5\%, 0.75\%, 1\%, 2\%, 3\%\}$ of κ_{ex} (marker shape), while the pump time-scaling factor λ_p is either fixed to the baseline $\lambda_p = 1$ or chosen from the sweep $\lambda_p \in \{0.7, 0.9, 1.1, 1.3\}$ (colors). For each $(N_{\mathrm{out}}, \kappa_\phi)$, the λ_p value from the sweep is selected by maximizing the mean even/odd cat-qubit fidelity $\mathcal{F}_{\mathrm{eo}}$ over the ε_x scan, and is plotted together with the corresponding baseline curve at $\lambda_p = 1$. Rows show (top to bottom): fitted even weight p_+ versus drive strength ε_x, even/odd cat-qubit fidelity $\mathcal{F}_{\mathrm{eo}}$ versus fitted odd weight p_-, top-mode efficiency η_{top} versus p_-, and virtual-mode purity $\mathrm{Tr}\{\rho_v(T)^2\}$ versus p_-. For the panels plotted against p_-, curves are truncated using N_{out}-dependent cutoffs in ε_x to retain the first (one-rotation) branch of the even-to-odd interpolation.

The dephasing results show that increasing κ_ϕ systematically degrades the performance of the dissipative-confinement model for both values of κ_2/K_{th}. For all investigated values of N_{out}, increasing dephasing lowers the cat-qubit fidelity and the virtual-mode purity along the first rotation branch, while also reducing the dominant-mode efficiency. At the same time, the logical interpolation from even-like to odd-like states remains visible across the sweep.
When comparing $\kappa_2/K_{\mathrm{th}} = 1$ and $\kappa_2/K_{\mathrm{th}} = 3$, however, it is important to distinguish absolute performance from noise robustness. The $\kappa_2/K_{\mathrm{th}} = 3$ case already has a higher zero-noise fidelity than the $\kappa_2/K_{\mathrm{th}} = 1$ case for all investigated N_{out}, so its higher fidelities at finite κ_ϕ do not by themselves imply that it is intrinsically less sensitive to dephasing. Rather, the comparison shows first that stronger two-photon confinement gives a better baseline operating point, and second that both

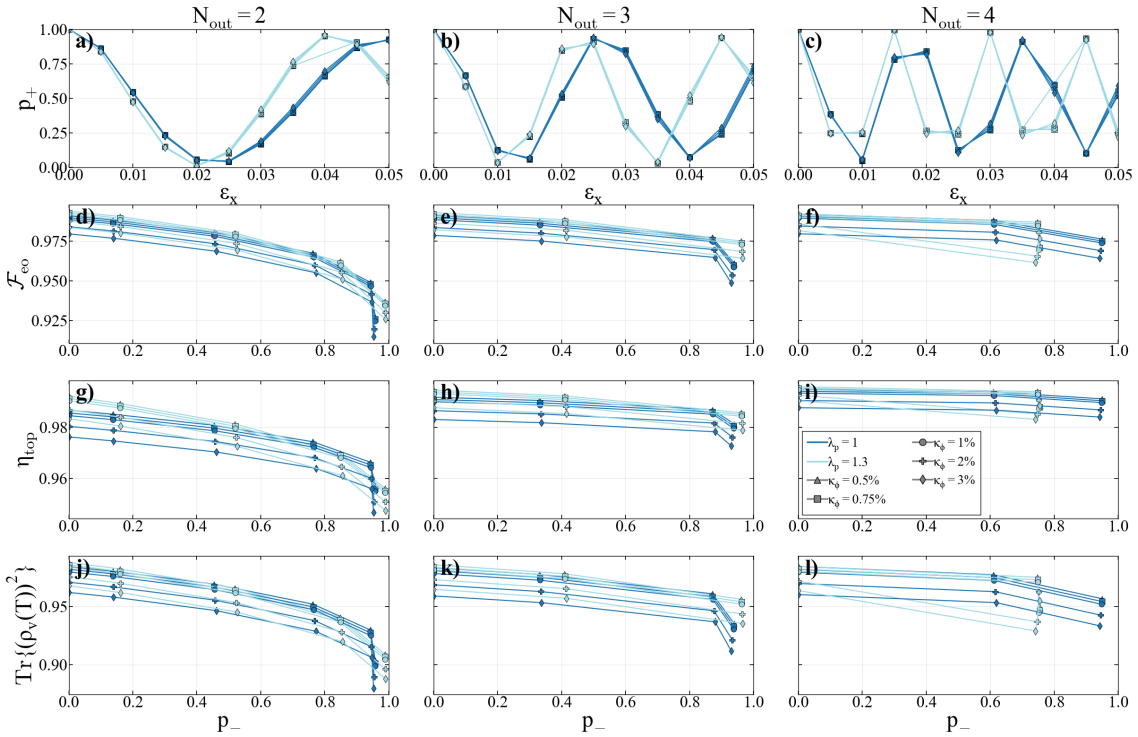

Figure 4.16: Dephasing effects in the two-photon-loss (dissipative-confinement) model for fixed $\kappa_2/K_{\text{th}} = 3$, shown for $N_{\text{out}} = 2, 3, 4$ (columns). All data use STA, LPF orders $(n_p, n_\varepsilon) = (3, 2)$, and fixed ε-pulse time scaling $\lambda_\varepsilon = 1.0$. The dephasing rate is varied over $\kappa_\phi = \{0.5\%, 0.75\%, 1\%, 2\%, 3\%\}$ of κ_{ex} (marker shape), while the pump time-scaling factor λ_p is either fixed to the baseline $\lambda_p = 1$ or chosen from the sweep $\lambda_p \in \{0.7, 0.9, 1.1, 1.3\}$ (colors). For each $(N_{\text{out}}, \kappa_\phi)$, the λ_p value from the sweep is selected by maximizing the mean even/odd cat-qubit fidelity $\mathcal{F}_{\text{eo}}$ over the ε_x scan, and is plotted together with the corresponding baseline curve at $\lambda_p = 1$. Rows show (top to bottom): fitted even weight p_+ versus drive strength ε_x, even/odd cat-qubit fidelity $\mathcal{F}_{\text{eo}}$ versus fitted odd weight p_-, top-mode efficiency η_{top} versus p_-, and virtual-mode purity $\text{Tr}\{\rho_v(T)^2\}$ versus p_-. For the panels plotted against p_-, curves are truncated using N_{out}-dependent cutoffs in ε_x to retain the first (one-rotation) branch of the even-to-odd interpolation.

confinement regimes undergo a systematic degradation as dephasing increases.
The two-photon pump-time retuning also behaves differently in the two cases. For $\kappa_2/K_{\text{th}} = 1$, the full-sweep optimization selects $\lambda_p = 0.7$, but on the truncated first branch this choice does not improve the reported metrics and in fact lowers the fidelity relative to the baseline $\lambda_p = 1.0$ case. By contrast, for $\kappa_2/K_{\text{th}} = 3$, the selected value $\lambda_p = 1.3$ generally improves the branch-averaged fidelity and the balanced-point fidelity for $N_{\text{out}} = 2$ and 3, while the effect is smaller and more mixed for $N_{\text{out}} = 4$. This shows that the usefulness of simple two-photon pump-time retuning depends strongly on the underlying dissipative-confinement regime.

Figures 4.17 and 4.18 present the corresponding one-photon-loss results for the dissipative model at fixed $\kappa_2/K_{\mathrm{th}} = 1$ and $\kappa_2/K_{\mathrm{th}} = 3$, respectively, with $\kappa_\phi = 0$. The investigated one-photon-loss strengths were $\kappa_1 \in \{0.0050\kappa_{\mathrm{ex}}, 0.0075\kappa_{\mathrm{ex}}, 0.0100\kappa_{\mathrm{ex}}, 0.0200\kappa_{\mathrm{ex}}, 0.0300\kappa_{\mathrm{ex}}\}$

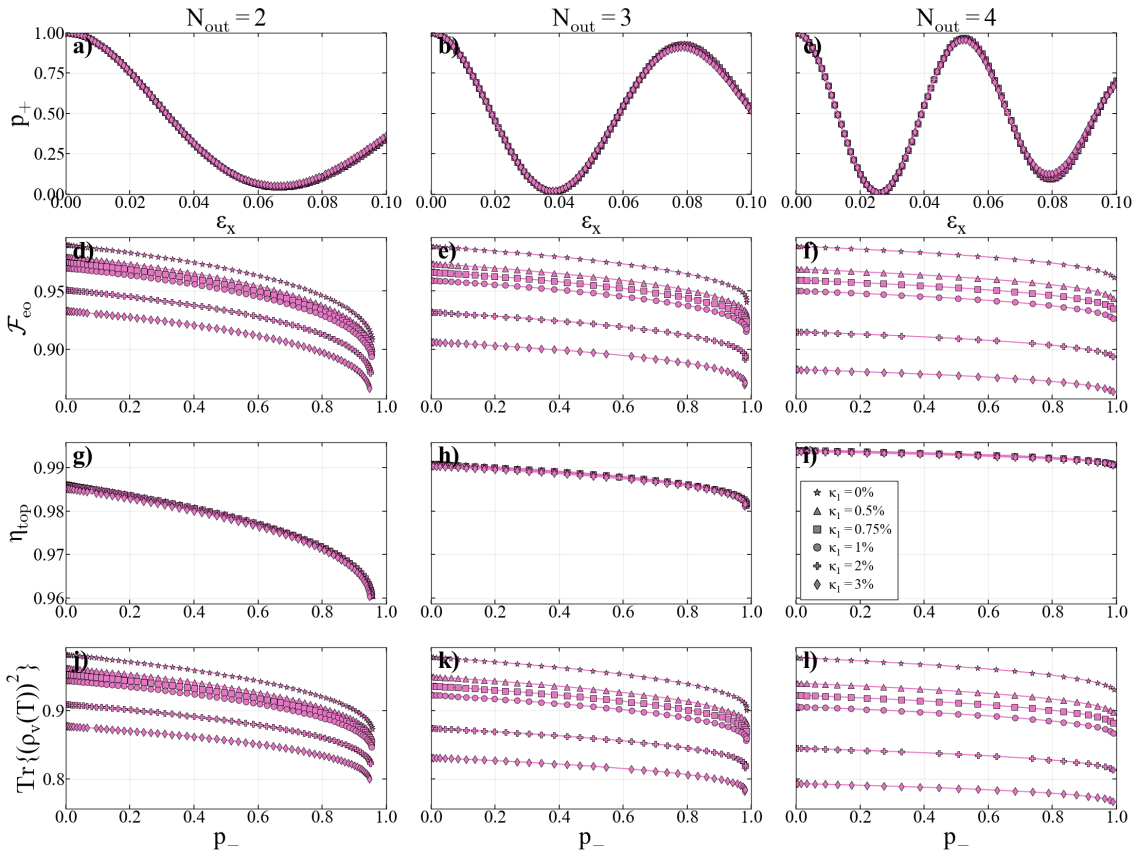

Figure 4.17: One-photon-loss effects in the two-photon-loss (dissipative-confinement) model for fixed $\kappa_2/K_{\mathrm{th}} = 1$, shown for $N_{\mathrm{out}} = 2, 3, 4$ (columns). All data use STA, LPF orders $(n_p, n_\varepsilon) = (3, 2)$, fixed pulse time scalings $\lambda_p = \lambda_\varepsilon = 1.0$, and zero dephasing ($\kappa_\phi = 0$), while the one-photon loss rate is varied over $\kappa_1 = \{0\%, 0.5\%, 0.75\%, 1\%, 2\%, 3\%\}$ of κ_{ex} (marker shape). Rows show (top to bottom): fitted even weight p_+ versus drive strength ε_x, even/odd cat-qubit fidelity $\mathcal{F}_{\mathrm{eo}}$ versus fitted odd weight p_-, top-mode efficiency η_{top} versus p_-, and virtual-mode purity $\mathrm{Tr}\{\rho_v(T)^2\}$ versus p_-. For the panels plotted against p_-, curves are truncated using N_{out}-dependent cutoffs in ε_x to retain the first (one-rotation) branch of the even-to-odd interpolation.

The one-photon-loss results show a similarly systematic reduction in performance with increasing κ_1 for both values of κ_2/K_{th}. In all investigated cases, increasing one-photon loss lowers the cat-qubit fidelity and the virtual-mode purity along the first rotation branch. The dominant-mode efficiency also decreases, but more weakly than the fidelity. At the same time, the value of ε_x required to reach the first balanced point remains nearly unchanged, indicating that one-photon loss primarily degrades the quality of the generated and captured state rather than strongly altering the location of the rotation trajectory in drive space. Comparing the two confinement

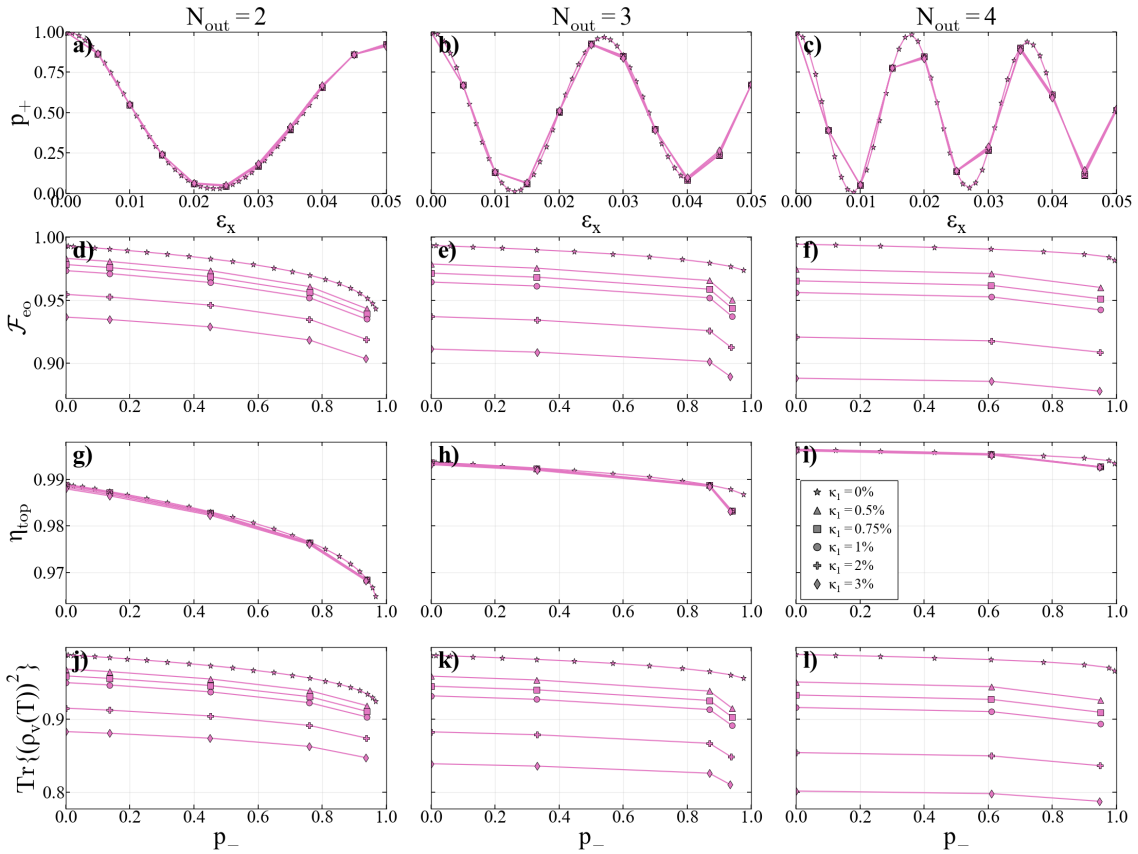

Figure 4.18: One-photon-loss effects in the two-photon-loss (dissipative-confinement) model for fixed $\kappa_2/K_{\text{th}} = 3$, shown for $N_{\text{out}} = 2, 3, 4$ (columns). All data use STA, LPF orders $(n_p, n_\varepsilon) = (3, 2)$, fixed pulse time scalings $\lambda_p = \lambda_\varepsilon = 1.0$, and zero dephasing ($\kappa_\phi = 0$), while the one-photon loss rate is varied over $\kappa_1 = \{0\%, 0.5\%, 0.75\%, 1\%, 2\%, 3\%\}$ of κ_{ex} (marker shape). Rows show (top to bottom): fitted even weight p_+ versus drive strength ε_x, even/odd cat-qubit fidelity $\mathcal{F}_{\text{eo}}$ versus fitted odd weight p_-, top-mode efficiency η_{top} versus p_-, and virtual-mode purity $\text{Tr}\{\rho_v(T)^2\}$ versus p_-. For the panels plotted against p_-, curves are truncated using N_{out}-dependent cutoffs in ε_x to retain the first (one-rotation) branch of the even-to-odd interpolation.

strengths, the case $\kappa_2/K_{\text{th}} = 3$ again retains higher fidelities and purities than $\kappa_2/K_{\text{th}} = 1$ over the same range of one-photon loss, showing that the stronger dissipative confinement case also remains a better operating point also after one-photon loss noise has been added.

Taken together, these results show that the two-photon-loss model is meaningfully affected by both pure dephasing and one-photon loss, with degradation appearing in the state fidelity, the purity, and also the dominant-mode efficiency. At the same time, the protocol remains qualitatively functional over the investigated noise range, in the sense that the even-to-odd interpolation remains visible and the captured states continue to follow the intended logical-rotation path.

A central point in interpreting the comparison between $\kappa_2/K_{\text{th}} = 1$ and $\kappa_2/K_{\text{th}} = 3$ is that stronger dissipative confinement already provides a better zero-noise oper-

ating point. The higher noisy fidelities observed for $\kappa_2/K_{\mathrm{th}} = 3$ therefore reflect, at least in part, this more favorable baseline and should not automatically be read as evidence of strictly lower intrinsic noise sensitivity. A more careful interpretation is that increasing κ_2 improves the underlying dissipative stabilization of the cat manifold, after which both dephasing and one-photon loss produce additional degradation from that baseline. In this sense, stronger engineered two-photon confinement improves the quality of the dissipative operating regime, while the noise channels still impose a clear and systematic performance penalty.

The partial success of pump-time retuning under dephasing further shows that the response to noise depends on the confinement regime: for weaker confinement the retuned pulse does not improve the first-branch performance, whereas for stronger confinement it can provide a modest but systematic improvement, particularly for $N_{\mathrm{out}} = 2$ and 3. Overall, the results suggest that the dissipative-confinement model can tolerate weak noise while remaining operational, but that its achievable performance is limited by the baseline quality of the chosen confinement regime.

5
Conclusion

The aim of this thesis was to investigate how quantum information can be encoded into a propagating microwave mode in a superconducting-circuit setting, with particular focus on traveling two-component cat states and their suitability for communication between superconducting nodes. To this end, numerical protocols were developed for preparing cat-like states in a Kerr-nonlinear parametric oscillator (KPO), releasing them into a transmission line, identifying the dominant temporal output mode, and reconstructing the state of a mode-matched captured field using a virtual-cavity approach. The captured propagating mode was then benchmarked against ideal cat-qubit target states using fidelity, purity, and temporal-mode selectivity.

For the Kerr (Hamiltonian-confinement) model, the results show that the protocol can generate propagating states with both high logical-state quality and high concentration into a single temporal mode. Across all investigated target photon numbers $N_{\text{out}} \in \{2, 3, 4, 5\}$, the LPF-order pair $(n_p, n_\varepsilon) = (3, 2)$ was found to provide the best overall performance when STA was enabled. The corresponding cat-qubit fidelities were consistently high, while the top-mode efficiency also remained high over the investigated parameter range. Taken together, these results show that the emitted field can be shaped such that most of the quantum information is carried by one dominant propagating mode, and that the captured state remains close to the intended cat-qubit manifold throughout the logical interpolation.

The Kerr-model analysis also shows that shortcut-to-adiabaticity is an important ingredient in the protocol. The comparison between simulations with and without STA indicates that STA improves the preparation-and-release dynamics. In addition, the comparison between the extracted dominant mode and the reference profile $\alpha(t) = \sqrt{p(t)/K}$ supports the interpretation that the shaped output remains close to the intended single-mode wave packet, which is central for reliable downstream capture and transfer.

At the same time, the intracavity analysis shows that quantitative agreement with the chosen even-cat reference does not necessarily imply that every instantaneous intracavity Wigner snapshot resembles an ideal textbook cat state. Although the KPO follows the selected even-cat reference well according to the fidelity-based diagnostics, the sampled intracavity Wigner functions do not always display strongly pronounced interference fringes. This is consistent with the fact that, in the present protocol, state generation and release occur simultaneously rather than in two fully separated stages. The intracavity field at a given time therefore represents only the residual field remaining in the KPO, while the relevant cat-state structure is formed in the emitted wave packet. The clearest cat-state signature of the protocol thus appears in the captured traveling mode rather than necessarily in every instantaneous

intracavity snapshot.
The alternative two-photon dissipative-confinement model demonstrates that propagating cat-qubit generation is not limited to the Kerr-confinement mechanism alone. The dissipative protocol also produces a clear even-to-odd logical interpolation and operational traveling states, but the comparison presented in the results chapter shows that its performance depends strongly on the two-photon loss strength. In particular, stronger dissipative confinement gives a better operating point than weaker confinement, while the Kerr reference remains the main benchmark for high-quality performance. This means that engineered dissipation can support traveling bosonic-state generation, but in the present study it does not fully match the quality of the best Kerr-based protocol.
With respect to noise robustness, the comparison suggests that robustness depends on the dominant noise channel rather than on the confinement model alone. Both one-photon loss and pure dephasing reduce the cat-qubit fidelity, the virtual-mode purity, and, depending on the model, also the dominant-mode efficiency. The stronger two-photon-loss model, with $\kappa_2/K_{\mathrm{th}} = 3$, appears to be the most robust against pure dephasing, as it retains the highest fidelities across much of the tested range and remains comparatively stable as κ_ϕ increases. The dephasing results also show that modest additional improvements can be obtained by retuning the pump time scaling λ_p, which suggests that the observed phase-noise sensitivity is not determined solely by the confinement model itself but also by the chosen control parameters. In contrast, the Kerr-confinement model performs slightly better under one-photon loss and therefore appears to provide the most balanced overall robustness. The weaker dissipative-confinement case, with $\kappa_2/K_{\mathrm{th}} = 1$, is generally the most noise-sensitive of the models considered. Taken together, these results indicate that stronger dissipative confinement can improve robustness to phase noise, while the Kerr protocol remains the more favorable compromise when both noise channels are taken into account.
In summary, this thesis shows that it is possible, within the studied theoretical framework, to encode bosonic logical-qubit information into a propagating microwave mode with high fidelity and strong single-mode character. The combination of shaped control pulses, Kerr-based cat-state preparation, and virtual-cavity mode extraction provides a consistent framework for analyzing not only whether a nonclassical state is emitted, but also whether that state is emitted in a form that can realistically be captured and used by a receiving node. This is an important step toward modular superconducting architectures, where the ability to generate, transfer, and recover traveling bosonic code states is a central requirement.
Several natural directions for future work follow from the present results. One is to extend the study from virtual capture of a single dominant temporal mode to a full sender-receiver transfer problem with an explicit receiving node. Another is to include broader classes of imperfections, such as additional control errors, parameter mismatch, or more detailed hardware constraints. Finally, extending the analysis to other bosonic encodings and to full logical-process benchmarks, rather than state benchmarks alone, would clarify the practical usefulness of propagating bosonic code states for distributed quantum computing.

Bibliography

[1] R. P. Feynman, "Simulating physics with computers," *International Journal of Theoretical Physics*, vol. 21, no. 6–7, pp. 467–488, 1982. DOI: 10.1007/BF02650179.

[2] I. Georgescu, S. Ashhab, and F. Nori, "Quantum simulation," *Reviews of Modern Physics*, vol. 86, no. 1, pp. 153–185, Mar. 2014, ISSN: 1539-0756. DOI: 10.1103/revmodphys.86.153. [Online]. Available: http://dx.doi.org/10.1103/RevModPhys.86.153.

[3] Y. Cao et al., "Quantum chemistry in the age of quantum computing," *Chemical Reviews*, vol. 119, no. 19, pp. 10 856–10 915, Aug. 2019, ISSN: 1520-6890. DOI: 10.1021/acs.chemrev.8b00803. [Online]. Available: http://dx.doi.org/10.1021/acs.chemrev.8b00803.

[4] P. Shor, "Algorithms for quantum computation: Discrete logarithms and factoring," in *Proceedings 35th Annual Symposium on Foundations of Computer Science*, 1994, pp. 124–134. DOI: 10.1109/SFCS.1994.365700.

[5] J. Preskill, "Quantum computing in the nisq era and beyond," *Quantum*, vol. 2, p. 79, Aug. 2018, ISSN: 2521-327X. DOI: 10.22331/q-2018-08-06-79. [Online]. Available: http://dx.doi.org/10.22331/q-2018-08-06-79.

[6] B. M. Terhal, "Quantum error correction for quantum memories," *Reviews of Modern Physics*, vol. 87, no. 2, pp. 307–346, Apr. 2015, ISSN: 1539-0756. DOI: 10.1103/revmodphys.87.307. [Online]. Available: http://dx.doi.org/10.1103/RevModPhys.87.307.

[7] M. H. Devoret and R. J. Schoelkopf, "Superconducting circuits for quantum information: An outlook," *Science*, vol. 339, no. 6124, pp. 1169–1174, 2013. DOI: 10.1126/science.1231930. eprint: https://www.science.org/doi/pdf/10.1126/science.1231930. [Online]. Available: https://www.science.org/doi/abs/10.1126/science.1231930.

[8] H. J. Kimble, "The quantum internet," *Nature*, vol. 453, no. 7198, pp. 1023–1030, Jun. 2008, ISSN: 1476-4687. DOI: 10.1038/nature07127. [Online]. Available: http://dx.doi.org/10.1038/nature07127.

[9] A. Joshi, K. Noh, and Y. Y. Gao, "Quantum information processing with bosonic qubits in circuit qed," *Quantum Science and Technology*, vol. 6, no. 3, p. 033 001, Apr. 2021, ISSN: 2058-9565. DOI: 10.1088/2058-9565/abe989. [Online]. Available: http://dx.doi.org/10.1088/2058-9565/abe989.

[10] M. Mirrahimi et al., "Dynamically protected cat-qubits: A new paradigm for universal quantum computation," *New Journal of Physics*, vol. 16, no. 4, p. 045 014, Apr. 2014. DOI: 10.1088/1367-2630/16/4/045014. [Online]. Available: https://doi.org/10.1088/1367-2630/16/4/045014.

[11] A. Grimm et al., "Stabilization and operation of a kerr-cat qubit," *Nature*, vol. 584, no. 7820, pp. 205–209, 2020. DOI: 10.1038/s41586-020-2587-z.

[12] A. H. Kiilerich and K. Mølmer, "Quantum interactions with pulses of radiation," *Phys. Rev. A*, vol. 102, p. 023 717, 2 Aug. 2020. DOI: 10.1103/PhysRevA.102.023717. [Online]. Available: https://link.aps.org/doi/10.1103/PhysRevA.102.023717.

[13] H. Goto, Z. Lin, T. Yamamoto, and Y. Nakamura, "On-demand generation of traveling cat states using a parametric oscillator," *Phys. Rev. A*, vol. 99, p. 023 838, 2 Feb. 2019. DOI: 10.1103/PhysRevA.99.023838. [Online]. Available: https://link.aps.org/doi/10.1103/PhysRevA.99.023838.

[14] H. Goto, "Bifurcation-based adiabatic quantum computation with a nonlinear oscillator network," *Scientific Reports*, vol. 6, p. 21 686, Feb. 2016. DOI: 10.1038/srep21686. [Online]. Available: https://www.nature.com/articles/srep21686.

[15] A. Blais, A. L. Grimsmo, S. Girvin, and A. Wallraff, "Circuit quantum electrodynamics," *Reviews of Modern Physics*, vol. 93, no. 2, May 2021, ISSN: 1539-0756. DOI: 10.1103/revmodphys.93.025005. [Online]. Available: http://dx.doi.org/10.1103/RevModPhys.93.025005.

[16] D. F. Walls and G. J. Milburn, *Quantum Optics* (Springer Study Edition), 1st ed. Berlin, Heidelberg: Springer-Verlag Berlin Heidelberg, 1994, ISBN: 978-3-642-79504-6. DOI: 10.1007/978-3-642-79504-6. [Online]. Available: https://link.springer.com/book/10.1007/978-3-642-79504-6.

[17] S. Puri, S. Boutin, and A. Blais, "Engineering the quantum states of light in a kerr-nonlinear resonator by two-photon driving," *npj Quantum Information*, vol. 3, p. 18, Apr. 2017. DOI: 10.1038/s41534-017-0019-1. [Online]. Available: https://www.nature.com/articles/s41534-017-0019-1.

[18] W. Pfaff et al., "Controlled release of multiphoton quantum states from a microwave cavity memory," *Nature Physics*, vol. 13, pp. 882–887, 2017. DOI: 10.1038/nphys4143.

[19] C. J. Axline et al., "On-demand quantum state transfer and entanglement between remote microwave cavity memories," *Nature Physics*, vol. 14, pp. 705–710, 2018. DOI: 10.1038/s41567-018-0115-y.

[20] M. Khanahmadi, M. M. Lund, K. Mølmer, and G. Johansson, "Multimode character of quantum states released from a superconducting cavity," *Phys. Rev. Res.*, vol. 5, p. 043 071, 4 Oct. 2023. DOI: 10.1103/PhysRevResearch.5.043071. [Online]. Available: https://link.aps.org/doi/10.1103/PhysRevResearch.5.043071.

[21] R. Gautier, A. Sarlette, and M. Mirrahimi, "Combined dissipative and hamiltonian confinement of cat qubits," *PRX Quantum*, vol. 3, no. 2, May 2022, ISSN: 2691-3399. DOI: 10.1103/prxquantum.3.020339. [Online]. Available: http://dx.doi.org/10.1103/PRXQuantum.3.020339.

[22] A. del Campo, "Shortcuts to adiabaticity by counterdiabatic driving," *Phys. Rev. Lett.*, vol. 111, p. 100 502, 10 Sep. 2013. DOI: 10.1103/PhysRevLett.111.100502. [Online]. Available: https://link.aps.org/doi/10.1103/PhysRevLett.111.100502.

[23] S. Puri et al., "Bias-preserving gates with stabilized cat qubits," *Science Advances*, vol. 6, no. 34, Aug. 2020, ISSN: 2375-2548. DOI: 10.1126/sciadv.aay5901. [Online]. Available: http://dx.doi.org/10.1126/sciadv.aay5901.

[24] M. Khanahmadi and K. Mølmer, *Environment-assisted generation of non-gaussian wavepacket quantum states*, 2025. arXiv: 2504.04513 [quant-ph]. [Online]. Available: https://arxiv.org/abs/2504.04513.

[25] C. W. Gardiner and M. J. Collett, "Input and output in damped quantum systems: Quantum stochastic differential equations and the master equation," *Phys. Rev. A*, vol. 31, pp. 3761–3774, 6 Jun. 1985. DOI: 10.1103/PhysRevA.31.3761. [Online]. Available: https://link.aps.org/doi/10.1103/PhysRevA.31.3761.

[26] M. A. Nielsen and I. L. Chuang, *Quantum Computation and Quantum Information*, 10th Anniversary Edition. Cambridge University Press, 2010.

A

Supplementary results, parameter scans, and robustness data

This appendix collects supplementary figures, tables, and parameter-scan results that support the main conclusions of the thesis but are too detailed to include in the main text. The material is organized to mirror the structure of the results chapter: first, additional pulse-shape and STA comparisons for the Hamiltonian-confinement (Kerr) model; second, supplementary parameter scans for Kerr scaling and the two-photon-loss model; and finally, detailed robustness data for dephasing and one-photon loss.
Unless stated otherwise, all quantities are defined as in the main text, and the reported metrics are evaluated using the same truncation, calibration, and branch-selection procedures as in the corresponding main-text figures. In particular, when data are shown as functions of the fitted odd weight p_-, the curves are truncated to retain the first effective rotation branch, so that different parameter sets are comparable.

A.1 Low-pass filter order study

For completeness, Figure A.1 compare the LPF-order scans with and without STA for the Kerr model. The purpose of this comparison is to show that the favorable low-pass-filter region is not an isolated point, but part of a broader and relatively stable trend across the considered target photon numbers.
Overall, the scans indicate that the same general LPF-order region remains favorable across all investigated N_{out}-values with STA enabled. This supports the use of the baseline choice $(n_p, n_\varepsilon) = (3, 2)$ in the main study, since it remains close to optimal across the investigated cases while providing a consistent reference point for the remaining parameter sweeps.

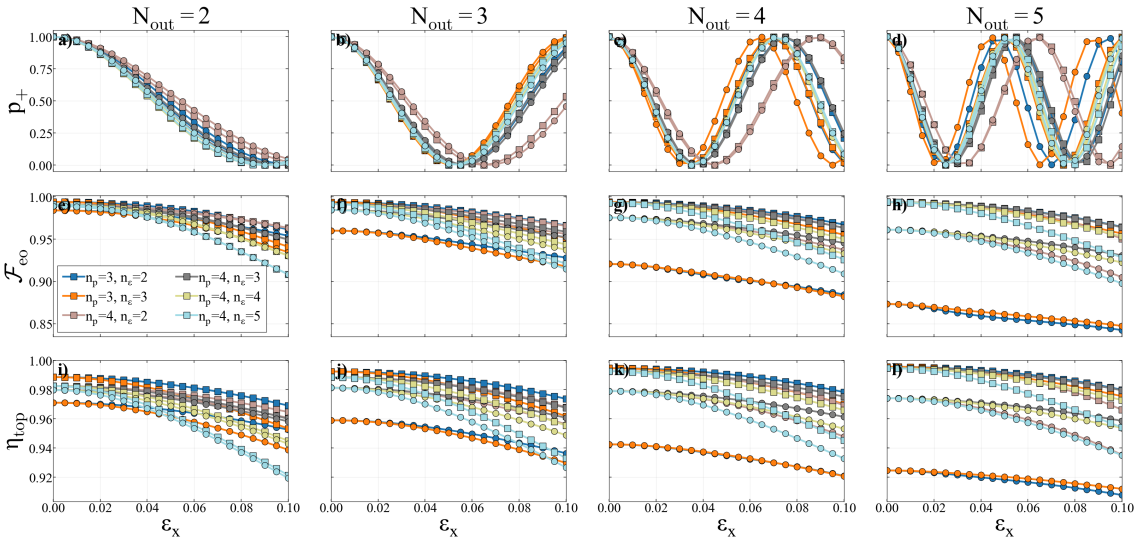

Figure A.1: Even-cat population p_+ (top row), even/odd cat-qubit fidelity $\mathcal{F}_{\text{eo}}$ (middle row), and top-mode population η_{top} (bottom row) as functions of the normalized one-photon-drive amplitude ε_x. The four columns correspond to target photon numbers $N_{\text{out}} = 2, 3, 4, 5$. Each color denotes a different low-pass-filter order pair (n_p, n_ε), while the marker distinguishes the cases with STA (square) and without STA (circle).

A.2 Comparison of protocols with and without STA

Table A.1 summarizes the comparison between protocols with STA disabled and enabled, complementing the corresponding main-text figure (Figure 4.4) with branch-averaged performance metrics. The table reports the even/odd cat-qubit fidelity $\mathcal{F}_{\text{eo}}^{(1)}$ and the top-mode efficiency $\eta_{\text{top}}^{(1)}$ evaluated on the first effective rotation branch for each N_{out}.

The results show that including STA improves both $\mathcal{F}_{\text{eo}}$ and η_{top}, with the improvement becoming more pronounced at larger target photon numbers. This quantitative comparison supports the choice to include STA in the main parameter studies.

N_{out}	Protocol	$\overline{\mathcal{F}}_{\text{eo}}^{(1)}$	$\overline{\eta}_{\text{top}}^{(1)}$
2	no STA	0.9737	0.9644
2	with STA	0.9831	0.9817
3	no STA	0.9547	0.9561
3	with STA	0.9903	0.9904
4	no STA	0.9175	0.9412
4	with STA	0.9929	0.9941

Table A.1: Branch-averaged even/odd fidelity $\overline{\mathcal{F}}_{\text{eo}}^{(1)}$ and top-mode efficiency $\overline{\eta}_{\text{top}}^{(1)}$ for the STA comparison shown in Figure 4.4, using the first effective rotation branch for each N_{out}.

A.3 Calibration data for Kerr-strength scaling

This section collects supplementary calibration data for the Kerr-scaling study presented in the main text. Table A.3 reports the calibrated two-photon pump amplitude A and feed quantity N_{feed} for different values of the normalized Kerr strength $K_{\text{ham}}/K_{\text{th}}$ and target photon numbers N_{out}.
The purpose of including these values is to make the rescaling procedure transparent and to document how the operating point shifts as the Hamiltonian Kerr strength is varied while the threshold-based normalization is kept fixed. This data is primarily included for reproducibility and for interpreting the trends observed in the main-text Kerr-scaling results.

N_{out}	$K_{\text{ham}}/K_{\text{th}}$	$\overline{A}^{(1)}$	$\overline{N}^{(1)}_{\text{feed}}$
2	1.0	2.485360	8.220334
	2.0	4.837934	31.164094
	3.0	7.231223	69.624298
	4.0	9.627635	123.421570
	5.0	12.034484	192.847371
	6.0	14.470525	278.807764
	7.0	16.869908	378.949377
3	1.0	3.457024	15.903671
	2.0	6.880628	63.001864
	3.0	10.289999	140.905789
	4.0	13.695567	249.607666
	5.0	17.099044	389.084459
	6.0	20.521158	560.407480
	7.0	23.965355	764.302794
4	1.0	4.476875	26.670945
	2.0	8.965859	106.972650
	3.0	13.452570	240.823829
	4.0	17.867687	424.840429
	5.0	22.275277	660.291169
	6.0	26.702200	948.818619
	7.0	31.135917	1290.067476

Table A.2: Comparison of two-photon pump amplitude A and feed N_{feed} between different Kerr-term scalings $K_{\text{ham}}/K_{\text{th}} \in \{1, 2, 3, 4, 5, 6, 7\}$ for each $N_{\text{out}} \in \{2, 3, 4\}$, evaluated on the truncated first-rotation branch.

A.4 Calibration data for the two-photon-loss model

This section provides supplementary calibration data for the two-photon dissipative-confinement model discussed in the main text. The corresponding table lists the calibrated two-photon pump amplitude A and feed quantity N_{feed} for different values of the normalized two-photon loss rate κ_2/K_{th} and target photon numbers N_{out}.

These values are included to make it easier to compare the dissipative-confinement model with the Kerr reference case on equal footing and to clarify how the operating points were selected for the parameter scans.

N_{out}	κ_2/K_{th}	$\overline{A}^{(1)}$	$\overline{N}^{(1)}_{\mathrm{feed}}$
2	1.0	5.066281	34.182944
	2.0	9.821080	128.462905
	3.0	14.633084	285.171271
	4.0	19.403609	501.460940
	5.0	24.257370	783.650032
	6.0	29.041275	1123.283422
	7.0	33.901297	1530.891538
3	1.0	7.141615	67.873511
	2.0	13.939079	258.568641
	3.0	20.791429	575.269763
	4.0	27.599529	1013.706461
	5.0	34.436192	1578.119329
	6.0	41.247478	2264.166102
	7.0	48.080845	3076.510882
4	1.0	9.208895	112.850859
	2.0	18.061829	434.123069
	3.0	26.932242	965.239126
	4.0	35.814121	1706.863338
	5.0	44.720628	2661.371482
	6.0	53.621344	3826.176487
	7.0	62.491169	5196.696930

Table A.3: Comparison of two-photon pump amplitude A and feed N_{feed} between different two photon loss rates $\kappa 2/K_{\mathrm{th}} \in \{1, 2, 3, 4, 5, 6, 7\}$ for each $N_{\mathrm{out}} \in \{2, 3, 4\}$, evaluated on the truncated first-rotation branch.

A.5 Supplementary noise-robustness data

This section gathers the numerical summary tables corresponding to the noise-robustness analysis in the main text. Whereas the main figures emphasize the qualitative trends, the tables collected here provide the underlying branch-averaged metrics and selected comparison points in compact form. This allows a more direct comparison of how dephasing and one-photon loss affect the fidelity and mode selectivity of the captured traveling state in both confinement models.

A.5.1 Effect of dephasing in the Kerr model

Table A.4 compares the baseline pump-time scaling $\lambda_p = 1.0$ with the value selected from the λ_p sweep for each pair $(N_{\text{out}}, \kappa_\phi)$. The purpose is to quantify whether retuning the pump duration can partially mitigate the effect of dephasing in the Hamiltonian-confinement (Kerr) model.

N_{out}	$\kappa_\phi/\kappa_{\text{ex}}$	λ_p	$\overline{\mathcal{F}}_{\text{eo}}^{(1)}$	$\mathcal{F}_{\text{eo,min}}^{(1)}$	$\mathcal{F}_{\text{eo}}(p_- = 0.5)$	$\epsilon_x(p_- = 0.5)$	$\overline{\eta}_{\text{top}}^{(1)}$
2	0.0050	1.0	0.974596	0.953361	0.979139	0.045547	0.970950
		1.1	0.975706	0.953540	0.980914	0.043994	0.972917
2	0.0075	1.0	0.970341	0.949376	0.974858	0.045420	0.965645
		1.1	0.971483	0.949583	0.976660	0.043867	0.967628
2	0.0100	1.0	0.966097	0.945403	0.970597	0.045257	0.960382
		1.1	0.967272	0.945638	0.972425	0.043704	0.962380
3	0.0050	1.0	0.977763	0.971791	0.978674	0.027259	0.977650
		1.1	0.978699	0.972433	0.979885	0.025971	0.978946
3	0.0075	1.0	0.971496	0.965664	0.972402	0.027115	0.971340
		1.1	0.972454	0.966308	0.973635	0.025826	0.972620
3	0.0100	1.0	0.965242	0.959548	0.966144	0.026962	0.965076
		1.1	0.966220	0.960192	0.967395	0.025685	0.966339
4	0.0050	1.0	0.975885	0.973726	0.976123	0.018423	0.979353
		1.1	0.975843	0.973509	0.976208	0.017389	0.979698
4	0.0075	1.0	0.967556	0.965449	0.967798	0.018279	0.972121
		1.1	0.967518	0.965221	0.967887	0.017256	0.972438
4	0.0100	1.0	0.959236	0.957181	0.959481	0.018145	0.964933
		1.1	0.959199	0.956938	0.959572	0.017116	0.965221
5	0.0050	1.0	0.971769	0.970667	0.971884	0.013399	0.978860
		0.9	0.971229	0.969761	0.971514	0.014448	0.977881
5	0.0075	1.0	0.961253	0.960174	0.961373	0.013266	0.970702
		0.9	0.960758	0.959339	0.961042	0.014302	0.969772
5	0.0100	1.0	0.950737	0.949680	0.950861	0.013143	0.962582
		0.9	0.950292	0.948921	0.950574	0.014162	0.961702

Table A.4: Comparison between the baseline pump time scaling $\lambda_p = 1.0$ and the value selected from the λ_p sweep for each $(N_{\text{out}}, \kappa_\phi)$. The selected value is determined from the mean $\mathcal{F}_{\text{eo}}$ over the full scanned ε_x interval, while the metrics reported here are evaluated on the same truncated low-ε_x branch used in Figure 4.13. The quantity $\mathcal{F}_{\text{eo}}(p_- = 0.5)$ is evaluated at the first occurrence of $p_- = 0.5$ as ε_x increases.

A.5.2 Effect of one-photon loss in the Kerr model

Table A.5 reports the effect of one-photon loss in the Kerr model for $N_{\mathrm{out}} = 2, 3, 4, 5$. The table complements the corresponding main-text figure by listing the branch-level metrics used to compare the degradation in performance as κ_1 increases.

N_{out}	$\kappa_1/\kappa_{\mathrm{ex}}$	$\overline{\mathcal{F}}^{(1)}_{\mathrm{eo}}$	$\mathcal{F}^{(1)}_{\mathrm{eo,min}}$	$\mathcal{F}_{\mathrm{eo}}(p_- = 0.5)$	$\epsilon_x(p_- = 0.5)$	$\overline{\eta}^{(1)}_{\mathrm{top}}$
2	0.0050	0.973252	0.951596	0.977798	0.045874	0.981537
	0.0075	0.968381	0.946782	0.972915	0.045877	0.981457
	0.0100	0.963561	0.942013	0.968084	0.045881	0.981378
3	0.0050	0.975583	0.969383	0.976489	0.027560	0.990315
	0.0075	0.968370	0.962198	0.969275	0.027540	0.990266
	0.0100	0.961266	0.955120	0.962168	0.027535	0.990216
4	0.0050	0.973027	0.970790	0.973254	0.018688	0.993889
	0.0075	0.963543	0.961323	0.963768	0.018689	0.993858
	0.0100	0.954249	0.952044	0.954472	0.018691	0.993825
5	0.0050	0.968520	0.967395	0.968622	0.013658	0.995253
	0.0075	0.956829	0.955715	0.956930	0.013653	0.995231
	0.0100	0.945427	0.944326	0.945527	0.013652	0.995209

Table A.5: Effect of one-photon loss in the Kerr-confinement model for $N_{\mathrm{out}} = 2, 3, 4, 5$. All metrics are computed on the same truncated low-ε_x branch used in Figure 4.14. The quantity $\mathcal{F}_{\mathrm{eo}}(p_- = 0.5)$ is evaluated at the first occurrence of $p_- = 0.5$ as ε_x increases.

A.5.3 Effect of dephasing for $\kappa_2/K_{\mathrm{th}} = 1$

Table A.6 summarizes the effect of optimizing λ_p in the two-photon-loss model at fixed $\kappa_2/K_{\mathrm{th}} = 1$ under dephasing. It is included to show whether the same retuning strategy used in the Kerr model remains beneficial in the two-photon dissipative-confinement setting.

N_{out}	$\kappa_\phi/\kappa_{\mathrm{ex}}$	λ_p	$\overline{\mathcal{F}}^{(1)}_{\mathrm{eo}}$	$\mathcal{F}^{(1)}_{\mathrm{eo,min}}$	$\mathcal{F}_{\mathrm{eo}}(p_- = 0.5)$	$\epsilon_x(p_- = 0.5)$	$\overline{\eta}^{(1)}_{\mathrm{top}}$
2	0.0050	1.0	0.957643	0.905877	0.966552	0.031156	0.974593
		0.7	0.945510	0.902737	0.953730	0.035897	0.954324
2	0.0075	1.0	0.956296	0.904526	0.965233	0.031130	0.973537
		0.7	0.944015	0.901263	0.952266	0.035853	0.953053
2	0.0100	1.0	0.954953	0.903176	0.963951	0.031081	0.972485
		0.7	0.942526	0.899799	0.950824	0.035798	0.951786
2	0.0200	1.0	0.949620	0.897834	0.958758	0.030961	0.968319
		0.7	0.936617	0.893987	0.945067	0.035601	0.946771
2	0.0300	1.0	0.944351	0.892572	0.953662	0.030814	0.964219
		0.7	0.930788	0.888278	0.939334	0.035461	0.941834
3	0.0050	1.0	0.967183	0.935568	0.973449	0.018808	0.985604
		0.7	0.953204	0.927011	0.956448	0.022651	0.966551
3	0.0075	1.0	0.965763	0.934202	0.972039	0.018788	0.984723
		0.7	0.951540	0.925430	0.954805	0.022616	0.965418
3	0.0100	1.0	0.964348	0.932837	0.970640	0.018765	0.983847
		0.7	0.949881	0.923854	0.953168	0.022584	0.964289
3	0.0200	1.0	0.958737	0.927435	0.965067	0.018683	0.980376
		0.7	0.943306	0.917609	0.946667	0.022457	0.959821
3	0.0300	1.0	0.953195	0.922106	0.959567	0.018602	0.976962
		0.7	0.936829	0.911481	0.940252	0.022337	0.955428
4	0.0050	1.0	0.975583	0.958995	0.977939	0.012869	0.991452
		0.7	0.960875	0.943278	0.962519	0.016094	0.975874
4	0.0075	1.0	0.974163	0.957611	0.976522	0.012856	0.990723
		0.7	0.959142	0.941616	0.960799	0.016077	0.974875
4	0.0100	1.0	0.972747	0.956228	0.975116	0.012843	0.989998
		0.7	0.957412	0.939950	0.959092	0.016051	0.973881
4	0.0200	1.0	0.967125	0.950743	0.969524	0.012795	0.987126
		0.7	0.950564	0.933395	0.952303	0.015970	0.969947
4	0.0300	1.0	0.961571	0.945323	0.964006	0.012740	0.984303
		0.7	0.943818	0.926937	0.945630	0.015875	0.966081

Table A.6: Comparison between the baseline pump time scaling $\lambda_p = 1.0$ and the value selected from the λ_p sweep for the two-photon-loss model at fixed $\kappa_2/K_{\mathrm{th}} = 1$. The selected value is determined from the mean $\mathcal{F}_{\mathrm{eo}}$ over the full scanned ε_x interval, while the metrics reported here are evaluated on the same truncated low-ε_x branch used in Figure 4.15. The quantity $\mathcal{F}_{\mathrm{eo}}(p_- = 0.5)$ is evaluated at the first occurrence of $p_- = 0.5$ as ε_x increases.

A.5.4 Effect of one-photon loss for $\kappa_2/K_{\mathrm{th}} = 1$

Table A.7 lists the corresponding branch-level performance metrics for one-photon loss in the two-photon-loss model at fixed $\kappa_2/K_{\mathrm{th}} = 1$.

N_{out}	$\kappa_1/\kappa_{\mathrm{ex}}$	$\overline{\mathcal{F}}_{\mathrm{eo}}^{(1)}$	$\mathcal{F}_{\mathrm{eo,min}}^{(1)}$	$\mathcal{F}_{\mathrm{eo}}(p_- = 0.5)$	$\epsilon_x(p_- = 0.5)$	$\overline{\eta}_{\mathrm{top}}^{(1)}$
2	0.0050	0.952121	0.901199	0.960056	0.031221	0.976807
	0.0075	0.947702	0.897562	0.955535	0.031213	0.976744
	0.0100	0.943332	0.893964	0.951024	0.031243	0.976680
	0.0200	0.926331	0.879992	0.933556	0.031276	0.976417
	0.0300	0.909748	0.866663	0.916861	0.031297	0.976021
3	0.0050	0.957616	0.927848	0.962204	0.018857	0.987614
	0.0075	0.950778	0.921634	0.955269	0.018856	0.987571
	0.0100	0.944045	0.915516	0.948444	0.018856	0.987528
	0.0200	0.918142	0.892022	0.922178	0.018850	0.987353
	0.0300	0.893777	0.870015	0.897503	0.018846	0.987160
4	0.0050	0.960226	0.943776	0.962035	0.012891	0.992949
	0.0075	0.951063	0.935048	0.952814	0.012897	0.992921
	0.0100	0.942083	0.926496	0.943791	0.012899	0.992893
	0.0200	0.907881	0.894018	0.909485	0.012881	0.992767
	0.0300	0.876484	0.864132	0.877854	0.012875	0.992654

Table A.7: Effect of one-photon loss in the two-photon-loss model at fixed $\kappa_2/K_{\mathrm{th}} = 1$ for $N_{\mathrm{out}} = 2, 3, 4$. All metrics are computed on the same truncated low-ε_x branch used in the corresponding figure. The quantity $\mathcal{F}_{\mathrm{eo}}(p_- = 0.5)$ is evaluated at the first occurrence of $p_- = 0.5$ as ε_x increases.

A.5.5 Effect of dephasing for $\kappa_2/K_{\mathrm{th}} = 3$

Table A.8 presents the optimized-λ_p comparison for the stronger dissipative-confinement setting $\kappa_2/K_{\mathrm{th}} = 3$, allowing direct comparison with the $\kappa_2/K_{\mathrm{th}} = 1$ case.

N_{out}	$\kappa_\phi/\kappa_{\mathrm{ex}}$	λ_p	$\overline{\mathcal{F}}^{(1)}_{\mathrm{eo}}$	$\mathcal{F}^{(1)}_{\mathrm{eo,min}}$	$\mathcal{F}_{\mathrm{eo}}(p_- = 0.5)$	$\epsilon_x(p_- = 0.5)$	$\overline{\eta}^{(1)}_{\mathrm{top}}$
2	0.0050	1.0	0.967141	0.927131	0.978439	0.010747	0.975111
		1.3	0.972570	0.936827	0.980519	0.009737	0.977845
2	0.0075	1.0	0.965926	0.925882	0.977232	0.010741	0.974046
		1.3	0.971481	0.935698	0.979451	0.009727	0.976948
2	0.0100	1.0	0.964713	0.924623	0.976078	0.010724	0.972985
		1.3	0.970399	0.934582	0.978373	0.009721	0.976054
2	0.0200	1.0	0.959899	0.919638	0.971396	0.010683	0.968785
		1.3	0.966100	0.930144	0.974149	0.009684	0.972514
2	0.0300	1.0	0.955140	0.914735	0.966792	0.010632	0.964651
		1.3	0.961845	0.925748	0.969981	0.009641	0.969032
3	0.0050	1.0	0.979105	0.961014	0.984192	0.006561	0.987749
		1.3	0.985332	0.974906	0.986114	0.005816	0.990982
3	0.0075	1.0	0.977850	0.959776	0.982934	0.006554	0.986861
		1.3	0.984237	0.973811	0.985030	0.005811	0.990275
3	0.0100	1.0	0.976595	0.958532	0.981696	0.006545	0.985978
		1.3	0.983154	0.972724	0.983956	0.005806	0.989571
3	0.0200	1.0	0.971619	0.953629	0.976738	0.006521	0.982481
		1.3	0.978821	0.968388	0.979667	0.005786	0.986787
3	0.0300	1.0	0.966701	0.948783	0.971838	0.006497	0.979042
		1.3	0.974532	0.964098	0.975417	0.005767	0.984049
4	0.0050	1.0	0.985290	0.976165	0.988586	0.004096	0.993411
		1.3	0.983495	0.971652	0.988538	0.003345	0.992893
4	0.0075	1.0	0.984047	0.974940	0.987344	0.004089	0.992679
		1.3	0.982447	0.970620	0.987488	0.003340	0.992338
4	0.0100	1.0	0.982817	0.973723	0.986109	0.004084	0.991951
		1.3	0.981394	0.969584	0.986427	0.003339	0.991785
4	0.0200	1.0	0.977905	0.968878	0.981182	0.004064	0.989068
		1.3	0.977210	0.965463	0.982225	0.003327	0.989597
4	0.0300	1.0	0.973048	0.964073	0.976323	0.004040	0.986235
		1.3	0.973070	0.961381	0.978070	0.003315	0.987446

Table A.8: Comparison between the baseline pump time scaling $\lambda_p = 1.0$ and the value selected from the λ_p sweep for the two-photon-loss model at fixed $\kappa_2/K_{\mathrm{th}} = 3$. The selected value is determined from the mean $\mathcal{F}_{\mathrm{eo}}$ over the full scanned ε_x interval, while the metrics reported here are evaluated on the same truncated low-ε_x branch used in the corresponding figure. The quantity $\mathcal{F}_{\mathrm{eo}}(p_- = 0.5)$ is evaluated at the first occurrence of $p_- = 0.5$ as ε_x increases.

A.5.6 Effect of one-photon loss for $\kappa_2/K_{\mathrm{th}} = 3$

Table A.9 reports the effect of one-photon loss in the two-photon-loss model for $\kappa_2/K_{\mathrm{th}} = 3$, thereby completing the robustness comparison across the two dissipative-confinement settings considered in this thesis.

N_{out}	$\kappa_1/\kappa_{\mathrm{ex}}$	$\overline{\mathcal{F}}^{(1)}_{\mathrm{eo}}$	$\mathcal{F}^{(1)}_{\mathrm{eo,min}}$	$\mathcal{F}_{\mathrm{eo}}(p_- = 0.5)$	$\epsilon_x(p_- = 0.5)$	$\overline{\eta}^{(1)}_{\mathrm{top}}$
2	0.0050	0.968236	0.943227	0.971376	0.010779	0.980773
	0.0075	0.963644	0.939076	0.966740	0.010781	0.980719
	0.0100	0.959110	0.934982	0.962170	0.010782	0.980664
	0.0200	0.941431	0.918990	0.944333	0.010793	0.980440
	0.0300	0.924509	0.903677	0.927244	0.010808	0.980208
3	0.0050	0.967458	0.950204	0.972294	0.006572	0.989480
	0.0075	0.960536	0.943705	0.965254	0.006574	0.989451
	0.0100	0.953721	0.937315	0.958324	0.006571	0.989422
	0.0200	0.927494	0.912724	0.931650	0.006572	0.989302
	0.0300	0.902855	0.889664	0.906578	0.006570	0.989174
4	0.0050	0.968686	0.960100	0.971782	0.004104	0.994848
	0.0075	0.959423	0.951120	0.962422	0.004106	0.994829
	0.0100	0.950346	0.942318	0.953248	0.004103	0.994810
	0.0200	0.915846	0.908891	0.918370	0.004101	0.994730
	0.0300	0.884044	0.878122	0.886201	0.004097	0.994644

Table A.9: Effect of one-photon loss in the two-photon-loss model at fixed $\kappa_2/K_{\mathrm{th}} = 3$ for $N_{\mathrm{out}} = 2, 3, 4$. All metrics are computed on the same truncated low-ε_x branch used in the corresponding figure. The quantity $\mathcal{F}_{\mathrm{eo}}(p_- = 0.5)$ is evaluated at the first occurrence of $p_- = 0.5$ as ε_x increases.

DEPARTMENT OF MICROTECHNOLOGY AND NANOSCIENCE
CHALMERS UNIVERSITY OF TECHNOLOGY
Gothenburg, Sweden
www.chalmers.se

CHALMERS
UNIVERSITY OF TECHNOLOGY